Dynamical Stability of Nascent Neutron Stars

Thesis by

Yuk Tung Liu

In Partial Fulfillment of the Requirements

for the Degree of

Doctor of Philosophy

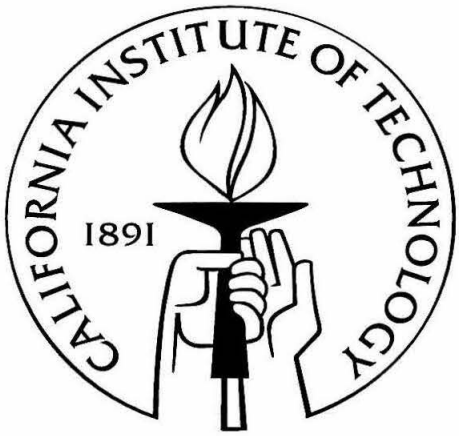

California Institute of Technology

Pasadena, California

2003

(Defended May 8, 2002)

Acknowledgements

I thank Lee Lindblom for his guidance on all aspects of this work, and giving me countless pieces of advice on this thesis and other manuscripts. Part of the work in this thesis was done in collaboration with Lee, from which I have learnt a lot of useful techniques. I thank Kip Thorne for stimulating discussions. I am also indebted to Kip for giving me an opportunity to work with him on the thermoelastic noise of LIGO test masses during the winter break of 1999.

I thank Chris Fryer for useful discussions on the accretion induced collapse and the structure of the resulting collapsed stars. Thanks are also given to Stuart Shapiro for useful discussions concerning issues on neutron stars and stability analysis. I thank Joel Tohline, from whom I learned several useful techniques in numerical simulations. I am indebted to Yanbei Chen and Alessandra Buonanno for teaching me various issues on the LIGO-II noise curve. I thank Yuri Levin and Eugene Chiang for useful discussions on various issues about white dwarfs and neutron stars.

I thank Lior Burko and Kashif Alvi for letting me collaborate with them on some of their research problems. I am grateful to all the people who have regularly participated in Kip's weekly group meetings. I have learned a lot of things from many stimulating discussions in the group meetings.

Last but not least, I thank my mother, father, and sister for their encouragement even though they do not know precisely what I do.

The work presented in this thesis was supported by NSF grants PHY-9796079, PHY-9900776 and AST-9731698, and NASA grant NAG5-4093.

Abstract

This thesis presents a study of the dynamical stability of nascent neutron stars resulting from the accretion induced collapse of rapidly rotating white dwarfs.

Chapter 2 and part of Chapter 3 study the equilibrium models for these neutron stars. They are constructed by assuming that the neutron stars have the same masses, angular momenta, and specific angular momentum distributions as the pre-collapse white dwarfs. If the pre-collapse white dwarf is rapidly rotating, the collapsed object will contain a high density central core of size about 20 km, surrounded by a massive accretion torus extending to hundreds of kilometers from the rotation axis. The ratio of the rotational kinetic energy to gravitational binding energy, β, of these neutron stars is all found to be less than 0.27.

Chapter 3 studies the dynamical stability of these neutron stars by numerically evolving the linearized hydrodynamical equations. A dynamical bar-mode instability is observed when the β of the star is greater than the critical value $\beta_d \approx 0.25$. It is expected that the unstable mode will persist until a substantial amount of angular momentum is carried away by gravitational radiation. The detectability of these sources is studied and it is estimated that LIGO II is unlikely to detect them unless the event rate is greater than 10^{-6}/year/galaxy.

All the calculations on the structure and stability of the neutron stars in Chapters 2 and 3 are carried out using Newtonian hydrodynamics and gravity. Chapter 4 studies the relativistic effects on the structure of these neutron stars. New techniques are developed and used to construct neutron star models to the first post-Newtonian (1PN) order. The structures of the 1PN models are qualitatively similar to the corresponding Newtonian models, but the values of β are somewhat smaller. The maximum β for these 1PN neutron stars is found to be 0.24, which is 8% smaller than the Newtonian result (0.26). However, relativistic effects will also change the critical value β_d. A detailed post-Newtonian stability analysis has yet to be carried out to study the relativistic effects on the dynamical stability of these neutron stars.

Contents

List of Figures

List of Tables

Chapter 1

Introduction and Summary

1.1 Accretion induced collapse

White dwarfs, stars that are mainly supported by degenerate electron pressure, are one of the end products of stellar evolution. Most white dwarfs are made of carbon and oxygen (C-O white dwarfs), while a small fraction of them are made of oxygen, neon and magnesium (O-Ne-Mg white dwarfs). The C-O white dwarfs are formed when main sequence stars of masses $M \lesssim 6M_{\odot}$ exhaust their nuclear fuel, whereas O-Ne-Mg white dwarfs are formed from stars with initial masses of $8M_{\odot} - 12M_{\odot}$ in close binaries (see [1] for a review).

An isolated white dwarf simply cools and radiates away its residual thermal energy and quietly turns into a dark star. A white dwarf in a binary system may evolve differently, because it could accrete matter from its companion. The mass, central density and angular momentum of the white dwarf could increase as a result of this accretion. If the mass of the accreting white dwarf is close to the Chandrasekhar limit, the accretion may eventually make it massive enough that it can no longer maintain hydrodynamic equilibrium. The star will either explode as a Type Ia supernova or collapse to a neutron star (see Sections 1.3 and 2.2 for detail).

An accreting white dwarf can easily be spun up to rapid rotation by the accretion material [18]. Hence the massive white dwarf usually rotates rapidly before it becomes unstable. If collapse results, conservation of angular momentum implies that the new-born neutron star formed from this *accretion induced collapse* (AIC) must rotate rapidly, and a significant portion of the stellar material would be hung up by the centrifugal force. The collapsed object would contain a relatively high density neutron core surrounded by a highly flattened, centrifugally supported disk. This rapidly rotating star may develop a non-axisymmetric instability which typically has the shape of a bar. It has been suggested [2] that this unstable "bar" mode could emit a substantial amount of gravitational

radiation that might be detectable by gravitational wave interferometers, such as LIGO, VIRGO, GEO and TAMA.

The objectives of this thesis are

- to build equilibrium models of the new-born neutron stars produced by AIC and study their properties;
- to determine under what circumstance these neutron stars could develop a dynamical instability;
- to estimate the strength and signal-to-noise ratio of the gravitational radiation emitted by neutron stars undergoing this instability;
- to study the effects of general relativity on the equilibrium structure of these neutron stars.

The structure of this thesis is as follows. In this chapter, we give a general introduction to the main issues and summarize all the important results. In Chapter 2, we describe in detail the techniques we use to construct the equilibrium models. Next we build three of the most rapidly rotating models using both hot and cold equations of state and study the stars' properties. In Chapter 3, we study the stability of these neutron stars and determine under what condition a neutron star could be dynamically unstable. To do this, we first construct a number of equilibrium neutron star models with different amounts of rotation using the method described in Chapter 2. Next we analyze the stability of each of the models. Finally, we estimate the strength and signal-to-noise ratio of the gravitational radiation emitted by neutron stars undergoing the instability. All the computations in Chapters 2 and 3 were done using Newtonian hydrodynamics and gravity. Neutron stars are compact, and relativistic effects play a significant role in the equilibrium structure as well as their stability. So in Chapter 4, we develop new techniques and construct the equilibrium models of the nascent neutron stars that include first post-Newtonian effects. We then compare the relativistic models with the Newtonian ones.

Most of the work presented in this thesis was done independently by the author under the supervision of Lee Lindblom. Part of the work on the construction of equilibrium models in Chapter 2 was done in collaboration with Lee Lindblom.

1.2 Dynamical instabilities of a rapidly rotating star

As mentioned in the previous Section, the new-born neutron star resulting from the AIC of a rapidly rotating white dwarf, or from the collapse of a rapidly rotating massive stellar core, could develop a non-axisymmetric instability. We shall describe this type of instability in this Section.

Rotational instabilities arise from non-axisymmetric perturbations having angular dependence $e^{im\varphi}$, where φ is the azimuthal angle. The $m = 2$ mode is called the bar mode, and is usually the strongest mode for stars undergoing this type of instability. There are two types of instabilities. A *dynamical* instability is driven by hydrodynamics and gravity, and it develops on a dynamical timescale, e.g., the timescale for a sound wave to travel across the star. A *secular* instability, on the other hand, is driven by viscosity or gravitational radiation reaction, and its growth time is determined by the relevant dissipative timescale. These secular timescales are usually much longer than the dynamical timescale of the system. This thesis only studies the dynamical instabilities, because they are much stronger and so are unlikely to be strongly affected dynamically by viscosity, magnetic fields or other dissipative processes.

These non-axisymmetric dynamical instabilities occur only for rapidly rotating stars. A useful parameter to characterize the rotation of a star is $\beta = T/|W|$, where T and W are the rotational kinetic energy and gravitational potential energy, respectively. It is well known that there is a critical value β_d such that a star will be dynamically unstable if $\beta > \beta_d$. For a uniform density and rigidly rotating star, a Maclaurin spheroid, the critical value is determined to be $\beta_d \approx 0.27$ [3]. Many numerical simulations using Newtonian gravity show that β_d remains roughly the same for differentially rotating polytropes having the same specific angular momentum distribution as the Maclaurin spheroids [4, 5, 6, 7, 8, 9, 10, 11, 12]. However, β_d can take values between 0.14 and 0.27 for other angular momentum distributions [13, 10, 14] (the lower limit $\beta_d = 0.14$ is observed only for a star having a toroidal density distribution, i.e., the maximum density occurs off the center [14]). Numerical simulations using full general relativity and post-Newtonian approximations suggest that relativistic corrections to Newtonian gravity cause β_d to decrease slightly [15, 16, 17].

Most of the stability analyses to date have been carried out by assuming that the star rotates with an *ad hoc* rotation law or using simplified equations of state. The results of these analyses might not be applicable to the new-born neutron stars resulting from AIC. Recently, Fryer, Holz and Hughes [18] carried out an AIC simulation using a realistic rotation law and a realistic equation of state. Their pre-collapse white dwarf has an angular momentum $J = 10^{49}$ g cm^2 s^{-1}. After the collapse, the neutron star has β less than 0.06, which is too small for the star to be dynamically

unstable. However, they point out that if the pre-collapse white dwarf spins faster, the resulting neutron star could have high enough β to trigger a dynamical instability. They also point out that a pre-collapse white dwarf could easily be spun up to rapid rotation by accretion. The spin of an accreting white dwarf before collapse depends on its initial mass, its magnetic field strength, its accretion rate, etc. [19].

One of the purposes of this thesis is to carry out more realistic analyses of the stability of the nascent neutron stars resulting from AIC. The strategy is as follows. First, build equilibrium neutron star models. Second, perturb these stars by adding small density and velocity perturbations to the equilibrium models. Third, numerically evolve the linearized hydrodynamical equations and see if the perturbations grow with time. Fourth, extract the growth rate from the evolution data. Finally, determine the critical value β_d for the onset of the dynamical instability.

1.3 Equilibrium models

The proper way to construct the equilibrium neutron star model is to numerically follow the collapse of the white dwarf and wait for the final collapsed object to settle down into hydrodynamic equilibrium. Such a realistic simulation has been done by Fryer et al. [18] for a slowly rotating pre-collapse white dwarf. Simulations for the collapse of massive stellar cores were also performed by several authors [20, 21, 22, 23, 24]. This kind of simulation is computational expensive, so we adopt a simpler approach: build the equilibrium neutron star model which has the same total mass, angular momentum and specific angular momentum distribution $j(m_\varpi)$ as the pre-collapse white dwarf. Here m_ϖ is the mass fraction interior to a cylindrical surface.

This method is justified if the following assumptions are correct:

1. the collapse is axisymmetric;
2. viscosity can be neglected;
3. there is no meridional circulation in the final state of the neutron star;
4. the neutron star are described by a barotropic equation of state, i.e., the pressure P is a function of density ρ only;
5. no material is ejected during the collapse.

Assumption 3 is probably the most controversial one. However, such a rotational profile was observed in some collapse simulations [21, 22, 25].

In order to build the neutron star models by the above method, we first have to build the models of pre-collapse white dwarfs, calculate in each model the star's total mass M, angular momentum J and specific angular momentum j as a function of the cylindrical mass fraction m_{ϖ}. These are the parameters necessary to build a mapping between a pre-collapse white dwarf and the resulting neutron star.

1.3.1 Models of pre-collapse white dwarfs

When a C-O white dwarf is accreting material, the star compresses and releases gravitational energy. Part of the gravitational energy is used to raise the Fermi energy of the degenerate electrons, and the rest turns into heat (compressional heating) [26]. The evolution of the temperature of the white dwarf depends on the balance between the cooling and compressional heating. When the central density and/or temperature is high enough, carbon will ignite explosively. While the carbon combustion front propagates outward, electron captures behind the front soften the equation of state (EOS) and make the star unstable. There are two possible outcomes. The white dwarf will either be torn apart by the runaway carbon burning or collapse to a neutron star. Which path the white dwarf takes depends on the competition between the carbon burning and electron captures [27]. Electron captures happen only at high density where the Fermi energy of the electrons is high enough to trigger inverse beta decay. Numerical simulations [29, 30] suggest that if carbon ignition occurs at a central density ρ_c in the range 6×10^9 g cm$^{-3} \lesssim \rho_c \lesssim 10^{10}$ g cm^{-3}, electron captures take over and the star will collapse to a neutron star. The density at which carbon ignites depends on the entire accretion history of the white dwarf. The fate of an accreting C-O white dwarf as a function of its initial mass and accretion rate is summarized in a diagram in Ref. [27] (see also [28]).

An O-Ne-Mg white dwarf becomes unstable when the central density reaches 4×10^9 g cm^{-3}. At this density, electron captures by ^{24}Mg occur and soften the EOS and induce collapse. The star will most likely collapse to a neutron star in this case. A more detailed discussion on the onset of the instability of a massive white dwarf is given in Section 2.2.1.

In Chapter 2, we compute three rapidly rotating pre-collapse white dwarf models using the numerical method developed by Hachisu [31] (see Section 2.2.2 for a brief review). Two of the models are for C-O white dwarfs with central densities $\rho_c = 6 \times 10^9$ g cm^{-3} and 10^{10} g cm^{-3}. The other one is for an O-Ne-Mg white dwarf with $\rho_c = 4 \times 10^9$ g cm^{-3}. These white dwarfs are rotating at the fastest possible frequency before mass shedding occurs at the equatorial surfaces. The masses, angular momenta and $j(m_{\varpi})$ distributions are computed in Section 2.2.3. These parameters are then

used to build the neutron star models corresponding to the collapse of these white dwarfs.

In order to determine the onset of dynamical instability, it is necessary to build more equilibrium models. So in Chapter 3, we compute sequences of rigidly rotating white dwarf models with different amounts of rotation. All the white dwarf models computed in this thesis are rigidly rotating, because the timescale for a magnetic field to suppress differential rotation is much shorter than the accretion timescale.

1.3.2 Models of nascent neutron stars

The gravitational collapse of a massive white dwarf is halted when the central density reaches nuclear density where the EOS becomes stiff. The core bounces back and within a few milliseconds, a hot ($T \gtrsim 20$ Mev), lepton rich protoneutron star settles into hydrodynamic equilibrium. During the so-called Kelvin-Helmholtz cooling phase, the temperature and lepton number decrease due to neutrino emission and the protoneutron star cools to a cold neutron star with temperature $T < 1$ Mev after several minutes. Since the cooling timescale is much longer than the hydrodynamical timescale, the protoneutron star can be regarded as in quasi-equilibrium.

In Chapter 2, we construct neutron star models using two sets of EOS's. One EOS is for the hot protoneutron stars and the other is one of the standard cold EOS's.

Equilibrium models are computed in Section 2.3.3 for the neutron stars corresponding to the collapse of the three white dwarfs in Section 2.2.3. They all consist of a high density central core of size about 20 km, surrounded by a massive accretion torus extending over 1000 km from the rotation axis. The stars are centrally condensed. More than 90% of the stellar mass is contained in the core and core-torus transition region, which is within about 100 km from the rotation axis. The structure of the hot protoneutron star models is very different from the cold models. The cold models are more compact, rotate faster and have a higher value of $\beta = T/|W|$, where T is the rotational kinetic energy and $|W|$ is the gravitational binding energy. The central densities of the hot protoneutron stars range from 3×10^{13} g cm^{-3} to 10^{14} g cm^{-3}. The central densities of the three cold models are about the same: $\rho_c \approx 3.5 \times 10^{14}$ g cm^{-3}. The values of β of the three cold models range from 0.23 to 0.26, whereas those of the hot models are $\beta = 0.13 - 0.14$. Up to this point, it is still not certain whether or not the cold models are dynamically unstable, but it is very likely that the hot models are stable. So we expect that when a white dwarf undergoes AIC, the collapsed star will first settle down in the quasi-equilibrium, hot protoneutron star phase. After about 20 s, the star cools down, increases its rotation rate and may be able to develop a dynamical instability.

More equilibrium neutron star models are computed in Chapter 3, Section 3.2.2. The objective of that chapter is to determine the onset of dynamical stability, so only cold models are computed there. The structure of the rapidly rotating neutron stars is qualitatively the same as that of the cold models described in the previous paragraph. All neutron stars resulting from AIC have $\beta \leq 0.26$, which is slightly less than the critical value β_d for the onset of a dynamical instability in the Maclaurin spheroids. Hence, a detailed stability analysis has to be carried out on these neutron stars.

1.4 Stability analysis

The motion of fluid inside a star, in the Newtonian approximation, is described by the hydrodynamical equations:

$$\frac{\partial \rho}{\partial t} + \boldsymbol{\nabla} \cdot (\rho \boldsymbol{v}) = 0 \, , \tag{1.1}$$

$$\frac{\partial \boldsymbol{v}}{\partial t} + \boldsymbol{v} \cdot \boldsymbol{\nabla} \boldsymbol{v} = -\frac{\boldsymbol{\nabla} \boldsymbol{P}}{\rho} - \boldsymbol{\nabla} \Phi \, , \tag{1.2}$$

$$\nabla^2 \Phi = 4\pi G \rho \, , \tag{1.3}$$

where ρ is density; $\boldsymbol{v}$ is the fluid's velocity; P is the pressure and Φ is the gravitational potential. To study the stability of the fluid's motion, we perturb the density ρ and velocity $\boldsymbol{v}$ away from their equilibrium values, ρ_0 and $\boldsymbol{v}_0$, by small quantities:

$$\rho(\boldsymbol{x}, t) = \rho_0(\boldsymbol{x}) + \delta\rho(\boldsymbol{x}, t) \, , \tag{1.4}$$

$$\boldsymbol{v}(\boldsymbol{x}, t) = \boldsymbol{v}_0(\boldsymbol{x}) + \delta\boldsymbol{v}(\boldsymbol{x}, t) \, . \tag{1.5}$$

The stability can be determined by numerically evolving $\delta\rho$ and $\delta\boldsymbol{v}$ and seeing if they grow with time. To find the onset of the instability, it is necessary to evolve only the linearized equations. This idea and numerical techniques were first proposed by Toman et al. [32].

Consider the angular Fourier decomposition of any perturbed quantity δq:

$$\delta q(\boldsymbol{x}, t) = \sum_{m=-\infty}^{\infty} \delta \tilde{q}_m(\varpi, z, t) e^{im\varphi} \, , \tag{1.6}$$

where ϖ is the cylindrical radius from the rotation axis and φ is the azimuthal angle. It is easy to prove that the m-modes decouple in the linearized hydrodynamical equations because of the

axisymmetry of the equilibrium configuration. Hence each m-mode can be evolved independently and the 3+1 simulation is reduced to many 2+1 simulations.

In Chapter 3, we evolve the perturbations $\delta\rho$ and $\delta\boldsymbol{v}$ by solving the linearized hydrodynamical equations and find that a bar-mode ($m = 2$) instability develops for stars with $\beta \geq \beta_d \approx 0.25$. No other unstable m-modes are observed. We find that all the neutron stars corresponding to the AIC of C-O white dwarfs are dynamically stable. Their β's are all less than the critical value β_d. Only the cold neutron stars resulting from the collapse of the O-Ne-Mg white dwarfs which rotate more than 93% of the maximum frequency can have $\beta > \beta_d$. The frequency of the unstable mode is $f \approx 450$ Hz and its growth rate is about 8 ms for the most rapidly rotation model ($\beta = 0.26$). As a comparison, the rotational frequency at the center of the star is 700 Hz.

1.5 Gravitational radiation

According to general relativity, time varying mass and current multipole moments (higher than the dipole) generate gravitational waves. Since a rapidly rotating neutron star could be unstable to the bar mode, the amplitude of the mode could become very large, providing a large amplitude of time changing multipole moments and emitting a substantial amount of gravitational waves. Recent full hydrodynamical simulations on the bar-mode instability [12, 33] show that the mode saturates when the density perturbation is comparable to the equilibrium density. In these simulations, the mode pattern persists after the saturation. It is possible that the mode will not be suppressed until gravitational waves remove a substantial amount of angular momentum from the star. The complete waveforms and strength of the gravitational waves emitted by this bar-mode instability depend on the unknown detailed nonlinear evolution of the mode. However, we can estimate the strength and detectability of the signals from the results of the linearized hydrodynamical evolutions. The detailed analysis is presented in Section 3.4. Here we summarize the results.

Simple analysis shows that the gravitational radiation emitted by these sources is dominated by the time changing mass quadrupole moments. The gravitational wave strength h is estimated to be

$$h \approx \alpha\, 7 \times 10^{-23} \left(\frac{20 \text{ Mpc}}{D} \right) , \tag{1.7}$$

where α is a dimensionless amplitude of the bar mode and D is the distance between the source and detector. The optimal signal-to-noise ratio for detecting this type of signal by the LIGO-II

broad-band interferometers is estimated to be

$$\frac{S}{N} = 15 \left(\frac{20 \text{ Mpc}}{D}\right) \left(\frac{\Delta J}{5 \times 10^{48} \text{ g cm}^2 \text{ s}^{-1}}\right)^{1/2} \left(\frac{f}{450 \text{ Hz}}\right)^{-1/2} \times \left(\frac{\sqrt{S_h(f)}}{2 \times 10^{-24} \text{ Hz}^{-1/2}}\right)^{-1}, \quad (1.8)$$

where f is the oscillation frequency of the mode; ΔJ is the total amount of angular momentum emitted by the gravitational waves and $S_h(f)$ is the spectral density of the gravitational wave detectors. The value 5×10^{48} g cm^2 s^{-1} is the estimated maximum amount of ΔJ.

The detectability of this type of source also depends on the event rate. The event rate for AIC is estimated to be between 10^{-5} and 10^{-8} per galaxy per year [34, 35]. Of all the AIC events, only those corresponding to the collapse of rapidly rotating O-Ne-Mg white dwarfs can end up in the bar-mode instability, and the fraction of these is unknown. If a signal-to-noise ratio of 5 is required to detect the source, an event rate of at least 10^{-6}/galaxy/year is required for such a source to occur at a detectable distance per year. Hence these sources will not be promising for LIGO II if the event rate is much less than 10^{-6} per year per galaxy.

The event rate of the core collapse of massive stars is much higher than that of AIC. The structure of a pre-supernova core is very similar to that of a pre-collapse white dwarf, so our results might be applicable to the neutron stars produced by the core collapse. If the core is rapidly rotating, the resulting neutron star might be able to develop a bar-mode instability. If a significant fraction of the pre-supernova cores are rapidly rotating, the chance of detecting the gravitational radiation from the bar-mode instability might be much higher than expected.

1.6 Relativistic effects

All the neutron star calculations discussed in Sections 1.3-1.4 have been done with Newtonian hydrodynamics and gravity. However, neutron stars are compact objects and general relativistic effects have a significant influence on both the structure and dynamical stability of the stars. Recent numerical simulations by Shibata, Baumgarte, Shapiro and Saijo show that as the star becomes more compact, the critical value β_d for the onset of the dynamical instability slightly decreases from the Newtonian value 0.26 to 0.24 for a specific EOS and rotation law [16, 17]. It is not clear, however, whether their result suggests that the relativistic effects would destabilize the stars we are studying, for the equilibrium structure of the star will also be changed by the relativistic effects. The value of β of a relativistic star will not be the same as that of a Newtonian star with the same baryon mass and total angular momentum. In Chapter 4, we compute the equilibrium models of neutron

stars to the first post-Newtonian (1PN) order and compare them with the corresponding Newtonian models (in Section 3.2.2). We only compute the neutron star models corresponding to the collapse of O-Ne-Mg white dwarfs since they are the only models that can be dynamically unstable in the Newtonian case.

We make the same assumptions in the construction of equilibrium models as we do in the Newtonian calculations. We compute models with the same baryon mass M_0, total angular momentum J and specific angular momentum distribution $j(m_\varpi)$ as the pre-collapse white dwarfs. However, none of the existing methods in the literature for constructing post-Newtonian models, as far as we know, are designed to build models with a specified $j(m_\varpi)$. We formulate a new version of the equilibrium equations that are accurate to 1PN order and generalize Smith and Centrella's version of the self-consistent field method [36], so that it can be used to build models with a specified $j(m_\varpi)$. The details are presented in Sections 4.2 and 4.3.

The 1PN models are presented in Section 4.4. We find that the structures of these 1PN models are qualitatively the same as the Newtonian models having the same baryon masses and angular momenta. However, they are more compact, rotate faster, and have smaller values of β than their Newtonian counterparts. The highest value of β the neutron star can achieve is 0.24, which is 8% smaller than the Newtonian case. We estimate that the fractional error due to our neglecting higher order post-Newtonian terms is about 3%.

We demonstrate in Chapter 4 that the relativistic effects lower the value of β of a star. Shibata, Baumgarte, Shapiro and Saijo demonstrated that the relativistic effects also lower the critical value β_d for the dynamical instability by a similar amount. Hence, it is not clear at this point whether relativistic effects destabilize the star. Numerical stability analyses have to be carried out to settle this issue, but these are beyond the scope of this thesis.

Bibliography

[1] K. Nomoto and M. Hashimoto, Phys. Rep. **163**, 13 (1988).

[2] K. S. Thorne, in *Black Holes and Relativistic Stars*, ed. R. M. Wald (The University of Chicago Press, 1998).

[3] S. Chandrasekhar, *Ellipsoidal Figures of Equilibrium* (New Haven: Yale University Press, 1969).

[4] J. E. Tohline, R. H. Durisen and M. McCollough, Astrophys. J., **298**, 220, 1985.

[5] R. H. Durisen, R. A. Gingold, J. E. Tohline and A. P. Boss, Astrophys. J., **305**, 281, 1986.

[6] H. A. Williams and J. E. Tohline, Astrophys. J., **334**, 449, 1988.

[7] J. L. Houser, J. M. Centrella and S. C. Smith, Phys. Rev. Lett., **72**, 1314, 1994.

[8] S. Smith, J. L. Houser and J. M. Centrella, Astrophys. J., **458**, 236 (1996).

[9] J. L. Houser and J. M. Centrella, Phys. Rev. D., **54**, 7278 (1996).

[10] B. K. Pickett, R. H. Durisen and R. H. Davis, Astrophys. J., **458**, 714 (1996).

[11] J. L. Houser, Mon. Not. Roy. Astro. Soc., **209**, 1069 (1998).

[12] K. C. B. New, J. M. Centrella and J. E. Tohline, Phys. Rev. D, **62**, 064019 (2000).

[13] J. N. Imamura and J. Toman, Astrophys. J, **444**, 363 (1995).

[14] J. M. Centrella, K. C. B. New, L. L. Lowe and J. D. Brown, Astrophys. J. Lett., **550**, 193 (2001).

[15] N. Stergioulas and J. L. Friedman, Astrophys. J., **492**, 301 (1998).

[16] M. Shibata, T. W. Baumgarte and S. L. Shapiro, Astrophys. J., **542**, 453 (2000).

[17] M. Saijo, M. Shibata, T. W. Baumgarte and S. L. Shapiro, Astrophys. J., **548**, 919 (2000).

[18] C. L. Fryer, D. E. Holz and S. A. Hughes, to appear in Astrophys. J., astro-ph/0106113 (2001).

[19] See e.g., R. Narayan and R. Popham, Astrophys. J. Lett., **346**, 25 (1989).

[20] E. Müller, W. Hillebrandt, Astro. & Astrophys., **103**, 358 (1981).

[21] R. Mönchmeyer and E. Müller, in NATO ASI on *Timing Neutron Stars*, ed. Ögelman H., D. (Reidel Publ. Comp., Dordrecht, 1988).

[22] H.-Th. Janka and R. Mönchmeyer, Astro. & Astrophys., **209**, L5 (1989); H.-Th. Janka and R. Mönchmeyer, Astro. & Astrophys., **226**, 69 (1989).

[23] R. Mönchmeyer, G. Schäfer, E. Müller and Katea R. E., Astro. & Astrophys., **246**, 417 (1991).

[24] T. Zwerger and E. Müller, Astro. & Astrophys., **320**, 209 (1997).

[25] C. L. Fryer, private communication.

[26] K. Nomoto, Astrophys. J., **253**, 798 (1982).

[27] K. Nomoto in *Proc. 13th Texas Symposium on Relativistic Astrophysics*, ed. M. Ulmer (Singapore: World Scientific, 1987).

[28] K. Nomoto and Y. Kondo, Astrophys. J. Lett., **367**, 19 (1991).

[29] F. S. Timmes and S. E. Woosley, Astrophys. J., **396**, 649 (1992).

[30] E. Bravo and D. García-Senz, Mon. Not. R. Astro. Soc., **307**, 984 (1999).

[31] I. Hachisu, Astrophys. J. Supp., **61**, 479 (1986).

[32] J. T. Toman, J. N. Imamura, B. K. Pickett and R. H. Durisen, Astrophys. J., **497**, 370 (1998).

[33] J. D. Brown, Phys. Rev. D., **62**, 0004002 (2000).

[34] V. Kalogera, to appear in the proceedings of the 3rd Amaldi Conference on Gravitational Waves, astro-ph/9911532 (1999).

[35] C. L. Fryer, W. Benz, S. A. Colgate and M. Herant, Astrophys. J., **516**, 892 (1999).

[36] S. Smith, J. M. Centrella, in *Approaches to Numerical Relativity*, ed. R. d'Inverno. (Cambridge Univ. Press, New York 1992).

Chapter 2

Models of Rapidly Rotating Neutron Stars: Remnants of Accretion Induced Collapse

Coauthored with Lee Lindblom; published in *Monthly Notices of the Royal Astronomical Society* [Mon. Not. Roy. Astro. Soc. **324**, 1063 (2001)].

Abstract

Equilibrium models of differentially rotating nascent neutron stars are constructed, which represent the result of the accretion induced collapse of rapidly rotating white dwarfs. The models are built in a two-step procedure: (1) a rapidly rotating pre-collapse white dwarf model is constructed; (2) a stationary axisymmetric neutron star having the same total mass and angular momentum distribution as the white dwarf is constructed. The resulting collapsed objects consist of a high density central core of size roughly 20 km, surrounded by a massive accretion torus extending over 1000 km from the rotation axis. The ratio of the rotational kinetic energy to the gravitational potential energy of these neutron stars ranges from 0.13 to 0.26, suggesting that some of these objects may have a non-axisymmetric dynamical instability that could emit a significant amount of gravitational radiation.

2.1 Introduction

The accretion induced collapse of a rapidly rotating white dwarf can result in the formation of a rapidly and differentially rotating compact object. It has been suggested that such rapidly rotating objects could emit a substantial amount of gravitational radiation [53], which might be observable

by the gravitational wave observatories, such as LIGO, VIRGO and GEO. It has been demonstrated that if the collapse is axisymmetric, the energy emitted by gravitational waves is rather small [34, 12, 32, 58]. However, if the collapsed object rotates rapidly enough to develop a non-axisymmetric "bar" instability, the total energy released by gravitational waves could be 10^4 times greater than the axisymmetric case [20, 19, 49, 18].

Rotational instabilities of rotating stars arise from non-axisymmetric perturbations of the form $e^{im\varphi}$, where φ is the azimuthal angle. The $m = 2$ mode is known as the *bar mode*, which is often the fastest growing unstable mode. There are two kinds of instabilities. A *dynamical* instability is driven by hydrodynamics and gravity, and develops on a dynamical timescale, e.g., the time for sound waves to travel across the star. A *secular* instability is driven by dissipative processes, such as viscosity or gravitational radiation reaction, and the growth time is determined by the dissipative timescale. These secular timescales are usually much longer than the dynamical timescale of the system. An interesting class of secular and dynamical instabilities only occur in rapidly rotating stars. One convenient measure of the rotation of a star is the parameter $\beta = T_{\rm rot}/|W|$, where $T_{\rm rot}$ is the rotational kinetic energy and W is the gravitational potential energy. Dynamical and secular instabilities set in when β exceeds the critical values β_d and β_s respectively. It is well known that $\beta_d \approx 0.27$ and $\beta_s \approx 0.14$ for uniformly rotating, constant density and incompressible stars, the Maclaurin spheroids [8]. Numerous numerical simulations in Newtonian theory show that β_d and β_s have roughly these same values for differentially rotating polytropes with the same specific angular momentum distribution as the Maclaurin spheroids [56, 10, 57, 20, 49, 19, 40, 18, 35]. However, the critical values of β are smaller for polytropes with some other angular momentum distributions [21, 40, 7]. And general relativistic simulations also suggest that the critical values of β are smaller than the classical Maclaurin spheroid values [50, 47, 42].

Most of the stability analyses to date have been carried out on stars having simple *ad hoc* rotation laws. It is not clear whether these rotation laws are appropriate for the nascent neutron stars formed from the accretion induced collapse of rotating white dwarfs.

New-born neutron stars resulting from the core collapse of massive stars with realistic rotation laws were studied by Mönchmeyer, Janka and Müller [31, 24, 25], and Zwerger and Müller [58]. The study of Mönchmeyer et al. shows that the resulting neutron stars have $\beta < 0.14$. Zwerger and Müller carried out simulations of 78 models using simplified analytical equations of state (EOS). They found only one model having $\beta > 0.27$ near core bounce. However, β remains larger than 0.27 for only about one millisecond, because the core re-expands after bounce and slows down. The pre-

collapse core of that model is the most extreme one in their large sample: it is the *most rapidly* and most differentially rotating model, and it has the softest EOS. In addition, they found three models with $0.14 < \beta < 0.27$. Rampp, Müller and Ruffert [41] subsequently performed 3-D simulations of three of these models. They found that the model with $\beta > 0.27$ shows a nonlinear growth of a non-axisymmetric dynamical instability dominated by the bar mode ($m = 2$). However, no instability is observed for the other two models during their simulated time interval of tens of milliseconds, suggesting that they are dynamically stable. Their analysis does not rule out the possibility that these models have non-axisymmetric secular instabilities, because the secular timescale is expected to range from hundreds of milliseconds to few minutes, much longer than their simulation time.

The aim of this chapter is to improve Zwerger and Müller's study by using realistic EOS for both the pre-collapse white dwarfs and the collapsed stars. For the pre-collapse white dwarfs, we use the EOS of a zero-temperature degenerate electron gas with electrostatic corrections. A hot, lepton rich protoneutron star is formed as a result of the collapse. This protoneutron star cools down to a cold neutron star in about 20 s (see, e.g., [6]), which is much longer than the dynamical timescale. So we adopt two EOS for the collapsed stars: one is suitable for protoneutron stars; the other is one of the standard cold neutron-star EOS.

Instead of performing the complicated hydrodynamic simulations, however, we adopt a much simpler method. We assume (1) the collapsed stars are in rotational equilibrium with no meridional circulation, (2) any ejected material during the collapse carries a negligible amount of mass and angular momentum, and (3) the neutron stars have the same specific angular momentum distributions as those of the pre-collapse white dwarfs. The justifications of these assumptions will be discussed in Section 2.3. Our strategy is as follows. First we build the equilibrium pre-collapse rotating white dwarf models and calculate their specific angular momentum distributions. Then we construct the resulting collapsed stars having the same masses, total angular momenta and specific angular momentum distributions as those of the pre-collapse white dwarfs. All computations in this chapter are purely Newtonian. In the real situation, if a dynamical instability occurs, the star will never achieve equilibrium. However, our study here can still give a useful clue to the instability issue.

This Chapter is organized as follows. In the next section we present equilibrium models of pre-collapse, rapidly and rigidly rotating white dwarfs. In Section 2.3, we construct the equilibrium models corresponding to the collapse of these white dwarfs. The stabilities of the collapsed objects are discussed in Section 2.4. Finally, we summarize our conclusions in Section 2.5.

2.2 Pre-collapse white dwarf models

2.2.1 Collapse mechanism

As mass is accreted onto a white dwarf, the matter in the white dwarf's interior is compressed to higher densities. Compression releases gravitational energy and some of the energy goes into heat [36]. If the accretion rate is high enough, the rate of heat generated by this *compressional heating* is greater than the cooling rate and the central temperature of the accreting white dwarf increases with time.

The inner core of a carbon-oxygen (C-O) white dwarf becomes unstable when the central density or temperature becomes sufficiently high to ignite explosive carbon burning. Carbon deflagration releases nuclear energy and causes the pressure to increase. However, electron capture behind the carbon deflagration front reduces the temperature and pressure and triggers collapse. Such a white dwarf will either explode as a Type Ia supernova or collapse to a neutron star. Which path the white dwarf takes depends on the competition between the nuclear energy release and electron capture [37]. If the density at which carbon ignites is higher than a critical density of about 9×10^9 g cm^{-3} [54], electron capture takes over and the white dwarf will collapse to a neutron star. However, if the ignition density is lower than the critical density, carbon deflagration will lead to a total disruption of the whole star, leaving no remnant at all. More recent calculations by Bravo and García-Senz [4], taking into account the Coulomb corrections to the EOS, suggest that this critical density is somewhat lower: 6×10^9 g cm^{-3}. The density at which carbon ignites depends on the central temperature. The central temperature is determined by the balance between the compressional heating and the cooling and so strongly depends on the accretion rate and accretion time. For zero-temperature C-O white dwarfs, carbon ignites at a density of about 10^{10} g cm^{-3} [44, 39], which is higher than the above critical density. If the accreting white dwarf can somehow maintain a low central temperature during the whole accretion process, carbon will ignite at a density higher than the critical density, and the white dwarf will collapse to a neutron star. The fate of an accreting white dwarf as a function of the accretion rate and the white dwarf's initial mass is summarized in two diagrams in the paper of Nomoto [37] (see also [38]). Roughly speaking, low accretion rates ($\dot{M} \lesssim 10^{-8} M_\odot$ yr^{-1}) and high initial mass of the white dwarf ($M \gtrsim 1.1\, M_\odot$), or very high accretion rates (near the Eddington limit) lead to collapse rather than explosion.

Under certain conditions, an accreting oxygen-neon-magnesium (O-Ne-Mg) white dwarf can also collapse to a neutron star [37, 38]. The collapse is triggered by the electron captures of ^{24}Mg

and ^{20}Ne at a density of 4×10^9 g cm^{-3}. Electron captures not only soften the EOS and induce collapse, but also generate heat by γ-ray emission. When the star is collapsed to a central density of 10^{10} g cm^{-3}, oxygen ignites [38]. At such a high density, however, electron captures occur at a faster rate than the oxygen burning and the white dwarf collapses all the way to a neutron star.

In this section, we explore a range of possible pre-collapse white dwarf models. We assume that the white dwarfs are rigidly rotating. This is justified by the fact that the timescale for a magnetic field to suppress any differential rotation, τ_B, is short compared with the accretion timescale. For example, $\tau_B \sim 10^3$ years if the massive white dwarf has a magnetic field $B \sim 100G$. We construct three white dwarf models using the EOS of a zero-temperature degenerate electron gas with Coulomb corrections derived by Salpeter [43]. All three white dwarfs are rigidly rotating at the maximum possible angular velocities. *Model I* represents a C-O white dwarf with a central density of $\rho_c = 10^{10}$ g cm^{-3}, the highest ρ_c a C-O white dwarf can have before carbon ignition induces collapse. *Model II* is also a C-O white dwarf but has a lower central density, $\rho_c = 6 \times 10^9$ g cm^{-3}. This is the lowest central density for which a white dwarf can still collapse to a neutron star after carbon ignition. *Model III* is an O-Ne-Mg white dwarf with $\rho_c = 4 \times 10^9$ g cm^{-3}, that is the density at which electron captures occur and induce the collapse. Since the densities are very high, the pressure is dominated by the ideal degenerate Fermi gas with electron fraction $Z/A = 1/2$ that is suitable for both C-O and O-Ne-Mg white dwarfs. Coulomb corrections, which depend on the white dwarf composition through the atomic number Z, contribute only a few per cent to the EOS at high densities, so the three white dwarfs are basically described by the same EOS.

2.2.2 Numerical method

We treat the equilibrium rotating white dwarfs as rigidly rotating, axisymmetric, and having no internal motion other than the motion due to rotation. The Lichtenstein theorem (see, e.g., [52]) guarantees that a rigidly rotating star has reflection symmetry about the equatorial plane. We also neglect viscosity and assume Newtonian gravity. Under these assumptions the equilibrium configuration is described by the static Euler equation:

$$\boldsymbol{v} \cdot \boldsymbol{\nabla} \boldsymbol{v} = -\frac{\boldsymbol{\nabla} P}{\rho} - \boldsymbol{\nabla} \Phi \ , \tag{2.1}$$

where P is pressure; ρ is density; Φ is the gravitational potential, which satisfies the Poisson equation

$$\nabla^2 \Phi = 4\pi G \rho \ , \tag{2.2}$$

where G is the gravitational constant. The fluid's velocity $\boldsymbol{v}$ is related to the rotational angular frequency Ω by $\boldsymbol{v} = \Omega\varpi\boldsymbol{e}_{\hat{\varphi}}$, where ϖ is the distance from the rotation axis and $\boldsymbol{e}_{\hat{\varphi}}$ is the unit vector along the azimuthal direction. The EOS we use is barotropic, i.e., $P = P(\rho)$, so the Euler equation can be integrated to give

$$h = C - \Phi + \frac{\varpi^2}{2}\Omega^2 \ , \tag{2.3}$$

where C is a constant. The enthalpy (per mass) h is given by

$$h = \int_0^P \frac{dP}{\rho} \ , \tag{2.4}$$

and is defined only inside the star. The boundary of the star is the surface with $h = 0$.

The equilibrium configuration is determined by Hachisu's self-consistent field method [15]: given an enthalpy distribution h_i, we calculate the density distribution ρ_i from the inverse of equation (2.4) and from the EOS. Next we calculate the gravitational potential Φ_i everywhere by solving the Poisson equation (2.2). Then the enthalpy is updated by

$$h_{i+1} = C_{i+1} - \Phi_i + \frac{\varpi^2}{2}\Omega_{i+1}^2 \ , \tag{2.5}$$

with C_{i+1} and Ω_{i+1}^2 determined by two boundary conditions. In Hachisu's paper [15], the axis ratio, i.e., the ratio of polar to equatorial radii, and the maximum density are fixed to determine C_{i+1} and Ω_{i+1}^2. However, we find it more convenient in our case to fix the equatorial radius R_e and central enthalpy h_c, so that

$$C_{i+1} = h_c + \Phi_i(0) \tag{2.6}$$

$$\Omega_{i+1}^2 = -\frac{2}{R_e^2}[C_{i+1} - \Phi_i(A)] \ , \tag{2.7}$$

where $\Phi_i(0)$ and $\Phi_i(A)$ are the gravitational potential at the center and at the star's equatorial surface, respectively. The procedure is repeated until the enthalpy and density distribution converge to the desired degree of accuracy.

We used a spherical grid with L radial spokes and N evenly spaced grid points along each radial spoke. The spokes are located at angles θ_i in such a way that $\cos\theta_i$ correspond to the zeros of the Legendre polynomial of order $2L-1$: $P_{2L-1}(\cos\theta_i) = 0$. Because of the reflection symmetry, we only need to consider spokes lying in the first quadrant. Poisson's equation is solved using the technique described by Ipser and Lindblom [23]. The special choice of the angular positions of the radial

spokes and the finite difference scheme make our numerical solution equivalent to an expansion in Legendre polynomials through order $l = 2L - 2$ [23]. Although the white dwarfs we consider here are rapidly rotating, the equilibrium configurations are close to spherical, as demonstrated in the next subsection. So a relatively small number of radial spokes are adequate to describe the stellar models accurately. We compare the results of $(L, N) = (10, 3000)$ with $(L, N) = (20, 5000)$ and find agreement to an accuracy of 10^{-5}. The accuracy of the model can also be measured by the Virial theorem, which states that $2T_{\rm rot} + W + 3\Pi = 0$ for any equilibrium star (see, e.g., [52]). Here $T_{\rm rot}$ is the rotational kinetic energy; W is the gravitational potential energy and $\Pi = \int P\, d^3x$. We define

$$\epsilon = \left| \frac{2T_{\rm rot} + W + 3\Pi}{W} \right| . \tag{2.8}$$

All models constructed in this section have $\epsilon \approx 10^{-7}$.

2.2.3 Results

We constructed three models of rigidly rotating white dwarfs. All of them are maximally rotating: material at the star's equatorial surface rotates at the local orbital frequency. Models I and II are C-O white dwarfs with central densities $\rho_c = 10^{10}$ g cm^{-3} and $\rho_c = 6 \times 10^9$ g cm^{-3}, respectively; Model III is an O-Ne-Mg white dwarf with $\rho_c = 4 \times 10^9$ g cm^{-3}. The properties of these white dwarfs are summarized in Table 2.1. We see that the angular momentum J decreases as the central density ρ_c increases, because the white dwarf becomes smaller and more centrally condensed. Although $T_{\rm rot}$ increases with ρ_c, $|W|$ increases at a faster rate so that $\beta = T_{\rm rot}/|W|$ decreases with increasing ρ_c. We also notice that the mass does not change much with increasing ρ_c. The reason is that massive white dwarfs are centrally condensed so their masses are determined primarily by the high density central core. Here the degenerate electron gas becomes highly relativistic and the Coulomb effects are negligible, so the composition difference is irrelevant. Hence the white dwarf behaves like an $n = 3$ polytrope, whose mass in the non-rotating case is independent of the central density.

The masses of our three models are all greater than the Chandrasekhar limit for non-rotating white dwarfs. A non-rotating C-O white dwarf with $\rho_c = 10^{10}$ g cm^{-3} has a radius $R = 1300$ km and a mass $M = 1.40 M_\odot$. When this white dwarf is spun up to maximum rotation while keeping its mass fixed, the star puffs up to an oblate figure of equatorial radius $R_e = 4100$ km and polar radius $R_p = 2700$ km, and its central density drops to $\rho_c = 5.5 \times 10^8$ g cm^{-3}. This peculiar behavior is caused by the soft EOS of relativistic degenerate electrons, which makes the star highly compressible and also highly expansible. When the angular velocity of the star is increased, the centrifugal force

Table 2.1: The central density ρ_c, mass M, angular momentum J, rotational frequency Ω, rotational kinetic energy $T_{\rm rot}$, the ratio of rotational kinetic to gravitational energies β, equatorial radius R_e and polar radius R_p of three rigidly and maximally rotating white dwarfs.

	ρ_c	M	J	Ω	$T_{\rm rot}$	β	R_e	R_p
	g cm^{-3}	$M_\odot$	g cm^2 s^{-1}	rad s^{-1}	erg		km	km
Model I	10^{10}	1.47	3.12×10^{49}	5.37	8.38×10^{49}	0.015	1895	1247
Model II	6×10^9	1.46	3.51×10^{49}	4.32	7.57×10^{49}	0.017	2189	1439
Model III	4×10^9	1.45	3.80×10^{49}	3.65	6.94×10^{49}	0.018	2441	1602

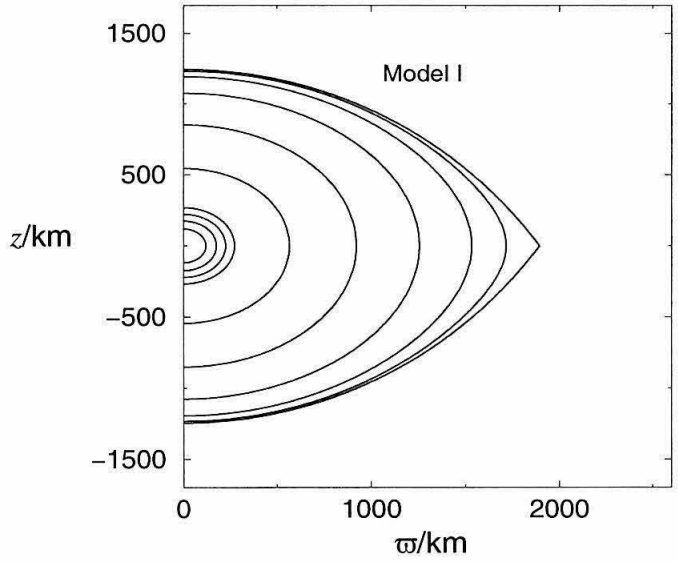

Figure 2.1: Meridional density contours of the rotating white dwarf of Model I. The contours, from inward to outward, correspond to densities ρ/ρ_c =0.8, 0.6, 0.4, 0.2, 0.1, 10^{-2}, 10^{-3}, 10^{-4}, 10^{-5} and zero.

causes a large reduction in central density, resulting in a dramatic increase in the overall size of the star.

Figures 2.1-2.3 display the density contours of our three models. The contours in the high density region remain more or less spherical even though our models represent the most rapidly rotating cases. The effect of rotation is only to flatten the density contours of the outer region in which the density is relatively low. This suggests that the white dwarfs are centrally condensed, and is clearly demonstrated in Figure 2.4, where the cylindrical mass fraction

$$m_\varpi = \frac{2\pi}{M} \int_0^\varpi d\varpi'\, \varpi' \int_{-\infty}^{\infty} dz'\, \rho(\varpi', z') \tag{2.9}$$

is plotted. In all of our three models, more than half of the mass is concentrated inside the cylinder with $\varpi \approx 0.2 R_e$.

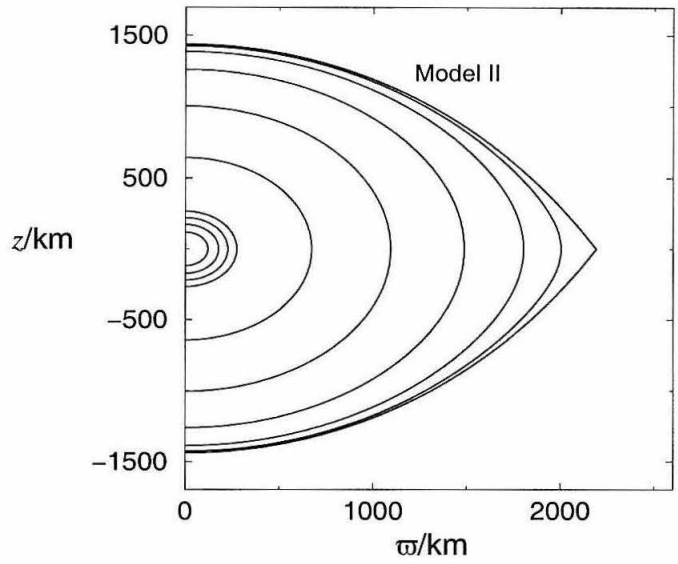

Figure 2.2: Same as Figure 2.1 but for Model II.

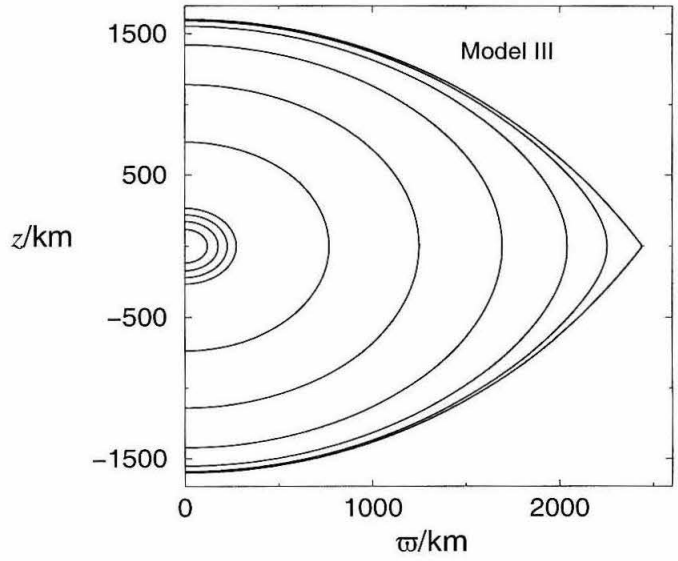

Figure 2.3: Same as Figure 2.1 but for Model III.

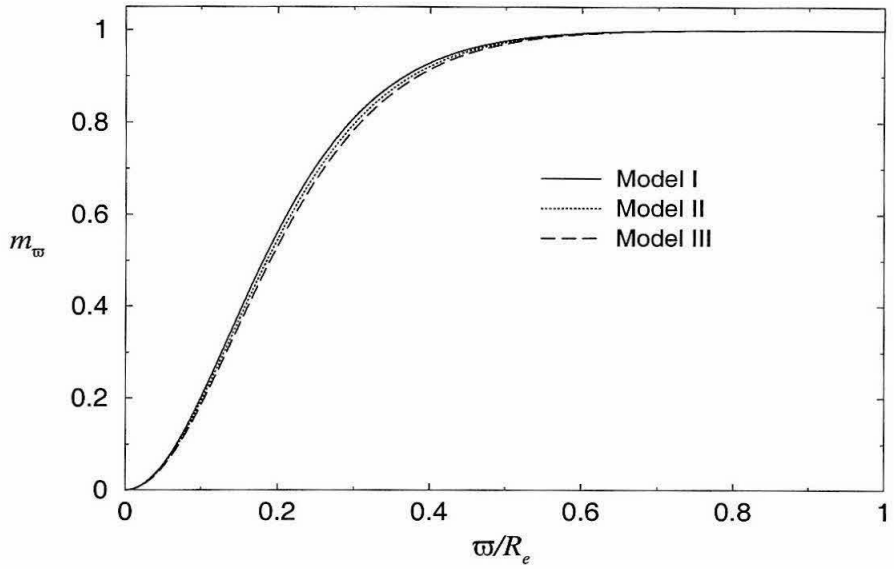

Figure 2.4: Cylindrical mass fraction m_ϖ as a function of ϖ. Solid line corresponds to Model I; dotted line, Model II, and dashed line, Model III.

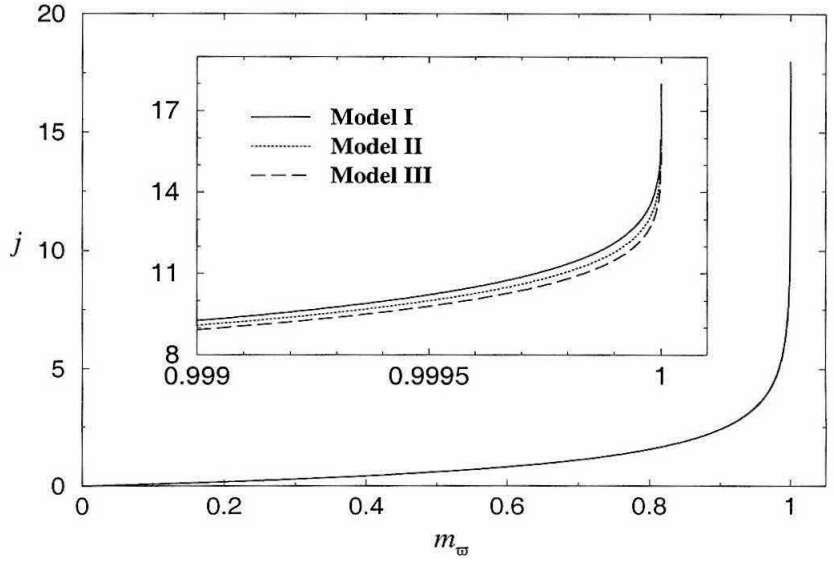

Figure 2.5: Normalized specific angular momentum j as a function of the cylindrical mass fraction m_ϖ. The curves for the three models are indistinguishable except in the region very close to $m_\varpi = 1$, which is magnified in the inset.

Table 2.2: The outer layers of Model I white dwarf. J_ϖ is the angular momentum of the material inside the cylinder of radius ϖ.

ϖ/R_e	$1-m_\varpi$	$1-J_\varpi/J$	$j(m_\varpi)/j(1)$
0.83	7.5×10^{-5}	100×10^{-5}	0.69
0.86	3.5×10^{-5}	49×10^{-5}	0.73
0.90	0.65×10^{-5}	9.8×10^{-5}	0.81
0.95	0.027×10^{-5}	0.45×10^{-5}	0.90

Figure 2.5 shows the specific angular momentum j as a function of the cylindrical mass fraction m_ϖ, normalized so that $\int_0^1 j(m_\varpi)\,dm_\varpi = 1$. The $j(m_\varpi)$-curves for the three models are almost indistinguishable except in the region where $m_\varpi \approx 1$. The spike of the curve near $m_\varpi = 1$ can be understood from Figure 2.4, where we see that $m_\varpi \approx 1$ when $\varpi/R_e \gtrsim 0.6$. However, $j = (M/J)\Omega\varpi^2 \propto \varpi^2$. These two make the values of j in the interval $0.6^2 \lesssim j/j(m_\varpi = 1) \leq 1$ squeeze to the region $m \approx 1$, and the spike results. We shall point out in the next section that this spike causes a serious numerical problem in the construction of the equilibrium models of the collapsed objects. The problem can be solved by truncating the upper part of the $j(m_\varpi)$ curve. The physical justification is that the material in the outer region contributes only a very small fraction of the total mass and angular momentum of the star, as illustrated in Table 2.2 for Model I. The situations for the other two models are very similar and so are not shown. We see that material in the region where $\varpi/R_e > 0.9$ $[j(m_\varpi)/j(1) > 0.81]$ contributes less than 10^{-5} of the total mass and 10^{-4} of the total angular momentum. So the upper 19% of the $j(m_\varpi)$-curve has little influence to the inner structure of the collapsed star. While this region is important for the structure of the star's outer layers, that part of the star is not of our primary interest since the mass there is too small to develop any instability that can produce a substantial amount of gravitational radiation.

2.3 Collapsed objects

In this section, we present the equilibrium new-born neutron-star models that may result from the collapse of the three white dwarfs computed in the previous section. Instead of performing hydrodynamic simulations, we adopt a simpler approach.

First, we assume the collapsed stars are axisymmetric and are in rotational equilibrium with no meridional circulation. Second, we assume the EOS is barotropic, $P = P(\rho)$. These two assumptions imply that (1) the angular velocity Ω is a function of ϖ only, i.e. $\partial\Omega/\partial z = 0$, and (2) the Solberg condition is satisfied, which states that $dj/d\varpi > 0$ for stable barotropic stars in rotational equilibrium

(see, e.g., Tassoul 1978). The angular velocity profile ($\partial\Omega/\partial z = 0$) is observed in the simulations of Mönchmeyer, Janka and Müller (Mönchmeyer and Müller 1988; Janka and Mönchmeyer 1989ab). Third, we are only interested in the structure of the neutron stars within a few minutes after core bounce. The timescale is much shorter than any of the viscous timescales, so viscosity does not have time to change the angular momentum of a fluid particle [9, 45, 28, 17, 14]. Finally, we assume no material is ejected during the collapse. It follows, from the conservation of j and the fact that j is a function of ϖ only before and after collapse, that all particles initially located on a cylindrical surface of radius ϖ_1 from the rotation axis will end up being on a new cylindrical surface of radius ϖ_2. And the Solberg condition ensures that all particles initially inside the cylinder of radius ϖ_1 will collapse to the region inside the new cylinder of radius ϖ_2. Hence the specific angular momentum distribution $j(m_\varpi)$ of the new equilibrium configuration is the same as that of the pre-collapse white dwarf; here m_ϖ is the cylindrical mass fraction defined by equation (2.9).

Based on these assumptions, we constructed equilibrium models of the collapsed objects with the same masses, total angular momenta and $j(m_\varpi)$ as the pre-collapse white dwarfs.

2.3.1 Equations of state

The gravitational collapse of a massive white dwarf is halted when the central density reaches nuclear density where the EOS becomes stiff. The core bounces back, and within a few milliseconds, a hot ($T \gtrsim 20$ Mev), lepton rich protoneutron star settles into hydrodynamic equilibrium. During the so-called Kelvin-Helmholtz cooling phase, the temperature and lepton number decrease due to neutrino emission and the protoneutron star cools to a cold neutron star with temperature $T < 1$ Mev after several minutes. Since the cooling timescale is much longer than the hydrodynamical timescale, the protoneutron star can be regarded as in quasi-equilibrium.

The EOS of a protoneutron star is expressed in the form $P = P(\rho; s, Y_e)$, where s and Y_e are the entropy per baryon and lepton fraction, respectively. As pointed out by Strobel, Scraab and Weigel [51], the structure of a protoneutron star can be approximated by a constant s and Y_e throughout the star, resulting in an effectively barotropic EOS.

We used two different EOS for densities above 10^{10} g cm^{-3}. The first is one of the standard EOS for cold neutron stars. We adopt the Bethe-Johnson EOS [2] for densities above 10^{14} g cm^{-3}, and BBP EOS [1] for densities in the region 10^{11} g cm^{-3} $-$ 10^{14} g cm^{-3}. It turns out that the densities of these collapsed stars are lower than 4×10^{14} g cm^{-3}, and ideas about the EOS in this range have

not changed very much since 1970's. The second is the EOS $\mathrm{LPNS}^{s2}_{\mathrm{YL04}}$ of Strobel et al. [51][1]. This corresponds to a protoneutron star 0.5–1 s after core bounce. It has an entropy per baryon $s = 2k_{\mathrm{B}}$ and a lepton fraction $Y_e = 0.4$, where k_{B} is Boltzmann's constant. We join both EOS to that of the pre-collapse white dwarf for densities below 10^{10} g cm^{-3}. Hereafter, we shall call the first EOS the cold EOS, and the second one, the hot EOS.

2.3.2 Numerical method

We compute the equilibrium structure by Hachisu's self-consistent field method modified so that $j(m_\varpi)$ can be specified [48]. The iteration scheme is based on the integrated static Euler equation (2.1) written in the form

$$h(\varpi, z) = C - \Phi(\varpi, z) + \left(\frac{J}{M}\right)^2 \int_0^\varpi d\varpi' \frac{j^2(m_{\varpi'})}{\varpi'^3} \ , \tag{2.10}$$

where C is the integration constant, and M and J are the total mass and angular momentum of the star respectively. Given an enthalpy distribution h_i everywhere, the density distribution ρ_i is calculated by the EOS and the inverse of equation (2.4). Next we compute the mass M_i and cylindrical mass fraction $m_{\varpi,i}$ by

$$\begin{aligned} M_i &= 4\pi \int_0^\infty d\varpi' \varpi' \int_0^\infty dz' \rho_i(\varpi', z') \\ m_{\varpi,i} &= \frac{4\pi}{M_i} \int_0^\varpi d\varpi' \varpi' \int_0^\infty dz' \rho_i(\varpi', z') \ , \end{aligned} \tag{2.11}$$

and solve the Poisson equation $\nabla^2 \Phi_i = 4\pi G \rho_i$ to obtain the gravitational potential Φ_i. We then update the enthalpy by equation (2.10):

$$h_{i+1}(\varpi, z) = C_{i+1} - \Phi_i(\varpi, z) + \left(\frac{J_{i+1}}{M_{i+1}}\right)^2 \int_0^\varpi d\varpi' \frac{j^2(m_{\varpi',i})}{\varpi'^3} \ , \tag{2.12}$$

with the parameters C_{i+1} and $(J_{i+1}/M_{i+1})^2$ determined by specifying the central density ρ_c and equatorial radius R_e. The procedure is repeated until the enthalpy and density distribution converge to the desired degree of accuracy.

To construct the equilibrium configuration with the same total mass and angular momentum as a pre-collapse white dwarf, we first compute a model of a non-rotating spherical neutron star, use its enthalpy distribution as an initial guess for the iteration scheme described above and build a

[1]The tabulated EOS is obtained from http://www.physik.uni-muenchen.de/sektion/suessmann/astro/eos/.

configuration with slightly different ρ_c or R_e. Then the parameters ρ_c and R_e are adjusted until we end up with a configuration having the correct total mass and angular momentum.

Two numerical problems were encountered in this procedure. The first problem is that when the angular momentum J is increased, the star becomes flattened, and the iteration often oscillates among two or more states without converging. This problem can be solved by using a revised iteration scheme suggested by Pickett, Durisen and Davis [40], in which only a fraction of the revised enthalpy h_{i+1}, $h'_{i+1} = (1-\delta)h_{i+1} + \delta h_i$, is used for the next iteration. Here $\delta < 1$ is a parameter controlling the change of enthalpy. We need to use $\delta > 0.95$ for very flattened configurations, and it takes $100 - 200$ iterations for the enthalpy and density distributions to converge.

The second problem has to do with the spike of the $j(m_\varpi)$-curve near $m_\varpi = 1$ (see Figure 2.5). The slope is so steep that it makes the iteration unstable. As discussed in Section 2.2.3, the material in the region very close to $m_\varpi = 1$ contains a very small amount of mass and angular momentum, so we can truncate the last part of the $j(m_\varpi)$-curve without introducing much error. Specifically, we set a parameter $j_c < j(m_\varpi = 1)$, compute a quantity m_c which satisfies $j(m_c) = j_c$. Then we use the specific angular momentum distribution $\tilde{j}(m_\varpi) = j(m_\varpi\, m_c)$ instead of $j(m_\varpi)$. Typically, we choose $j_c/j(1) = 0.81$ so that $1 - m_c \approx 10^{-5}$ (see Table 2.2). Hence the distributions $\tilde{j}(m_\varpi)$ and $j(m_\varpi)$ are basically the same except in the star's outermost region, which is unimportant to the inner structure the star, and presumably also unimportant for the star's dynamical and secular stabilities. We also tried several different values of j_c and found that the change of physical properties of the collapsed objects (e.g., the quantities in Table 2.3) are within the error due to our finite-size grid. Thus the truncation is also justified numerically.

We evaluate these stellar models on a cylindrical grid. This allows us to compute the integrals in equations (2.11) and (2.12) easily. We find it more convenient however, to solve the the Poisson equation for the gravitational potential on a spherical grid using the method described by Ipser and Lindblom [23]. We have verified that the potential obtained in this way agrees with the result obtained with a cylindrical multi-grid solver to within 0.5%. However, the spherical grid solver (including the needed transformation from one grid to the other) is much faster than the cylindrical grid solver. The accuracy of our final equilibrium models can also be measured by the quantity ϵ defined in equation (2.8). The values of ϵ for models computed in this section are few times 10^{-4}.

Table 2.3: The central density ρ_c, radius of gyration R_g, characteristic radius R_* and ratio of rotational kinetic energy to gravitational energy β of the collapsed objects with the cold and the hot EOS.

	ρ_c g cm^{-3}	R_g km	R_* km	β
Model I (cold EOS)	3.7×10^{14}	63	670	0.230
Model I (hot EOS)	1.4×10^{14}	67	650	0.139
Model II (cold EOS)	3.5×10^{14}	78	800	0.246
Model II (hot EOS)	0.79×10^{14}	85	800	0.137
Model III (cold EOS)	3.2×10^{14}	94	940	0.261
Model III (hot EOS)	0.27×10^{14}	110	940	0.127

2.3.3 Results

Table 2.3 shows some properties of the collapsed objects resulting from the collapse of the three white dwarfs in Section 2.2. We define the radius of gyration, R_g, and the characteristic radius, R_*, of the star by

$$MR_g^2 = \int \rho \varpi^2 \, d^3x \tag{2.13}$$

$$m_\varpi(\varpi = R_*) = 0.999 \, . \tag{2.14}$$

We see that R_g and R_* that result from the same initial white dwarfs are insensitive to the neutron-star EOS, while there is a dramatic difference in the central density ρ_c and the ratio of rotational kinetic energy to gravitational potential energy β. The collapsed stars with the hot EOS have smaller ρ_c and β than those with the cold EOS. In fact, the central densities of these hot stars are less than nuclear density. It is well known that a non-rotating star cannot have a central density in the subnuclear density regime (4×10^{11} g cm$^{-3} \lesssim \rho \lesssim 2 \times 10^{14}$ g cm^{-3}) because the EOS is too soft to render the star stable against gravitational collapse. It has been suggested that if rotation is taken into account, a star with a central density in this regime can exist. Such stars are termed "fizzlers" in the literature [46, 55, 11, 33, 16, 22]. However, these so-called fizzlers in our case can exist for only about 20 s before evolving to rotating cold neutron stars. In order to build a stable cold model in the subnuclear density regime, the collapsed star has to rotate much faster, which is impossible unless the pre-collapse white dwarf is highly differentially rotating.

We mention in Section 2.1 that Zwerger and Müller [58] performed 2-D hydrodynamic simulations of axisymmetric rotational core collapse. Their pre-collapse models are rotating stars with $n = 3$ polytropic EOS, which is close to the real EOS of a massive white dwarf. All of their pre-collapse

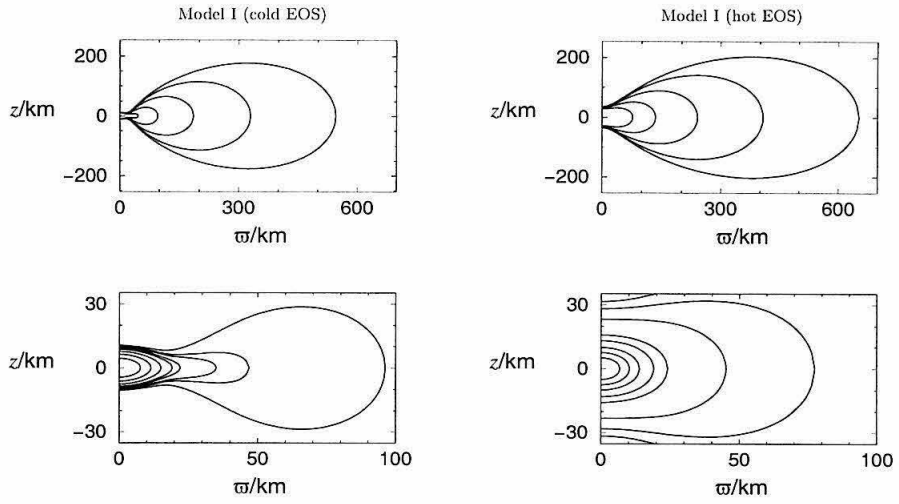

Figure 2.6: Meridional density contours of the neutron stars resulting from the collapse of Model I white dwarf. The left graphs correspond to the cold EOS, and the right graphs, the hot EOS. The contours in the upper graphs denote, from inward to outward, $\rho/\rho_c = 10^{-3}$, 10^{-4}, 10^{-5}, 10^{-6}, and 10^{-7}. The contours in the lower graphs denote, from inward to outward, ρ/ρ_c =0.8, 0.6, 0.4, 0.2, 0.1, 10^{-2}, 10^{-3} and 10^{-4}.

models have a central density of 10^{10} g cm^{-3} (see their Table 1). The model A1B3 in their paper is the fastest (almost) rigidly rotating star, but its total angular momentum J and β are respectively 22% and 40% less than those of our Model I of the pre-collapse white dwarf, though both have the same central density. This suggests that the structure of a massive white dwarf is sensitive to the EOS. Zwerger and Müller state in their paper that no equilibrium configuration exists that has $\beta > 0.01$ for the (almost) rigidly rotating case. This assertion is confirmed by our numerical code. Zwerger and Müller adopt a simplified analytical EOS for the collapsing core. At the end of their simulations, the models A1B3G1-A1B3G5, corresponding to the collapsed models of A1B3, have values of β less than 0.07, far smaller than the β's of our collapsed model I (see Table 2.3), indicating that the EOS of the collapsed objects also play an important role on the final equilibrium configurations (or that their analysis violates one of our assumptions).

Figures 2.6-2.8 show the density contours of the collapsed objects. We see that the contours of the dense central region look like the contours of a typical rotating star. As we go out to the low density region, the shapes of the contours become more and more disk-like. Eventually, the contours turn into torus-like shapes for densities lower than $10^{-4}\rho_c$. In all cases, the objects contain two regions: a dense central core of size about 20 km and a low density torus-like envelope extending

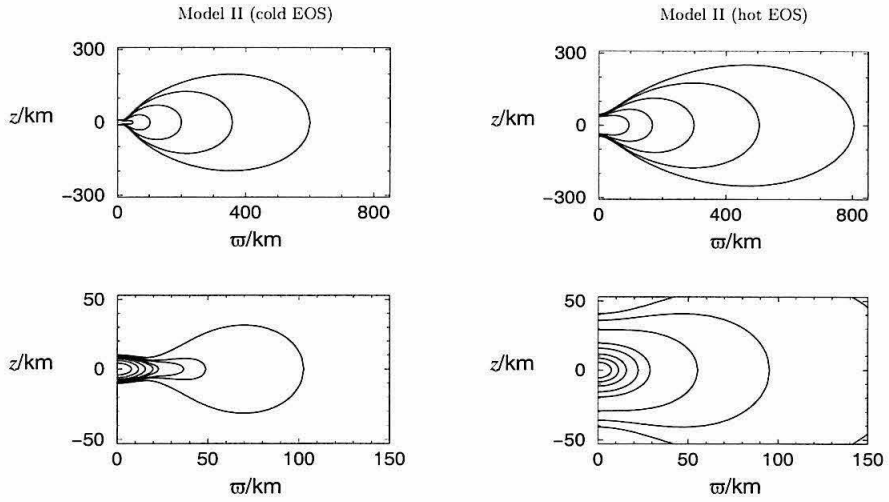

Figure 2.7: Same as Figure 2.6 but for Model II.

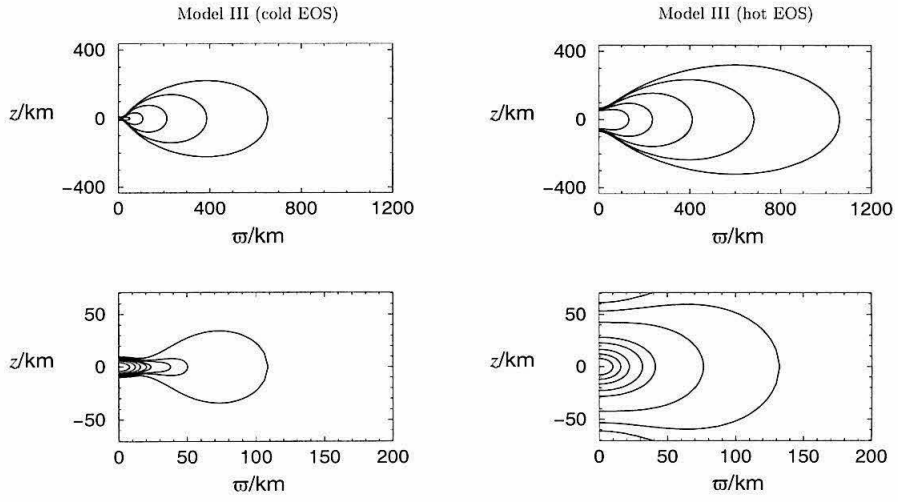

Figure 2.8: Same as Figure 2.6 but for Model III.

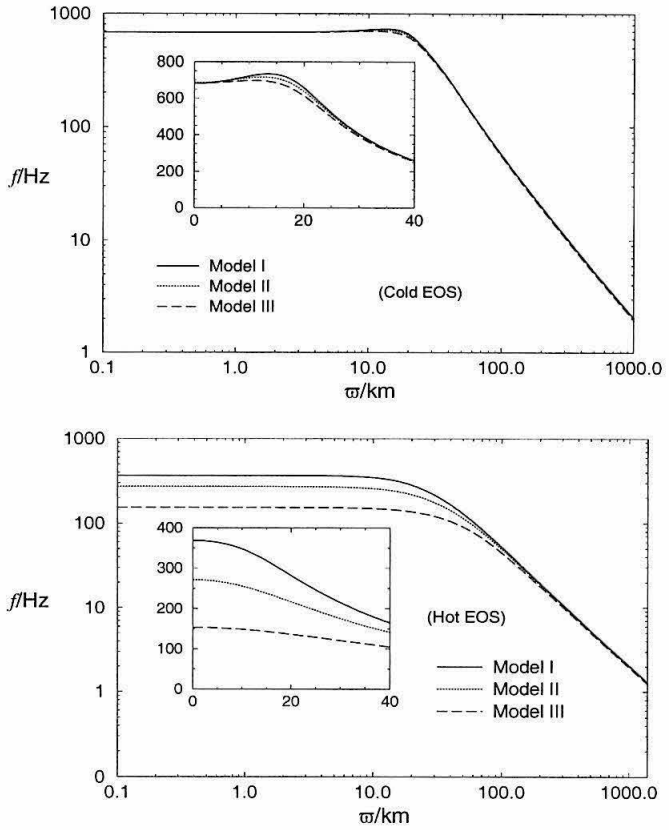

Figure 2.9: Rotational frequency f as a function ϖ for the cold models (upper graph) and the hot models (lower graph). The inset in each graph shows f in linear scale in the central region.

out to 1000 km from the rotation axis. Since we truncate the $j(m_\varpi)$-curve, we cannot determine accurately the actual boundary of the stars. The contours shown in these figures have been checked to move less than one per cent as the cutoff $j_c/j(1)$ is changed from 0.7 to 0.9. This little change is hardly visible at the displayed scales.

Figure 2.9 shows the rotational frequency $f \equiv \Omega/2\pi$ as a function of ϖ, the distance from the rotation axis. We see that the cores of the cold models are close to rigid rotation. The rotation periods of the cores of the cold neutron stars are all about 1.4 ms, slightly less than the period of the fastest observed millisecond pulsar (1.56 ms). A further analysis reveals that $f \propto \varpi^{-\alpha}$ in the region $\varpi \gtrsim 100$ km, where $\alpha \approx 1.5$ for the cold models and $\alpha \approx 1.4$ for the hot models.

To gain an insight into the structure of the envelope, we define the Kepler frequency Ω_K at a given point on the equator as the angular frequency required for a particle to be completely supported by centrifugal force, i.e., Ω_K satisfies the equation $\Omega_K^2 \varpi = g$, where g is the magnitude of gravitational

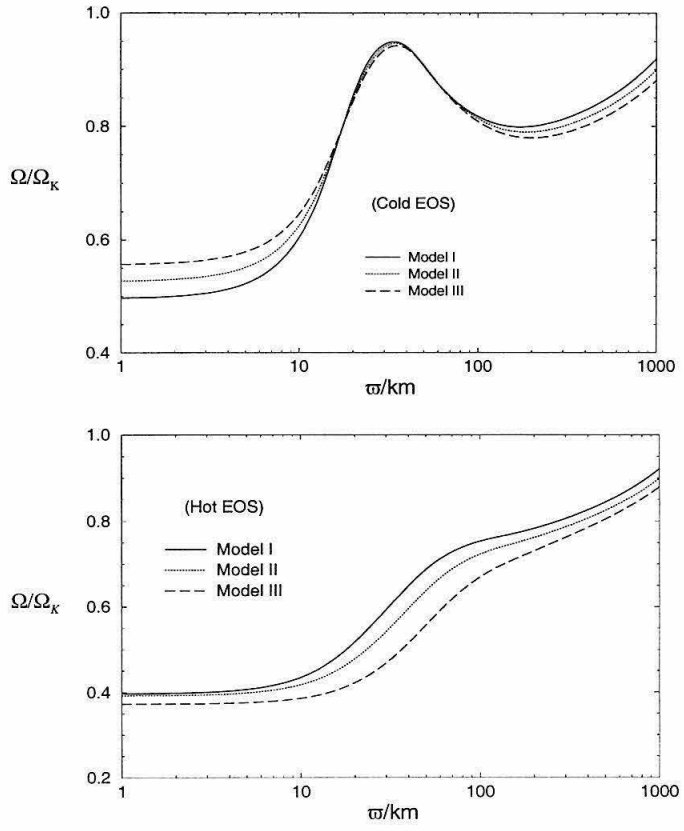

Figure 2.10: The ratio Ω/Ω_K along the equator as a function of ϖ for the cold models (upper graph) and the hot models (lower graph).

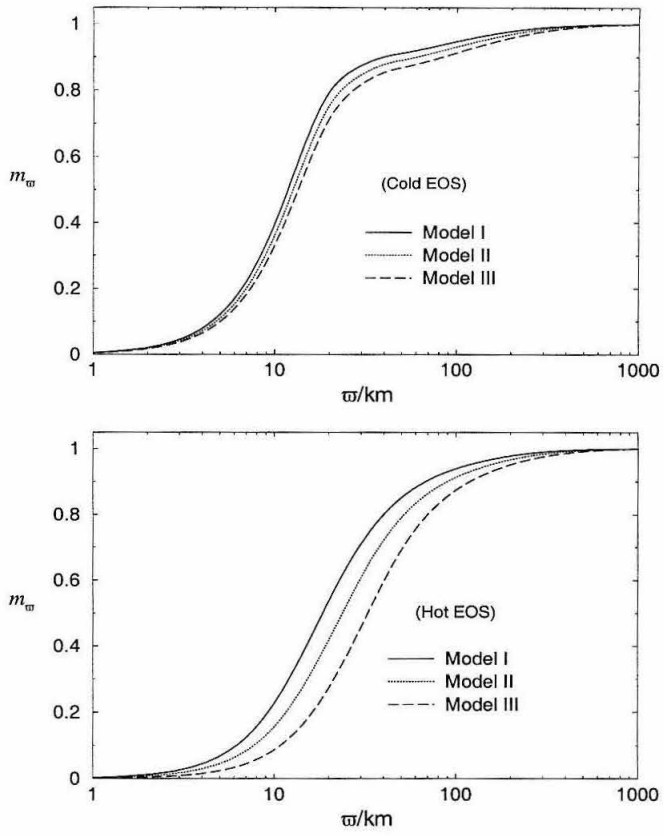

Figure 2.11: Cylindrical mass fraction m_ϖ as a function of ϖ for the cold models (upper graph) and the hot models (lower graph).

acceleration at that point. Figure 2.10 plots Ω/Ω_K as a function of ϖ along the equator. For the cold models, the curves increase from 0.5 at the center to a maximum of about 0.95 at $\varpi \approx 35$ km, then decrease to a local minimum of about 0.8, and then gradually increase in the outer region. The curves of the hot models, on the other hand, increase monotonically from about 0.4 at the center to over 0.7 in the outer region. In all cases, centrifugal force plays an important role in the structure of the stars, especially in the low density region.

Figure 2.11 plots the cylindrical mass fraction m_ϖ as a function of ϖ. In all cases the cores contain most of the stars' mass. Material in the region $\varpi \gtrsim 200$ km occupies only a few per cent of the total mass, but it is massive enough that its self-gravity cannot be neglected in order to compute the structure of the envelope accurately. The envelope can be regarded as a massive, self-gravitating accretion torus. The same structure is also observed in the core collapse simulations of Janka and Mönchmeyer [25] and Fryer and Heger (private communication with Fryer).

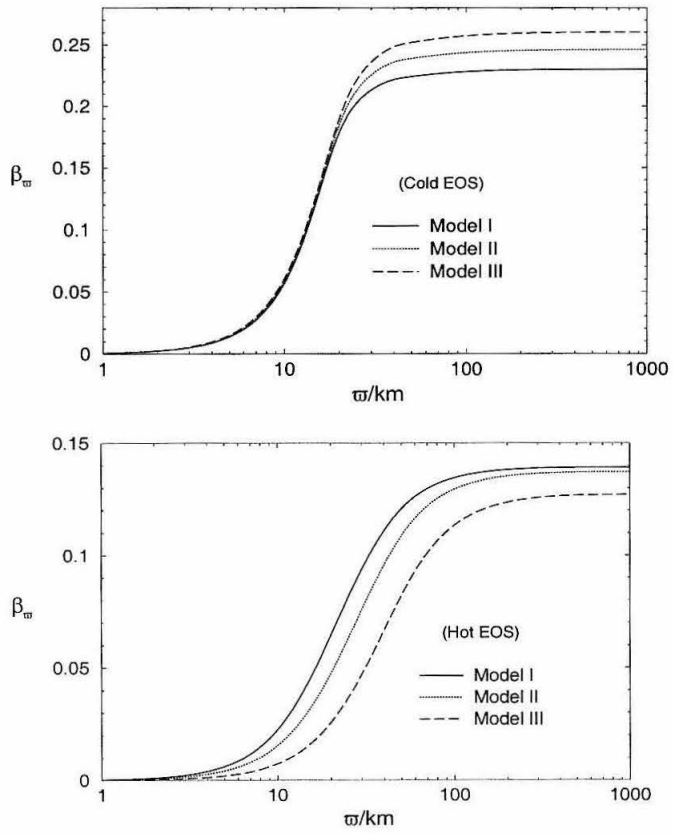

Figure 2.12: The quantity β_ϖ as a function of ϖ for the cold models (upper graph) and the hot models (lower graph).

Figure 2.12 shows $\beta_\varpi = T_{\rm rot}(\varpi)/|W(\varpi)|$ as a function of ϖ, where $T_{\rm rot}(\varpi)$ and $W(\varpi)$ are the rotational kinetic energy and gravitational potential energy inside the cylinder of radius ϖ, i.e.,

$$T_{\rm rot}(\varpi) = 2\pi \int_0^{\varpi} d\varpi' \varpi' (\Omega \varpi')^2 \int_0^{\infty} dz' \rho(\varpi', z') \tag{2.15}$$

$$W(\varpi) = 2\pi \int_0^{\varpi} d\varpi' \varpi' \int_0^{\infty} dz' \rho(\varpi', z') \Phi(\varpi', z') \ . \tag{2.16}$$

The values of β_ϖ approach β when $\varpi \gtrsim 40$ km for the cold EOS models and when $\varpi \gtrsim 100$ km for the hot EOS models. This suggests that material in the region $\varpi \gtrsim 100$ km contains negligible amount of kinetic energy, and any instability developed in this region could not produce strong gravitational waves.

2.4 Stability of the collapsed objects

We first consider axisymmetric instabilities, i.e., axisymmetric collapse. This stability is verified when we construct the models. Recall that we start from the model of a non-rotating spherical star which is stable. Then we use it as an initial guess to build a sequence of rotating stellar models with the same specific angular momentum distribution but different total masses and angular momenta. If the final model we end up with is unstable against axisymmetric perturbations, there must be at least one model in the sequence such that

$$q \equiv \left. \frac{\partial M}{\partial \rho_c} \right|_{j(m_\varpi), J} = 0 \ , \tag{2.17}$$

which signals the onset of instability [3]. Here M is the total mass and ρ_c is the central density. The partial derivative is evaluated by keeping the total angular momentum J and specific angular momentum distribution $j(m_\varpi)$ fixed. We have verified that all of our equilibrium models in the sequences satisfy $q > 0$. Hence they are all stable against axisymmetric perturbations.

We next consider non-axisymmetric instabilities. We have $\beta = 0.23 - 0.26$ for the cold EOS models and $\beta = 0.13 - 0.14$ for the hot EOS models (Table 2.3). The hot models are probably dynamically stable but may be secularly unstable. However, since they are evolving to cold neutron stars in about 20 s and their structures are continually changing on times comparable to the secular timescale, we shall not discuss secular instabilities of these hot models here.

The values of β for the three cold neutron stars are slightly less than the traditional critical value for dynamical instability, $\beta_d \approx 0.27$. This critical value is based on simulations of differentially

rotating polytropes having the $j(m_\varpi)$-distribution of Maclaurin spheroids. However, recent simulations demonstrate that differentially rotating polytropes having other $j(m_\varpi)$-distributions can be dynamically unstable for values of β as low as 0.14 [40, 7]. The equilibrium configurations of some of those unstable stars also contain a low density accretion disk like structure in the stars' outer layers. This feature is very similar to the equilibrium structure of our models. Hence a more detailed study has to be carried out to determine whether the cold models are dynamically stable.

The subsequent evolution of a bar-unstable object has been studied for the past 15 years [10, 57, 19, 40, 49, 18, 35, 22, 5]. It is found that a bar-like structure develops in a dynamical timescale. However, it is still not certain whether the bar structure would be persistent, giving rise to a long-lived gravitational wave signal, or material would be shed from the ends of the bar after tens of rotation periods, leaving an axisymmetric, dynamically bar-stable central star.

Even if the cold neutron stars are dynamically stable, they are subject to various secular instabilities. The timescale of the gravitational-wave-driven bar-mode instability can be estimated by [13]

$$\tau_{\rm bar} = 0.1 \text{ s} \left(\frac{\rm R}{35 \text{ km}}\right)^{-5} \left(\frac{\Omega}{4000 \text{ rad s}^{-1}}\right)^{-6} \left(\frac{\beta - \beta_{\rm s}}{0.1}\right)^{-5} . \tag{2.18}$$

In our case, $R \approx 35$ km (see Figure 2.12), $\Omega \approx 4000$ rad s^{-1} and $\beta \approx 0.24$, so $\tau_{\rm bar} \sim 0.1$ s. Gravitational waves may also drive the r-mode instability [29]. The timescale is estimated by

$$\tau_{\rm r} = 7.3 \text{ s} \left(\frac{\bar{\rho}}{10^{14} \text{ g cm}^{-3}}\right)^{3} \left(\frac{\Omega}{4000 \text{ rad s}^{-1}}\right)^{-6} \tag{2.19}$$

for the $l = 2$ r-mode at low temperatures [30], where $\bar{\rho}$ is the average density. Inserting $\bar{\rho}$ for the inner 20 km cores of the cold stars, we have $\tau_r \approx 10 \text{ s} \gg \tau_{\rm bar}$. The evolution of the bar-mode secular instability has only been studied in detail for the Maclaurin spheroids. These objects evolve through a sequence of deformed non-axisymmetric configurations eventually to settle down as a more slowly rotating stable axisymmetric star [27, 26]. It is generally expected that stars having more realistic EOS will behave similarly.

2.5 Conclusions

We have constructed equilibrium models of differentially rotating neutron stars which model the end products of the accretion induced collapse of rapidly rotating white dwarfs. We considered three models for the pre-collapse white dwarfs. All of them are rigidly rotating at the maximum

possible angular velocities. The white dwarfs are described by the EOS of degenerate electrons at zero temperature with Coulomb corrections derived by Salpeter [43].

We assumed that (1) the collapsed objects are axisymmetric and are in rotational equilibrium with no meridional circulation, (2) the EOS is barotropic, (3) viscosity can be neglected, and (4) any ejected material carries negligible amounts of mass and angular momentum. We then built the equilibrium models of the collapsed stars based on the fact that their final configurations must have the same masses, total angular momenta and specific angular momentum distributions, $j(m_\varpi)$, as the pre-collapse white dwarfs.

Two EOS have been used for the collapsed objects. One of them is one of the standard cold neutron-star EOS. The other is a hot EOS suitable for protoneutron stars, which are characterized by their high temperature and high lepton fraction.

The equilibrium structure of the collapsed objects in all of our models consists of a high density central core of size about 20 km, surrounded by a massive accretion torus extending over 1000 km from the rotation axis. More than 90% of the stellar mass is contained in the core and core-torus transition region, which is within about 100 km from the rotation axis (see Figure 2.11). The central densities of the hot protoneutron stars are in the subnuclear density regime (4×10^{11} g cm$^{-3} \lesssim \rho \lesssim 2 \times 10^{14}$ g cm^{-3}). The structures of these protoneutron stars are very different from those of the cold neutron stars, which the protoneutron stars will evolve to in roughly 20 s. The protoneutron stars have lower central densities, rotate less rapidly, and have smaller values of β. On the other hand, the structures of the three cold neutron stars are similar. Their central densities are around 3.5×10^{14} g cm^{-3} and their central cores are nearly rigidly rotating with periods of about 1.4 ms, slightly less than the fastest observed millisecond pulsar (1.56 ms).

Zwerger and Müller [58] performed 2-D simulations of the core collapse of massive stars. The major difference between their models and ours is that they used rather simplified EOS for both the pre-collapse and the collapsed models. When compared with their fastest rigidly rotating model, AlB3, we found their pre-collapse star has less total angular momentum and smaller β than the pre-collapse white dwarf of our Model I, although both have the same central density. The differences between their final collapsed models (A1B3G1-A1B3G5) and ours are even more significant. The values of β of our collapsed objects are much larger than theirs, suggesting that the EOS plays an important role in the equilibrium configurations of both the pre-collapse white dwarfs and the resulting collapsed stars.

The values of β of the cold neutron stars are only slightly less than the traditional critical value

of dynamical instability, 0.27, frequently quoted in the literature. The cold neutron stars may still be dynamically unstable and a detailed study is required to settle the issue. Even if they are dynamically stable, they are still subject to various kinds of secular instabilities. A rough estimate suggests that the gravitational-wave driven bar-mode instability dominates. The timescale of this instability is about 0.1 s.

Acknowledgements

We thank Kip Thorne and Chris Fryer for stimulating discussions. This research was supported by NSF grants PHY-9796079, PHY-9900776, and AST-9731698 and NASA grant NAG5-4093.

Bibliography

[1] G. Baym, H. A. Bethe and C. J. Pethick, Nucl. Phys. A, **175**, 225 (1971).

[2] H. A. Bethe and M. B. Johnson, Nucl. Phys. A, **230**, 1 (1974).

[3] G. S. Bisnovatsyi-Kogan and S. I. Blinnikov, Astro. & Astrophys., **31**, 391 (1974).

[4] E. Bravo and D. García-Senz, Mon. Not. Roy. Astro. Soc., **307**, 984 (1999).

[5] J. D. Brown, Phys. Rev. D, **62**, 084024 (2000).

[6] A. Burrows and J. M. Lattimer, Astrophys. J., **307**, 178 (1986).

[7] J. M. Centrella, K. C. B. New, L. L. Lowe and J. D. Brown, Astrophys. J. Lett., **550**, 193 (2001).

[8] S. Chandrasekhar, *Ellipsoidal Figures of Equilibrium* (New Haven: Yale University Press 1969).

[9] C. Cutler and L. Lindblom, Astrophys. J., **314**, 234 (1987).

[10] R. H. Durisen, R. A. Gingold, J. E. Tohline and A. P. Boss, Astrophys. J., **305**, 281 (1986).

[11] Y. Eriguchi Y. and E. Müller, Astro. & Astrophys., **147**, 161 (1985).

[12] L. S. Finn and C. R. Evans, Astrophys. J., **351**, 588 (1990).

[13] J. L. Friedman and B. F. Schutz, Astrophys. J., **199**, L157 (1975); J. L. Friedman and B. F. Schutz, Astrophys. J., **221**, L99 (1978).

[14] B. T. Goodwin and C. J. Pethick, Astrophys. J., **253**, 816 (1982).

[15] I. Hachisu, Astrophys. J. Supp., **61**, 479 (1986).

[16] A. Hayashi, Y. Eriguchi and M. Hashimoto, Astrophys. J., **492**, 286 (1998).

[17] L. J. van den Horn and Ch. G. van Weert, Astrophys. J., **251**, L97 (1981).

[18] J. L. Houser, Mon. Not. Roy. Astro. Soc., **299**, 1069 (1998).

[19] J. L. Houser and J. M. Centrella, Phys. Rev. D., **54**, 7278 (1996).

[20] J. L. Houser, J. M. Centrella and S. C. Smith, Phys. Rev. Lett., **72**, 1314, 1994.

[21] J. N. Imamura and J. Toman, Astrophys. J, **444**, 363 (1995).

[22] J. N. Imamura, R. H. Durisen and B. K. Pickett, Astrophys. J., **528**, 946 (2000).

[23] J. R. Ipser and L. Lindblom, Astrophys. J., **355**, 226 (1990).

[24] H.-Th. Janka and R. Mönchmeyer, Astro. & Astrophys., **209**, L5 (1989)

[25] H.-Th. Janka and R. Mönchmeyer, Astro. & Astrophys., **226**, 69 (1989).

[26] D. Lai and S. L. Shapiro, Astrophys. J., **442**, 259 (1995).

[27] L. Lindblom and S. L. Detweiler , Astrophys. J., **211**, 565 (1977).

[28] L. Lindblom and S. L. Detweiler, Astrophys. J., **232**, L101 (1979).

[29] L. Lindblom, B. J. Owen and S. M. Morsink, Phys. Rev. Lett., **80**, 4843 (1998).

[30] L. Lindblom, G. Mendell and B. J. Owen, Phys. Rev. D, **60**, 064006 (1999).

[31] R. Mönchmeyer and E. Müller, in NATO ASI on *Timing Neutron Stars*, ed. Ögelman H., D. Reidel Publ. Comp., Dordrecht (1988).

[32] R. Mönchmeyer, G. Schäfer, E. Müller and R. E. Katea, Astro. & Astrophys., **246**, 417 (1991).

[33] E. Müller and Y. Eriguchi, Astro. & Astrophys., **152**, 325 (1985).

[34] E. Müller and W. Hillebrandt, Astro. & Astrophys., **103**, 358 (1981).

[35] K. C. B. New, J. M. Centrella and J. E. Tohline, Phys. Rev. D, **62**, 064019 (2000).

[36] K. Nomoto, Astrophys. J., **253**, 798 (1982).

[37] K. Nomoto, in *Proc. 13th Texas Symposium on Relativistic Astrophysics*, ed. M. Ulmer (Singapore: World Scientific 1987)

[38] K. Nomoto and Y. Kondo, Astrophys. J. **367**, L19 (1991).

[39] S. Ogata, H. Iyetomi and S. Ichimaru, Astrophys. J., **372**, 259 (1991).

[40] B. K. Pickett, R. H. Durisen and R. H. Davis, Astrophys. J., **458**, 714 (1996).

[41] M. Rampp, E. Müller and M. Ruffert, Astro. & Astrophys., **332**, 969 (1998).

[42] M. Saijo, M. Shibata, T. W. Baumgarte and S. L. Shapiro, Astrophys. J., **548**, 919 (2001).

[43] E. E. Salpeter, Astrophys. J., **134**, 669 (1961).

[44] E. E. Salpeter and H. M. Van Horn, Astrophys. J., **155**, 183 (1969).

[45] R. F. Sawyer, Phy. Rev. D, **39**, 3804 (1989).

[46] S. L. Shapiro S and A. P. Lightman, Astrophys. J., **207**, 263 (1976).

[47] M. Shibata, T. W. Baumgarte and S. L. Shapiro, Astrophys. J., **542**, 453 (2000).

[48] S. Smith and J. M. Centrella, in *Approaches to Numerical Relativity*, edited by R. d'Inverno (Cambridge University Press, New York 1992).

[49] S. Smith, J. L. Houser and J. M. Centrella, Astrophys. J., **458**, 236 (1996).

[50] N. Stergioulas and J. L. Friedman, Astrophys. J., **492**, 301 (1998).

[51] K. Strobel, C. Schaab and M. K. Wiigel, Astro. & Astrophys., **350**, 497 (1999).

[52] J.-L. Tassoul, *Theory of Rotating Stars* (Princeton Univ. Press 1978).

[53] K. S. Thorne, in *Black Holes and Relativistic Stars*, ed. R. M. Wald (The University of Chicago Press 1998).

[54] F. S. Timmes and S. E. Woosley, Astrophys. J., **396**, 649 (1992).

[55] J. E. Tohline, Astrophys. J., **285**, 721 (1984).

[56] J. E. Tohline, R. H. Durisen and M. McCollough, Astrophys. J., **298**, 220, 1985.

[57] H. A. Williams and J. E. Tohline, Astrophys. J., **334**, 449, 1988.

[58] T. Zwerger and E. Müller, Astro. & Astrophys., **320**, 209 (1997).

Chapter 3

Dynamical Instability of New-born Neutron Stars as Sources of Gravitational Radiation

Accepted for publication by *Physical Review D.*

Abstract

The dynamical instability of new-born neutron stars is studied by evolving the linearized hydrodynamical equations. The neutron stars considered in this chapter are those produced by the accretion induced collapse of rigidly rotating white dwarfs. A dynamical bar-mode ($m = 2$) instability is observed when the ratio of rotational kinetic energy to gravitational potential energy β of the neutron star is greater than the critical value $\beta_d \approx 0.25$. This bar-mode instability leads to the emission of gravitational radiation that could be detected by gravitational wave detectors. However, these sources are unlikely to be detected by LIGO II interferometers if the event rate is less than 10^{-6} per year per galaxy. Nevertheless, if a significant fraction of the pre-supernova cores are rapidly rotating, there would be a substantial number of neutron stars produced by the core collapse undergoing bar-mode instability. This would greatly increase the chance of detecting the gravitational radiation.

3.1 Introduction

Neutron stars are believed to form from the core collapse of massive stars and the accretion induced collapse of massive white dwarfs. If the stellar core or white dwarf is rotating, conservation of angular momentum implies that the resulting neutron star must rotate very rapidly. It has been suggested [1]

that such a rapidly rotating star may develop a non-axisymmetric dynamical instability, emitting a substantial amount of gravitational radiation which might be detectable by gravitational wave observatories, such as LIGO, VIRGO, GEO and TAMA.

Rotational instabilities arise from non-axisymmetric perturbations having angular dependence $e^{im\varphi}$, where φ is the azimuthal angle. The $m = 2$ mode is called the bar mode, which is usually the strongest mode for stars undergoing instabilities. There are two types of instabilities. A *dynamical* instability is driven by hydrodynamics and gravity, and it develops on a dynamical timescale, e.g., the timescale for a sound wave to travel across the star. A *secular* instability, on the other hand, is driven by viscosity or gravitational radiation reaction, and its growth time is determined by the relevant dissipative timescale. These secular timescales are usually much longer than the dynamical timescale of the system.

In this chapter, we focus on the dynamical instabilities resulting from the new-born neutron stars formed from accretion induced collapse (AIC) of white dwarfs. These instabilities occur only for rapidly rotating stars. A useful parameter to characterize the rotation of a star is $\beta = T/|W|$, where T and W are the rotational kinetic energy and gravitational potential energy, respectively. It is well known that there is a critical value β_d so that a star will be dynamically unstable if its $\beta > \beta_d$. For a uniform density and rigidly rotating star, the Maclaurin spheroid, the critical value is determined to be $\beta_d \approx 0.27$ [2]. Numerous numerical simulations using Newtonian gravity show that β_d remains roughly the same for differentially rotating polytropes having the same specific angular momentum distribution as the Maclaurin spheroids [3, 4, 5, 6, 7, 8, 9, 10, 11]. However, β_d can take values between 0.14 and 0.27 for other angular momentum distributions [12, 9, 13] (the lower limit $\beta_d = 0.14$ is observed only for a star having a toroidal density distribution, i.e., the maximum density occurs off center [13]). Numerical simulations using full general relativity and post-Newtonian approximations suggest that relativistic corrections to Newtonian gravity cause β_d to decrease slightly [14, 15, 16].

Most of the stability analyses to date have been carried out by assuming that the star rotates with an *ad hoc* rotation law or using simplified equations of state. The results of these analyses might not be applicable to the new-born neutron stars resulting from AIC. Recently, Fryer, Holz and Hughes [17] carried out an AIC simulation using a realistic rotation law and a realistic equation of state. Their pre-collapse white dwarf has an angular momentum $J = 10^{49}$ g cm^2 s^{-1}. After the collapse, the neutron star has β less than 0.06, which is too small for the star to be dynamically unstable. However, they point out that if the pre-collapse white dwarf spins faster, the resulting

neutron star could have high enough β to trigger a dynamical instability. They also point out that a pre-collapse white dwarf could easily be spun up to rapid rotation by accretion. The spin of an accreting white dwarf before collapse depends on its initial mass, its magnetic field strength, its accretion rate, etc. [18].

In Chapter 2, we construct equilibrium models of new-born neutron stars resulting from AIC based on conservation of specific angular momentum. We show that if the pre-collapse white dwarfs are rapidly rotating, the resulting neutron stars could have β as large as 0.26, which is slightly smaller than the critical value β_d for Maclaurin spheroids. However, the specific angular momentum distributions of those neutron stars are very different from that of Maclaurin spheroids. So there is no reason to believe that the traditional value $\beta_d = 0.27$ can be applied to those models.

The purpose of this chapter is first to determine the critical value β_d for the new-born neutron stars resulting from AIC, and then estimate the signal-to-noise ratio and detectability of the gravitational waves emitted as a result of the instability. We do not intend to provide an accurate number for the signal-to-noise ratio, which requires a detailed nonlinear evolution of the dynamical instability. Instead, we use Newtonian gravitation theory to compute the structure of new-born neutron stars. Then we evolve the linearized Newtonian hydrodynamical equations to study the star's stability and determine the critical value β_d. Relativistic effects are expected to give a correction of order $(v/c)^2$, which is about 8% for the rapidly rotating neutron stars studied in this chapter. Here v is a typical sound speed inside the star and c is the speed of light.

This chapter is organized as follows. In Sec. 3.2, we apply the method described in Chapter 2 to construct a number of equilibrium neutron star models with different values of β. In Sec. 3.3, we study the stability of these models by adding small density and velocity perturbations to the equilibrium models. Then we evolve the perturbations by solving linearized hydrodynamical equations proposed by Toman et al. [28]. From the simulations, we can find out whether the star is stable and determine the critical value β_d. In Sec. 3.4, we estimate the strength and signal-to-noise ratio of the gravitational waves emitted by this instability. In Sec. 3.5, we estimate the effects of a magnetic field on the stability results. Finally, we summarize and discuss our results in Sec. 3.6.

3.2 Equilibrium models

In this section, we describe briefly how we construct new-born neutron star models from the pre-collapse white dwarfs. A more detailed description is given in Chapter 2.

3.2.1 Pre-collapse white dwarf models

We consider two types of pre-collapse white dwarfs: those made of carbon-oxygen (C-O) and those made of oxygen-neon-magnesium (O-Ne-Mg). The collapse of a massive C-O white dwarf is triggered by the explosive carbon burning near the center of the star [19, 20]. The central density of the pre-collapse C-O white dwarf must be in the range 6×10^9 g cm$^{-3} \lesssim \rho_c \lesssim 10^{10}$ g cm^{-3} in order for the collapse to result in a neutron star, rather than exploding as a Type Ia supernova [21]. The collapse of a massive O-Ne-Mg white dwarf, on the other hand, is triggered by electron captures by ^{24}Mg and ^{20}Ne when the central density reaches 4×10^9 g cm^{-3} [19, 20].

We construct three sequences of pre-collapse white dwarfs, with models in each sequence having different amounts of rotation. Sequences I and II correspond to C-O white dwarfs with central densities $\rho_c = 10^{10}$ g cm^{-3} and $\rho_c = 6 \times 10^9$ g cm^{-3} respectively. Sequence III is for O-Ne-Mg white dwarfs with $\rho_c = 4 \times 10^9$ g cm^{-3}. All white dwarfs are assumed to rotate rigidly, because the timescale for a magnetic field to suppress differential rotation is much shorter than the accretion timescale (see Sec. 3.6).

The pre-collapse white dwarfs constructed in this section are described by the equation of state (EOS) of a zero-temperature ideal degenerate electron gas with electrostatic corrections derived by Salpeter [22]. At high density, the pressure is dominated by the ideal degenerate Fermi gas with electron fraction $Z/A = 0.5$ that is suitable for both C-O and O-Ne-Mg white dwarfs. Electrostatic corrections, which depend on the white dwarf composition through the atomic number Z, contribute only a few percent to the EOS for the high density white dwarfs considered here.

Equilibrium models are computed by Hachisu's self-consistent field method [23], which is an iteration scheme based on the integrated Euler equation for hydrostatic equilibrium:

$$h + \Phi - \frac{\varpi^2}{2}\Omega^2 = C \ , \tag{3.1}$$

where Ω is the rotational angular frequency of the star; C is a constant; ϖ is the radius from the rotation axis; h is the specific enthalpy, which is related to the density ρ and pressure P by

$$h = \int_0^P \frac{dP}{\rho} \ . \tag{3.2}$$

The gravitational potential Φ satisfies the Poisson equation

$$\nabla^2 \Phi = 4\pi G \rho \ , \tag{3.3}$$

Table 3.1: Properties of pre-collapse white dwarfs. Here Ω is the rotational angular frequency; Ω_m is the maximum rotational angular frequency of the white dwarf in the sequence without mass shedding; R_e, R_p, M, J and β are, respectively, the equatorial radius, polar radius, mass, angular momentum and the ratio of rotational kinetic to gravitational potential energies.

Sequence I: C-O white dwarfs with $\rho_c = 10^{10}$ g cm^{-3}

Ω/Ω_m	R_e (km)	R_e/R_p	$M/M_\odot$	J (g cm^2 s^{-1})	β
0.20	1310	1.01	1.40	5.14×10^{48}	5.36×10^{-4}
0.65	1400	1.09	1.42	1.81×10^{49}	6.08×10^{-3}
0.84	1500	1.19	1.44	2.43×10^{49}	1.03×10^{-2}
0.93	1600	1.27	1.46	2.80×10^{49}	1.30×10^{-2}
1.00	1895	1.52	1.47	3.12×10^{49}	1.55×10^{-2}

Sequence II: C-O white dwarfs with $\rho_c = 6 \times 10^{10}$ g cm^{-3}

Ω/Ω_m	R_e (km)	R_e/R_p	$M/M_\odot$	J (g cm^2 s^{-1})	β
0.23	1517	1.01	1.39	3.31×10^{48}	7.73×10^{-4}
0.64	1610	1.09	1.42	1.95×10^{49}	6.11×10^{-3}
0.84	1740	1.19	1.44	2.75×10^{49}	1.12×10^{-2}
0.93	1847	1.28	1.45	3.13×10^{49}	1.39×10^{-2}
1.00	2189	1.52	1.46	3.51×10^{49}	1.66×10^{-2}

Sequence III: O-Ne-Mg white dwarfs with $\rho_c = 4 \times 10^{10}$ g cm^{-3}

Ω/Ω_m	R_e (km)	R_e/R_p	$M/M_\odot$	J (g cm^2 s^{-1})	β
0.23	1692	1.01	1.38	7.01×10^{48}	7.90×10^{-4}
0.62	1791	1.09	1.40	2.05×10^{49}	6.23×10^{-3}
0.86	1956	1.20	1.42	3.03×10^{49}	1.23×10^{-2}
0.96	2156	1.34	1.44	3.59×10^{49}	1.62×10^{-2}
1.00	2441	1.52	1.45	3.80×10^{49}	1.77×10^{-2}

where G is the gravitational constant. The self-consistent field method determines the structure of the star for fixed values of two adjustable parameters. In Ref. [23], the maximum density and axis ratio (the ratio of polar to equatorial radii) are the chosen parameters. However, it is more convenient to choose the central density ρ_c and equatorial radius R_e as the two parameters for the models studied here.

The accuracy of the equilibrium models can be measured by the quantity

$$\epsilon = \left| \frac{2T + W + 3\Pi}{W} \right| , \tag{3.4}$$

which should be equal to zero according to the Virial theorem (see e.g. [24]). Here T is the rotational kinetic energy; W is the gravitational potential energy and $\Pi = \int P d^3x$. The values of ϵ are of order 10^{-7} for all the pre-collapse white dwarf models calculated in this section. Table 3.1 shows some

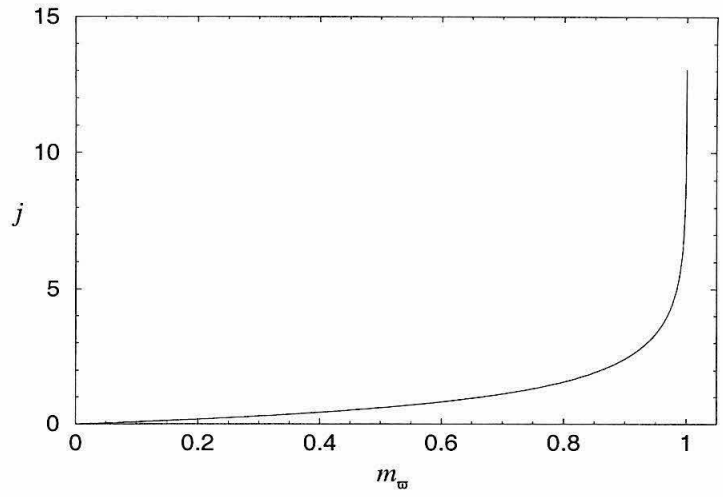

Figure 3.1: The normalized specific angular momentum j as a function of the cylindrical mass fraction m_ϖ for the white dwarf model in sequence III with $\Omega/\Omega_m = 0.964$.

properties of several pre-collapse white dwarfs in the three sequences. Each sequence terminates when the rotational angular frequency Ω of the white dwarf reaches a critical value Ω_m so that the mass shedding occurs on the equatorial surface of the star. The values of Ω_m are 5.37 rad s^{-1} for Sequence I, 4.32 rad s^{-1} for Sequence II, and 3.65 rad s^{-1} for Sequence III.

Figure 3.1 shows the normalized specific angular momentum

$$j = \frac{M}{J}\Omega\varpi^2 \tag{3.5}$$

as a function of the cylindrical mass fraction

$$m_\varpi = \frac{2\pi}{M}\int_0^\varpi d\varpi'\,\varpi'\int_{-\infty}^{\infty} dz'\,\rho(\varpi', z') \tag{3.6}$$

for a typical pre-collapse model. Here M and J are the total mass and angular momentum of the star, respectively. The specific angular momentum defined in Eq. (3.5) is normalized so that $\int_0^1 j(m_\varpi)\,dm_\varpi = 1$. The curves for other models are similar. The spike near $m_\varpi = 1$ is due to the high degree of central condensation of the white dwarf density (see Section 2.2.3).

3.2.2 Collapsed objects

The gravitational collapse of a massive white dwarf is halted when the core density reaches nuclear density. The core bounces back and settles down into hydrodynamical equilibrium in a few millisec-

onds. A hot ($T \gtrsim 20$ MeV) and lepton-rich *protoneutron star* is formed. After about 20 s, neutrinos carry away most of the energy and the star cools down to a cold neutron star. The hot protoneutron stars are less compact and have β smaller than 0.14 (see Chapter 2). They are thus expected to be dynamically stable. Hence in this chapter, we focus on the stability of the cold neutron stars shortly after the cooling.

We assume that (1) the neutron stars are axisymmetric and are in rotational equilibrium with no meridional circulation; (2) viscosity can be neglected; (3) no material is ejected during the collapse. Under these assumptions, it is easy to prove that the specific angular momentum j of the collapsed star as a function of cylindrical mass fraction m_ϖ is the same as the pre-collapse white dwarf. Hence the structure of the new-born neutron stars can be constructed by computing models with the same masses, angular momenta and $j(m_\varpi)$-distributions as the pre-collapse white dwarfs.

We adopt the Bethe-Johnson EOS [25] for densities above 10^{14} g cm^{-3}, and BBP EOS [26] for densities in the range $10^{11} - 10^{14}$ g cm^{-3}. The EOS for densities below 10^{11} g cm^{-3} is joined by that of the pre-collapse white dwarfs.

We construct the equilibrium models by the numerical method proposed by Smith and Centrella [27], which is a modified version of Hachisu's self-consistent field method so that $j(m_\varpi)$ can be specified. The iteration scheme is based on the integrated Euler equation (3.1) written in the form

$$h = C - \Phi + \left(\frac{J}{M}\right)^2 \int_0^\varpi d\varpi' \, \frac{j^2(m_{\varpi'})}{\varpi'^3} \ , \tag{3.7}$$

where J and M are the total angular momentum and mass of the star, respectively. As before, two parameters have to be fixed in the iteration procedure. We choose to fix the central density ρ_c and equatorial radius R_e. Since the correct ρ_c and R_e are not known beforehand, we have to vary these two quantities until the equilibrium model has the same J and M as the pre-collapse white dwarf.

The standard iteration algorithm described in Refs. [23] and [27] fails to converge when the star becomes very flattened. This problem is fixed by a modified scheme proposed by Pickett, Durisen and Davis [9], in which only a fraction of the revised density (or enthalpy) ρ_{i+1}, i.e. $\rho'_{i+1} = (1-\zeta)\rho_{i+1} + \zeta\rho_i$, is used for the next iteration. Here $\zeta < 1$ is a parameter controlling the change of density. A value of $\zeta > 0.95$ has to be used for very flattened configurations, and it takes 100–200 iterations for the density and enthalpy distributions to converge.

Chapter 2 mentions another numerical difficulty which has to do with the spike of the $j(m_\varpi)$ curve near $m_\varpi = 1$. We have to truncate a small portion of the $j(m_\varpi)$ curve in order to make the iteration converge. We also demonstrate that this truncation does not affect the inner structure of

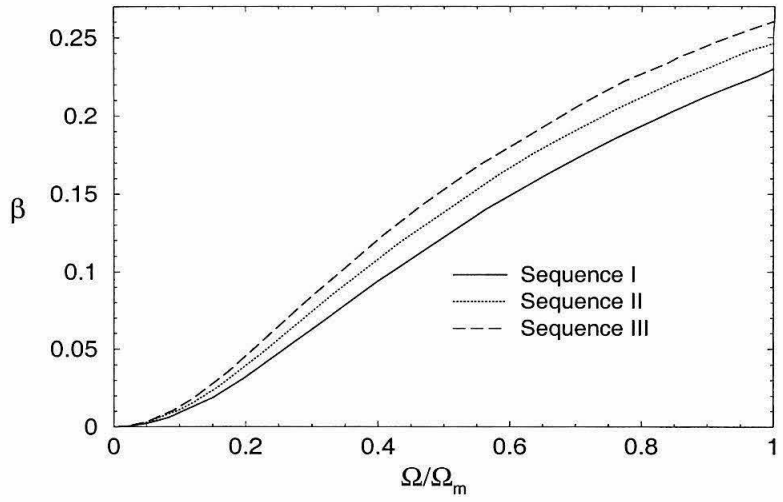

Figure 3.2: The values of β of the resulting neutron stars as a function of Ω/Ω_m of the pre-collapse white dwarfs.

the star. It turns out that, for reasons still to be understood, the numerical instability associated with the $j(m_\varpi)$ curve only occurs for the most rapidly rotating models (i.e., those models where the pre-collapse white dwarfs have $\Omega/\Omega_m = 1$). Hence, the truncation is not necessary for all the other cases.

As in the case of pre-collapse white dwarfs, we measure the accuracy of the equilibrium models by the quantity ϵ defined in Eq. (3.4). The models computed in this subsection have ϵ ranges from about 10^{-6} (for slowly rotating stars) to 10^{-4} (for rapidly rotating stars). We construct a number of neutron star models resulting from the collapse of the three sequences of pre-collapse white dwarfs in the previous subsection. The ratio of rotational kinetic energy to gravitational potential energy, β, of the neutron stars is plotted in Fig. 3.2 as a function of Ω/Ω_m of the pre-collapse white dwarf. The values of β for all the neutron star models are smaller than 0.27, the critical value of β for the dynamical instability of rigidly rotating Maclaurin spheroids.

The structure of the neutron stars with $\beta \gtrsim 0.1$ are all similar: they contain a high-density central core of size about 20 km, surrounded by a low-density torus-like envelope. The size of the envelope depends on the amount of rotation of the star, which can be measured by β. The size ranges from 100 km (for $\beta \sim 0.1$) to over 500 km (for $\beta \gtrsim 0.2$). Figure 3.3 shows the density contours of a typical model. This model corresponds to the collapse of an O-Ne-Mg white dwarf with $\Omega/\Omega_m = 0.964$. The resulting neutron star has $\beta = 0.255$. The envelope extends to about 1530 km in this case. As a comparison, the equatorial radius of the pre-collapse white dwarf is 2156 km.

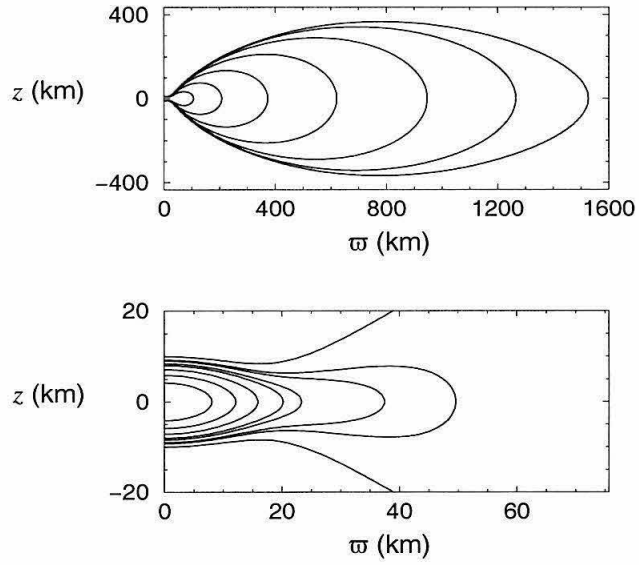

Figure 3.3: Meridional density contours of the neutron star resulting from the AIC of a rigidly rotating O-Ne-Mg white dwarf with $\Omega/\Omega_m = 0.964$. This neutron star has $\beta = 0.255$. The contours in the upper graph denote, from inward to outward, $\rho/\rho_c = 10^{-4}$, 10^{-5}, 10^{-6}, 10^{-7}, 10^{-8}, 10^{-9} and 0. The contours in the lower graph denote, from inward to outward, $\rho/\rho_c = 0.8$, 0.6, 0.4, 0.2, 0.1, 10^{-2}, 10^{-3} and 10^{-4}. The central density of the star is $\rho_c = 3.3 \times 10^{14}$ g cm^{-3}.

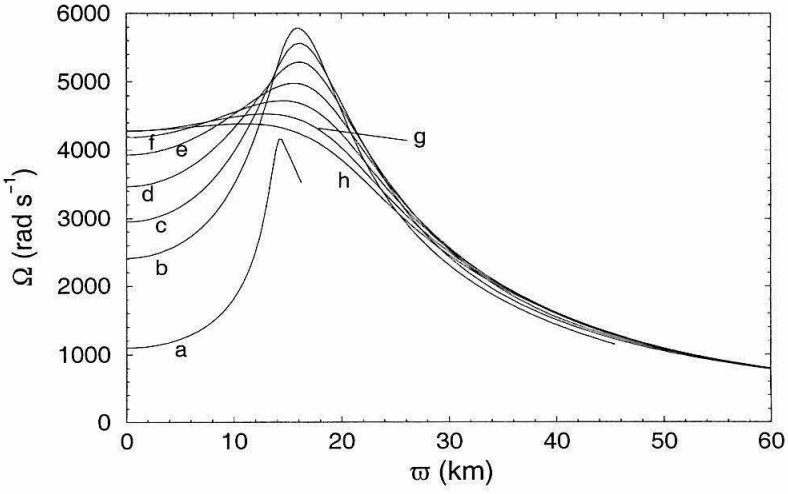

Figure 3.4: The distribution of rotational angular velocity Ω as a function of ϖ for $\varpi < 60$ km. These are models for sequence III with β's of the resulting neutron stars equal to (a) 0.0106, (b) 0.0555, (c) 0.0860, (d) 0.124, (e) 0.169, (f) 0.208, (g) 0.238 and (h) 0.261. The equatorial radii of the neutron stars in cases (a) and (b) are smaller than 60 km, and their frequency curves terminate at their equatorial radii.

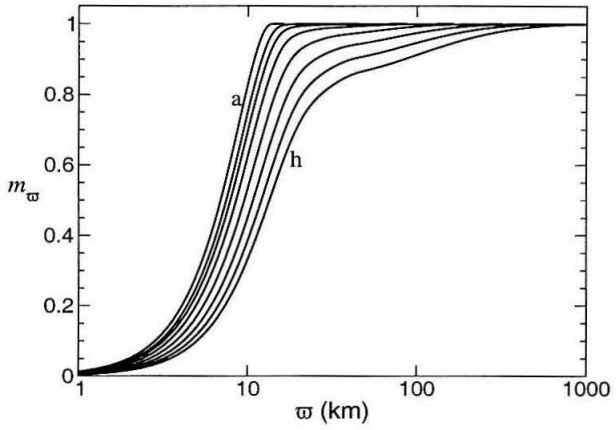

Figure 3.5: The cylindrical mass fraction m_ϖ as a function of ϖ for neutron star models in Fig. 3.4. The curves and their corresponding models are identified by the degree of central condensation: the higher the degree of central condensation, the lower the value of β.

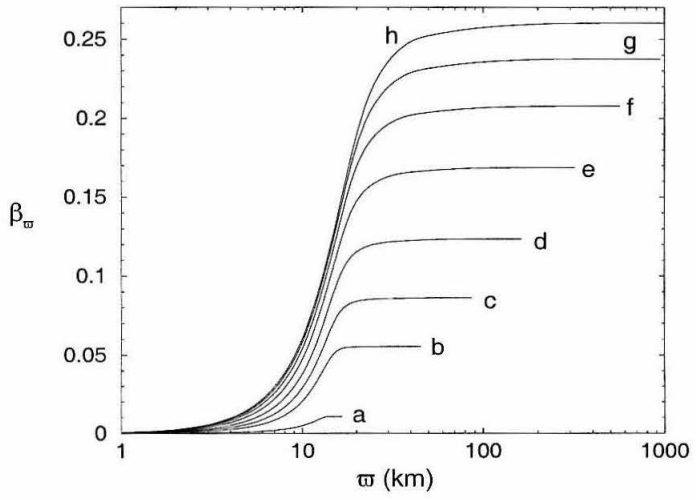

Figure 3.6: The value of β_ϖ as a function of ϖ for the neutron star models in Fig. 3.4. The curves for models (a)–(g) terminate at the equatorial radii of the stars.

Figure 3.4 shows the rotational angular velocity Ω as a function of radius ϖ for neutron star models corresponding to the collapse of sequence III white dwarfs. The cases for sequences I and II are similar. We see that stars with small β show strong differential rotation. However, the rotation in the core region ($\varpi \lesssim 20$ km) becomes more and more rigidly rotating as β increases. The most rapidly rotating case ($\beta = 0.261$) has $\Omega \approx 4400$ rad s^{-1} in the core. This corresponds to a rotation period of 1.4 ms, slightly less than the period of the fastest observed millisecond pulsar (1.56 ms). Further analysis reveals that the rotation curve in the envelope region roughly follows the Kepler law $\Omega \propto \varpi^{-3/2}$.

Figure 3.5 shows the cylindrical mass fraction m_ϖ as a function of ϖ for the same models as in Fig. 3.4. As expected, the degree of central concentration decreases with increasing β. However, more than 80% of the mass is still concentrated inside a radius $\varpi = 30$ km, even for the most rapidly rotating case. The collapsed object can be regarded as a rotating neutron star surrounded by an accretion torus.

Numerous numerical studies demonstrate that the quantity β is an important parameter for the dynamical stability of a rotating star. It is then useful to define a function β_ϖ as

$$\beta_\varpi = \frac{\int_0^\varpi d\varpi'\, \varpi' \int_{-\infty}^{\infty} dz'\, [\varpi'\Omega(\omega')]^2 \rho(\varpi', z')}{|\int_0^\varpi d\varpi'\, \varpi' \int_{-\infty}^{\infty} dz'\, \rho(\varpi', z')\Phi(\varpi', z')|}\ , \tag{3.8}$$

which is a measure of β for the material inside a cylinder of radius ϖ from the rotation axis. Figure 3.6 plots β_ϖ as a function of ϖ for the same neutron star models as in Fig. 3.4. We see that the curves level off when $\varpi \gtrsim 20 - 100$ km for all rapidly rotating models, suggesting that the material outside 100 km is probably unimportant for dynamical stability. It should also be noticed that the major contribution to β is from the region 10 km $\lesssim \varpi \lesssim 50$ km. Hence we expect that the material in this region plays an important role on the dynamical stability of the star.

3.3 Stability of the collapsed objects

In this section, we study the dynamical stabilities of the neutron star models computed in Sec. 3.2.2 using the technique of the linear stability analysis developed by Toman et al. [28]. This technique is briefly reviewed in Sec. 3.3.1. We then report the stability results in Sec. 3.3.2.

3.3.1 Linear stability analysis

The motion of fluid inside the star is described by the hydrodynamical equations:

$$\partial_t \rho + \nabla_a(\rho v^a) = 0 \ , \tag{3.9}$$

$$\partial_t v^a + v^b \nabla_b v^a = -\frac{\nabla^a P}{\rho} - \nabla^a \Phi \ , \tag{3.10}$$

$$\nabla_a \nabla^a \Phi = 4\pi G \rho \ , \tag{3.11}$$

where the summation convention is assumed, and ∇_a denotes the covariant derivative compatible with 3-D flat-space metric. To study the stability, we perturb the density ρ and velocity v^a away from their equilibrium values by small quantities:

$$\rho(x^b, t) = \rho_0(x^b) + \delta\rho(x^b, t) \ , \tag{3.12}$$

$$v^a(x^b, t) = \varpi\Omega(\varpi) e^a_{\hat{\varphi}} + \delta v^a(x^b, t) \ , \tag{3.13}$$

where $e^a_{\hat{\varphi}}$ is the unit vector along the azimuthal direction. The Lagrangian pressure perturbation ΔP is related to the Lagrangian density perturbation $\Delta\rho$ by

$$\Delta P = \gamma_p \frac{P}{\rho} \Delta\rho \ , \tag{3.14}$$

where for simplicity, the subscript "0" is suppressed, and hereafter in this section, ρ and P denote the equilibrium density and pressure, respectively. The quantity

$$\gamma_p = \left(\frac{d \log P}{d \log \rho} \right)_p \tag{3.15}$$

is the adiabatic index for pulsation. The relation between the Eulerian perturbations δP and $\delta\rho$ can be easily deduced from the transformation between the Lagrangian and Eulerian perturbations. The result is

$$\delta P = \gamma_p \frac{P}{\rho} \delta\rho + \left(\frac{\gamma_p}{\gamma_{\rm eq}} - 1 \right) \xi^a \nabla_a P \ , \tag{3.16}$$

where

$$\gamma_{\rm eq} = \left(\frac{d \log P}{d \log \rho} \right)_{\rm eq} \tag{3.17}$$

is the adiabatic index computed from the equilibrium EOS. The Lagrangian displacement ξ^a satisfies the equation

$$\partial_t \xi^a + v^b \nabla_b \xi^a - \xi^b \nabla_b v^a = \delta v^a \ . \tag{3.18}$$

The Eulerian change of the gravitational potential $\delta\Phi$ satisfies the Poisson equation

$$\nabla_a \nabla^a \delta\Phi = 4\pi G \delta\rho \ . \tag{3.19}$$

We find it useful to introduce a quantity $\delta h \equiv \delta P/\rho$, which is related to $\delta\rho$ by

$$\delta h = \gamma_p \frac{P}{\rho^2}\delta\rho + \left(\frac{\gamma_p}{\gamma_{\rm eq}} - 1\right)\xi^a \nabla_a h \ . \tag{3.20}$$

In the region where $\gamma_p = \gamma_{\rm eq}$, δh is the Eulerian change of the enthalpy.

If the system is unstable, the perturbed quantities will grow in time. Instead of solving the fully nonlinear equations (3.9)–(3.11), however, Toman et al. [28] develop a more efficient approach: expand Eqs. (3.9)–(3.11) to linear order of the perturbations and evolve the linearized equations.

Consider the angular Fourier decomposition of any perturbed quantity δq:

$$\delta q(x^b, t) = \sum_{m=-\infty}^{\infty} \delta\tilde{q}_m(\varpi, z, t) e^{im\varphi} \ . \tag{3.21}$$

It can be easily proved that each m-mode decouples in the linearized hydrodynamical equations because of the axisymmetry of the equilibrium configuration. In addition, the fact that the equilibrium configuration is symmetric under reflection about the equatorial plane ($z \to -z$) implies the modes with even and odd parity under the transformation $z \to -z$ also decouple. Hence each m-mode with a definite parity can be evolved separately and the 3+1 simulation is reduced to a 2+1 simulation, which saves a lot of computation time. Hereafter, all perturbed quantities will be assumed to have angular dependence $e^{im\varphi}$.

In Ref. [28], Toman et al. choose to evolve the variables $\delta\rho$ and δv^a. However, we find it more convenient and numerically stable in our case to evolve the variables δh and $\delta p^a = \rho\delta v^a$. The reason being that the simulations are performed on a discrete grid, and it is preferable to use variables that change smoothly to ensure accuracy. However, the background density ρ decreases abruptly outside the core region, and the perturbation $\delta\rho$ is expected to behave similarly. On the other hand, h, and presumably δh, change much more smoothly even near the boundary of the star. In the case where $\gamma_p \neq \gamma_{\rm eq}$, we also need to evolve the scalar function $\eta = \xi^b \nabla_b h$. In terms of the new variables, the

linearized equations become

$$\begin{aligned}
\partial_t \delta h &= -im\Omega\delta h - \gamma_p \frac{P}{\rho^2}\nabla_a \delta p^a \\
&\quad + \left(\frac{\gamma_p}{\gamma_{\rm eq}} - 1\right)\frac{\delta p^a}{\rho}\nabla_a h \ , \qquad (3.22)\\
\partial_t \delta p^a &= -\delta p^b \nabla_b v^a - v^b \nabla_b \delta p^a - \rho\nabla^a \delta h - \rho\nabla^a \delta\Phi \\
&\quad - \left(\frac{\gamma_p}{\gamma_{\rm eq}} - 1\right)\frac{\rho^2}{\gamma_p P}(\delta h + \eta)\nabla^a h \ , \qquad (3.23)\\
\partial_t \eta &= -im\Omega\eta + \frac{\delta p^a}{\rho}\nabla_a h \ , \qquad (3.24)\\
\nabla_a\nabla^a\delta\Phi &= \frac{4\pi G\rho^2}{\gamma_p P}\left[\delta h - \left(\frac{\gamma_p}{\gamma_{\rm eq}} - 1\right)\eta\right] \ . \qquad (3.25)
\end{aligned}$$

It follows from Eqs. (3.22)–(3.25) that if $(\delta h, \delta p^a)$ is a solution for an m-mode, the complex conjugate $(\delta h^*, \delta p^{a*})$ is a solution for the -m-mode. We can then define the physical "enthalpy" perturbation $\delta\tilde{h} = \delta h + \delta h^*$, and similarly for the physical density $\delta\tilde{\rho}$ and velocity $\delta\tilde{v}^a$ perturbations of an m-mode.

We use a uniform cylindrical grid to perform the simulations. We have checked that the code is able to reproduce the results in Ref. [28]. However, unlike the case in Ref. [28], the collapsed objects studied here have a large envelope extending beyond 1000 km when the stars under consideration are rapidly rotating. This numerical difficulty can be circumvented by a suitable truncation scheme.

As pointed out in Sec. 3.2.2, we expect the outer envelope will not influence the dynamical stability in any significant way. Hence it is necessary to evolve the perturbations only in the dynamically interesting region. This is done by introducing a radius R_m and a minimum density $\rho_{\rm min} \equiv \rho(R_m, 0)$. The perturbations are set to zero wherever the equilibrium density $\rho(\varpi, z) < \rho_{\rm min}$. If R_m is sufficiently large, increasing its value will not change the evolution result. We find that a value of $R_m \approx 200$ km is needed to ensure that the results converge, and we use a cylindrical grid with 400×400 grid points to achieve a resolution of 0.5 km.

In general, the two adiabatic indices γ_p and $\gamma_{\rm eq}$ are not equal. They coincide only if the pulsation timescale is much longer than all the reaction timescales for the different species of particles in the fluid to achieve equilibrium. This is the case for densities below neutron drip ($\rho \lesssim 4 \times 10^{11}$ g cm^{-3}) and above about 10^{13} g cm^{-3}. However, in the density range 4×10^{11} g cm$^{-3} \lesssim \rho \lesssim 10^{13}$ g cm^{-3}, the matter is a mixture of electrons, neutrons and nuclei in equilibrium. Some of the reactions required to achieve equilibrium involve weak interactions, which have timescales much longer than the pulsation timescale. Hence equilibrium is not achieved during pulsation, and $\gamma_p \neq \gamma_{\rm eq}$ in that density range [29, 30]. Most people studying neutron star pulsations neglect the difference of γ_p and $\gamma_{\rm eq}$ and use $\gamma_{\rm eq}$ in their calculations. It has been demonstrated (see, e.g. [32]) that this treatment has

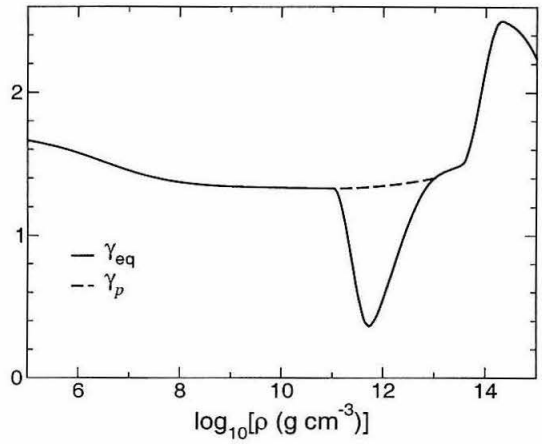

Figure 3.7: The values of $\gamma_{\rm eq}$ (solid line) and γ_p (dashed line) as a function of $\log_{10}\rho$. The two curves coincide when $\rho < \rho_d$ and $\rho > \rho_e$.

no significant effect on the final result, because the matter in that density range occupies only a tiny fraction of neutron star. However, it may have an important effect on the stability of the new-born neutron stars studied here. The reason is that the dynamically important region, as pointed out in Sec. 3.2.2, is 10 km $\lesssim \varpi \lesssim$ 50 km. This region contains a significant amount of matter in that density range (see Fig. 3.3). Our numerical simulations indicate that this is indeed the case. The critical value β_d for the dynamical instability drops from about 0.25 to 0.23 if $\gamma_{\rm eq}$ is used for the adiabatic index of pulsation.

The appropriate γ_p remains roughly constant from the density of neutron drip $\rho_d = 4 \times 10^{11}$ g cm^{-3} to the density above which $\gamma_{\rm eq} = \gamma_p$ around $\rho_e = 10^{13}$ g cm^{-3} [29, 30]. To provide a reasonable value of γ_p which mimics the curve in Refs. [29, 30] and which is compatible with the EOS used here, we take γ_p in the density range $\rho_d < \rho < \rho_e$ to be (also see Fig. 3.7)

$$\gamma_p(\rho) = \gamma_{\rm eq}(\rho_d) + [\gamma_{\rm eq}(\rho_e) - \gamma_{\rm eq}(\rho_d)]\,\frac{\log^2(\rho/\rho_d)}{\log^2(\rho_e/\rho_d)}\ . \tag{3.26}$$

Under some circumstances it is possible to have a region of the star where the mode is stationary in the fluid's co-rotating frame. In this case, we should use $\gamma_{\rm eq}$ for the adiabatic index of pulsation in the region where $|\omega'| = |\omega + m\Omega| \ll 2\pi/t_r$. Here ω is the angular frequency of an m-mode that has dependence $\exp[i(\omega t + m\varphi)]$ in the inertial frame; $\omega' = \omega + m\Omega$ is the angular frequency of the mode in the fluid's co-rotating frame; and $t_r \approx 1$ s is the timescale for different species of particles

to achieve β-equilibrium in the density range $\rho_d < \rho < \rho_e$. It turns out (see the next subsection) that rapidly rotating neutron stars have an unstable bar mode ($m = 2$) with $\omega \approx -3000$ rad s^{-1}. There is indeed a radius at which $\omega' = 0$. This radius is at $\varpi = \varpi_c \approx 40$ km for stars with $\beta > 0.23$. The density on the equator of the stars is $\rho \approx 10^{12}$ g cm^{-3}, well within the questionable density range. However, the width of this "co-rotating region," which satisfies $|\omega'| < 2\pi/t_r$, is

$$\Delta\varpi = \frac{2\pi/t_r}{|\partial_\varpi \Omega(\varpi_c)|} \approx 0.1 \text{ km} .$$

The material in the region contains only 10^{-4} of total mass and angular momentum of the star. Hence this thin co-rotating layer is not expected to have a significant influence on the overall stability of the stars.

3.3.2 Results

We perform a number of simulations on neutron star models computed by the method described in Sec. 3.2.2. The simulations are terminated either when an instability is fully developed or when the simulation time reaches 60 ms, corresponding to 40 rotation periods of the material at the center of the star. We regard a star as dynamically unstable if the density perturbation shows evidence of exponential growth and increases its amplitude by at least a factor of fifteen by the end of the simulation. In our simulations, no instability is observed for neutron star models in sequences I and II. A bar-mode ($m = 2$) instability develops for sequence III models when the star's β is greater than a critical value $\beta_d \approx 0.25$. The unstable mode has even parity under reflection about the equatorial plane. This β_d is slightly less than the critical value 0.27 for the Maclaurin spheroids. It should be pointed out that all the stars in sequences I and II have β's smaller than this β_d. Hence we believe that they are stable simply because their β's are not high enough.

Some other simulations [9, 13] show that in the cases where $\beta_d < 0.27$, the instability is dominated by the $m = 1$ mode for stars with β close to β_d. However, we do not observe any sign of an unstable $m = 1$ mode in our case. We also performed simulations using $\gamma_{\rm eq}$ (the solid curve in Fig. 3.7) as the adiabatic index for pulsation instead of γ_p (the dashed curve in Fig. 3.7). We find that β_d drops to about 0.23, showing that matter in the density region $\rho_d < \rho < \rho_e$ plays an important role on the instability.

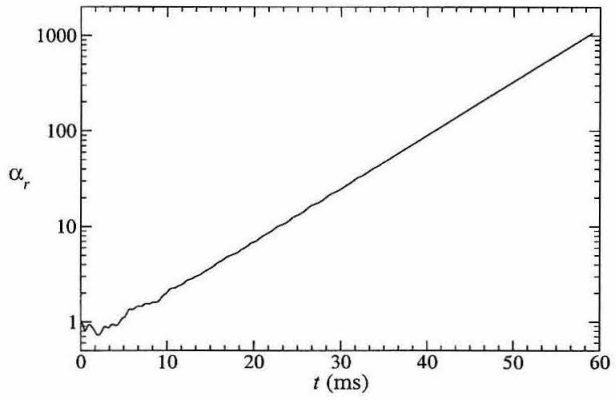

Figure 3.8: The relative amplitude α_r as a function of time. The equilibrium star has $\beta = 0.261$, the most rapidly rotating model.

To visualize the instability, we define an amplitude

$$\alpha = \left(\frac{\int |\delta\rho|^2 \, d^3x}{\int \rho^2 \, d^3x} \right)^{1/2} \tag{3.27}$$

for the density perturbation. Since we evolve the perturbations using linearized equations, it is more convenient to work with the relative amplitude α_r:

$$\alpha_r(t) = \alpha(t)/\alpha(0) \ . \tag{3.28}$$

This relative amplitude is defined so that it is equal to one at $t = 0$. Figure 3.8 shows the time evolution of α_r for the most rapidly rotating star ($\beta = 0.261$). We see that after about 10 ms, an instability develops and α_r grows exponentially. The e-folding time of the growth τ is found, by least squares fit, to be 7.8 ms.

The unstable mode can also be characterized by a complex angular frequency defined as

$$\omega_{22} = \frac{\dot{D}_{22}}{iD_{22}} \ , \tag{3.29}$$

where

$$D_{22} = \int r^2 \delta\rho Y_{22}^* \, d^3x \tag{3.30}$$

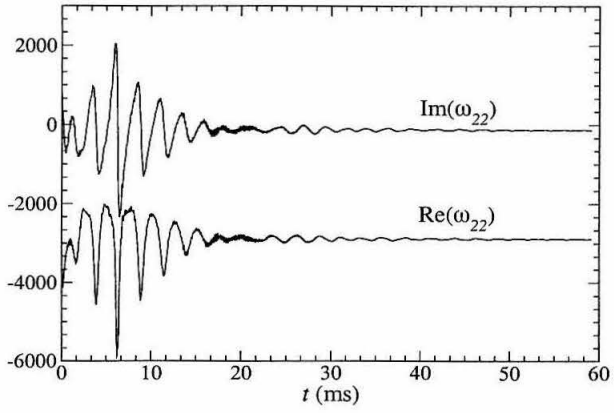

Figure 3.9: The time evolution of the angular frequency ω_{22} for the most rapidly rotating star ($\beta = 0.261$).

is the mass quadrupole moment, and the spherical harmonic function

$$Y_{22} = \frac{1}{4}\sqrt{\frac{15}{2\pi}}\,\sin^2\theta\, e^{2i\varphi}\ .$$

The time derivative of D_{22} is evaluated by the formula [31]

$$\dot{D}_{22} = \int \delta p^a \nabla_a (r^2 Y_{22}^*)\, d^3x - 2i \int \Omega r^2 \delta\rho Y_{22}^*\, d^3x\ , \tag{3.31}$$

where we have used the continuity equation (3.9) and integrated by parts.

Let ω be the complex frequency of the most unstable mode. The e-folding time is related to the imaginary part of ω by $\mathrm{Im}(\omega) = -1/\tau$. At late time, the density perturbation is dominated by the most unstable mode, which means that both $\delta\rho$ and D_{22} go approximately as $\exp(i\omega t)$. Hence $\omega_{22} \approx \omega$. Figure 3.9 plots ω_{22} as a function of time for the evolution of the most rapidly rotating star. We see that at late time, ω_{22} is approximately a constant, indicating that the perturbation is indeed dominated by the most unstable mode. The frequency of the unstable mode is then determined to be $\omega \approx (-2890 - 130i)$ rad s^{-1}. Note that the imaginary part agrees with the e-folding time determined above.

Figure 3.10 shows the magnitude of the density perturbation $|\delta\rho|$ of the unstable bar mode of the most rapidly rotating star ($\beta = 0.261$) on the equatorial plane. We see that $|\delta\rho|$ has a peak at $\varpi \approx 20$ km, which is in the transition region between the neutron star core and the tenuous outer

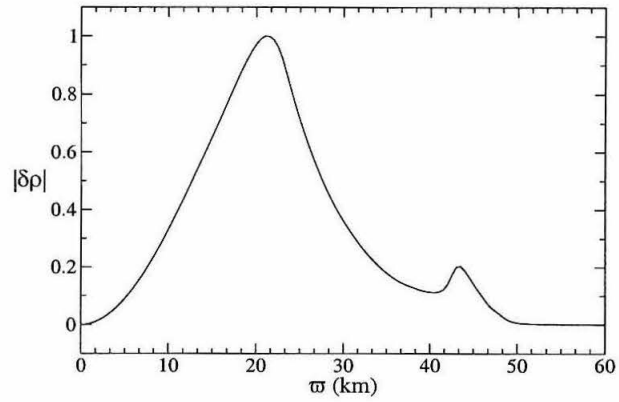

Figure 3.10: The magnitude of the density perturbation $|\delta\rho|$ of the unstable bar mode of the most rapidly rotating star ($\beta = 0.261$) on the equatorial plane. The magnitude is normalized so that the maximum value is one.

layers (see Fig. 3.3). There is a small, secondary peak at $\varpi = 44$ km, which is the co-rotation radius at which $\mathrm{Re}(\omega) + 2\Omega = 0$ for this neutron star. This secondary peak is caused by the resonant response of the fluid being driven by the mode co-rotating with it (see Section 3.7).

Figures 3.11 and 3.12 show the eigenfunctions of the physical perturbations $\delta\tilde{\rho}$ and $\delta\tilde{v}^a$ on the equatorial plane. Note that our grid extends out to 200 km from the center, but the dynamically interesting region is concentrated within 60 km from the center. Since the time dependence of the perturbations goes as $\exp[i(\omega t + m\varphi)]$, $\mathrm{Re}(\omega) < 0$ means the pattern rotates in prograde (counter-clockwise) direction. The density perturbation is bar-like in the inner region and becomes trailing spirals in the outer region. Similar structure is also observed in other numerical simulations on the bar-mode instability [9, 28, 8, 10, 11, 7, 33]. The secondary peak of $\delta\rho$ appears as two small arcs in Fig. 3.11 just inside the 0.1 contours. Figure 3.12 shows that $\delta\tilde{v}^a$ is almost parallel to the φ direction at the co-rotation radius, which is also a result of resonance (see Section 3.7). Since $\delta\tilde{v}^a$ changes abruptly near the co-rotation radius, it is very possible that shocks will develop there when the perturbations become large. This might have significant influence on the nonlinear evolution of the bar mode.

The eigenfunctions of the most unstable bar mode for the other unstable equilibrium neutron stars are similar to those displayed above. Table 3.2 summarizes the oscillation frequencies [$f = |\mathrm{Re}(\omega)|/(2\pi)$] and e-folding time τ of the unstable models we have studied. The table also shows the ratio of the rotational frequency of the pre-collapse white dwarfs to the maximum frequency Ω_m of the white dwarf in the sequence. We find that the oscillation frequencies are almost the same

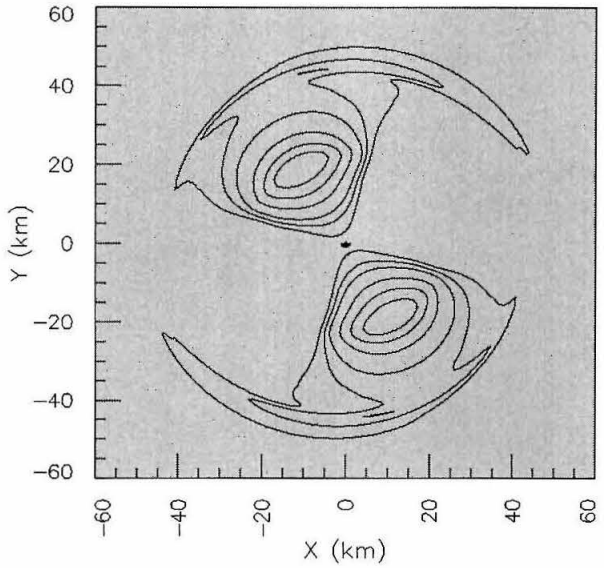

Figure 3.11: The eigenfunction of the physical density perturbation $\delta\tilde{\rho}$ on the equatorial plane for the bar mode of the most rapidly rotating star ($\beta = 0.261$). The density perturbations are normalized so that the maximum value is one. Only positive density regions of the eigenfunction are shown. The negative structure of the eigenfunction can be inferred from the sinusoidal structure of the eigenfunction. The contour levels are, from inward to outward, 0.8, 0.6, 0.4, 0.2, 0.1 and 0.01. The small arcs inside the 0.1 contours are additional contours of 0.2, corresponding to the secondary peak in Fig. 3.10.

Table 3.2: The oscillation frequency f and e-folding time τ of the most unstable bar mode for several unstable neutron stars. Here Ω is the rotational frequency of the pre-collapse white dwarf, and Ω_m is the maximum frequency of the white dwarf in Sequence III.

$(\Omega/\Omega_m)_{WD}$	β	$\mathrm{Re}(-\omega)$ rad s^{-1}	f Hz	τ ms
0.934	0.251	2800	445	20
0.964	0.255	2850	450	12
0.989	0.258	2850	450	8.9
1.000	0.261	2890	460	7.8

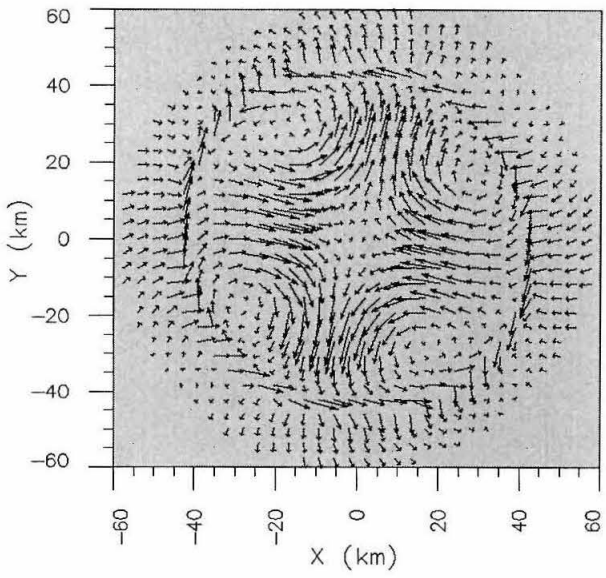

Figure 3.12: The eigenfunction of the physical velocity perturbation $\delta\tilde{v}^a$ on the equatorial plane for the bar mode of the most rapidly rotating star ($\beta = 0.261$).

($\approx$ 450 Hz) for all the cases. We do not observe any instability in our simulations for stars with $\beta \leq 0.241$. Hence we conclude that β_d is somewhere between 0.241 and 0.251, and the pre-collapse white dwarf has to have $\Omega \gtrsim 0.93\Omega_m$ in order for the collapsed star to develop a dynamical instability.

3.4 Gravitational radiation

In this section, we estimate the strength of the gravitational radiation emitted by neutron stars undergoing a dynamical instability. We also estimate the signal-to-noise ratio and discuss the detectability of these sources.

The rms amplitude of a gravitational wave strain, $h(t)$, depends on the orientation of the source and its location on the detector's sky. When averaged over these angles, its value is given by [35]

$$h^2(t) = \frac{1}{5}\langle h_+^2(t) + h_\times^2(t)\rangle \ , \tag{3.32}$$

where $h_+(t)$ and $h_\times(t)$ are the rms amplitudes of the plus and cross polarizations of the wave respectively, and $\langle ...\rangle$ denotes an average over the orientation of the source and its location on the detector's sky.

In the presence of perturbations, the density and velocity of fluid inside the star become

$$\rho(\boldsymbol{x},t) = \rho_0(\varpi,z) + \sum_{m=-\infty}^{\infty} \delta\rho_m(\boldsymbol{x},t) \tag{3.33}$$

$$\boldsymbol{v}(\boldsymbol{x},t) = \varpi\Omega(\varpi)\boldsymbol{e}_{\hat{\varphi}} + \sum_{m=-\infty}^{\infty} \delta\boldsymbol{v}_m(\boldsymbol{x},t) \ , \tag{3.34}$$

where the perturbation functions $\delta\rho_m$ and $\delta\boldsymbol{v}_m$ have angular dependence $e^{im\varphi}$. The amplitude of the gravitational waves produced by time varying mass and current multipole moments can be derived from Ref. [36]. The result is

$$h^2 = \frac{1}{D^2}\sum_{l=2}^{\infty}\sum_{m=-l}^{l}\frac{4G^2}{5c^{2l+4}}N_l\left[|D_{lm}^{(l)}|^2 + |S_{lm}^{(l)}|^2\right] \ , \tag{3.35}$$

where D is the distance between the source and detector; c is the speed of light, and

$$N_l = \frac{4\pi(l+1)(l+2)}{l(l-1)[(2l+1)!!]^2} \ ; \tag{3.36}$$

$$D_{lm}^{(l)} = \frac{d^l}{dt^l}D_{lm} \ ; \tag{3.37}$$

$$S_{lm}^{(l)} = \frac{d^l}{dt^l}S_{lm} \ . \tag{3.38}$$

For a Newtonian source, the mass moments D_{lm} and current moments S_{lm} are given by

$$D_{lm} = \int \rho r^l Y_{lm}^* \, d^3x \tag{3.39}$$

$$S_{lm} = \frac{2}{c}\sqrt{\frac{l}{l+1}}\int r^l \rho\boldsymbol{v}\cdot\boldsymbol{Y}_{\boldsymbol{lm}}^{\boldsymbol{B}\,*}\, d^3x \ , \tag{3.40}$$

where $\boldsymbol{Y}_{\boldsymbol{lm}}^{\boldsymbol{B}} = \boldsymbol{x}\times\boldsymbol{\nabla}Y_{lm}/\sqrt{l(l+1)}$ are the magnetic type vector spherical harmonics. The functions D_{lm} and S_{lm} have the property that $D_{lm}^* = (-1)^m D_{l\,-m}$ and $S_{lm}^* = (-1)^m S_{l\,-m}$. Hence it is sufficient to consider only positive values of m and Eq. (3.35) becomes

$$h^2 = \frac{1}{D^2}\sum_{l=2}^{\infty}\sum_{m=0}^{l}\frac{8G^2}{5c^{2l+4}}N_l\left[|D_{lm}^{(l)}|^2 + |S_{lm}^{(l)}|^2\right] \ . \tag{3.41}$$

The energy and angular momentum carried by the gravitational waves can also be derived

from [36]. The result is

$$\dot{E} = \sum_{l=2}^{\infty}\sum_{m=0}^{l}\frac{G}{c^{2l+1}}\,2N_l\overline{\left[|D_{lm}^{(l+1)}|^2+|S_{lm}^{(l+1)}|^2\right]}\;; \tag{3.42}$$

$$\dot{J} = \sum_{l=2}^{\infty}\sum_{m=0}^{l}\frac{G}{c^{2l+1}}\,2imN_l\overline{\left[D_{lm}^{(l)*}D_{lm}^{(l+1)}+S_{lm}^{(l)*}S_{lm}^{(l+1)}\right]}\;, \tag{3.43}$$

where the overline denotes time average over several periods.

When a neutron star develops a dynamical instability and the bar mode ($m = 2$) is the only unstable mode, the values of h, $\dot{E}$ and $\dot{J}$ will be dominated by the term involving D_{22}. Since the unstable bar mode has even parity under reflection about the equatorial plane, $D_{32} = S_{22} = 0$ and the next leading term will involve S_{32} and D_{42}. These terms are expected to be smaller than the D_{22} term by a factor of $(v/c)^4$ for $\dot{E}$ and $\dot{J}$, and a factor of $(v/c)^2$ for h. In our models, $v/c < 0.28$, so the contribution of higher order mass and current multipole moments are small and will be neglected.

Strictly speaking, the above analysis only applies when the amplitudes of the perturbations are small. When the amplitudes are large, however, the fluid motion does not separate neatly into decoupled Fourier components, so all D_{lm} and S_{lm} will contribute. However, it is expected that the D_{22} term will still be the most important term. Since the detailed nonlinear evolution of the dynamical instability is not known, the aim of this section is to provide an order of magnitude estimate of the gravitational radiation from these sources. Hence we shall only consider the effect of the mass quadrupole moment and assume D_{22} can be approximated by the bar-mode eigenfunctions computed in Sec. 3.3.2. In this approximation, Eqs. (3.41)–(3.43) become

$$h = \frac{32\pi^2 G}{5c^4 D}f^2|D_{22}|\sqrt{\frac{\pi}{15}}\;; \tag{3.44}$$

$$\dot{E} = \frac{1024\pi^7 G}{75c^5}f^6|D_{22}|^2\;; \tag{3.45}$$

$$\dot{J} = \frac{1024\pi^6 G}{75c^5}f^5|D_{22}|^2\;, \tag{3.46}$$

where $f = |\mathrm{Re}(\omega)|/(2\pi)$ is the oscillation frequency of the bar mode.

Substituting the bar-mode eigenfunctions (from Sec. 3.3.2) into Eq. (3.39), we find that

$$|D_{22}| \approx \alpha\, 8\times 10^{45}\ \mathrm{g\ cm^2} \tag{3.47}$$

for all the unstable models we have studied. Here α is the amplitude of the bar mode defined in Eq. (3.27). The mass quadrupole moment D_{22} has a time dependence $\exp(i\omega t)$, where ω is the

angular frequency of the mode. Hence the time derivative $D_{22}^{(l)} = (i\omega)^l D_{22}$ and we obtain

$$h \approx \alpha\, 7 \times 10^{-23} \left(\frac{20\ \mathrm{Mpc}}{D}\right) ; \tag{3.48}$$

$$\dot{E} \approx \alpha^2\, 9 \times 10^{52}\ \mathrm{erg\ s^{-1}} ; \tag{3.49}$$

$$\dot{J} \approx \alpha^2\, 6 \times 10^{49}\ \mathrm{g\ cm^2\ s^{-2}} . \tag{3.50}$$

The signal-to-noise ratio of these sources depends on the detailed evolution of the bar mode when the density perturbation reaches a large amplitude and nonlinear effects take over. Recently, New, Centrella and Tohline [11] and Brown [34] performed long-duration simulations of the bar-mode instability. They found that the mode saturates when the density perturbation is comparable to the equilibrium density, and the mode pattern persists, giving a long-lived gravitational wave signal. Here we assume that this is the case, and that the mode dies out only after a substantial amount of angular momentum is removed from the system by gravitational radiation. We then follow the method described in Refs. [37, 38] to estimate the signal-to-noise ratio.

In the stationary phrase approximation, the gravitational wave in the frequency domain $\tilde{h}(f)$ is related to $h(t)$ by

$$h^2(t) = |\tilde{h}(f)|^2 \left|\frac{df}{dt}\right| . \tag{3.51}$$

Combining Eqs. (3.44), (3.46) and (3.51), we obtain

$$|\tilde{h}(f)|^2 = \frac{G}{c^3} \frac{\dot{J}}{5\pi f |\dot{f}| D^2} . \tag{3.52}$$

The signal-to-noise ratio is given by

$$\left(\frac{S}{N}\right)^2 = 2 \int_0^\infty \frac{|\tilde{h}(f)|^2}{S_h(f)}\, df , \tag{3.53}$$

where $S_h(f)$ is the spectral density of the detector's noise. If we assume that the oscillation frequency remains constant in the entire evolution, we obtain [39]

$$\frac{S}{N} = \frac{1}{D} \sqrt{\frac{2G}{5\pi c^3} \frac{\Delta J}{f S_h(f)}} , \tag{3.54}$$

where ΔJ is the total amount of angular momentum emitted by gravitational waves. To estimate ΔJ, we assume that the mode dies out when the angular momentum of the star decreases to $J_d \approx 3.3 \times 10^{49}\ \mathrm{g\ cm^2\ s^{-1}}$, which is the angular momentum of the marginally bar-unstable star.

Then we have $\Delta J \lesssim 5 \times 10^{48}$ g cm^2 s^{-1} for all the unstable stars, and the signal-to-noise ratio for LIGO-II broad-band interferometers [40] is

$$\begin{aligned} \frac{S}{N} &= 15 \left(\frac{20 \text{ Mpc}}{D}\right) \left(\frac{\Delta J}{5 \times 10^{48} \text{ cgs}}\right)^{1/2} \times \\ &\left(\frac{f}{450 \text{ Hz}}\right)^{-1/2} \left(\frac{\sqrt{S_h(f)}}{2 \times 10^{-24} \text{ Hz}^{-1/2}}\right)^{-1} . \end{aligned} \tag{3.55}$$

The timescale of the gravitational wave emission can be estimated by the equation

$$\begin{aligned} \tau_{GW} &\sim \frac{\Delta J}{\dot{J}} \\ &\sim 7 \text{ s} \left(\frac{\alpha_s}{0.1}\right)^{-2} \left(\frac{\Delta \text{J}}{5 \times 10^{48} \text{ cgs}}\right) , \end{aligned} \tag{3.56}$$

where α_s is the amplitude α of the density perturbation at which the mode saturates. We have used Eqs. (3.46) and (3.47) to calculate the numerical value in the last equation.

The detectability of this type of sources also depends on the event rate. The event rate for the AIC in a galaxy is estimated to be between 10^{-5} and 10^{-8} per year [41, 42]. Of all the AIC events, only those corresponding to the collapse of rapidly rotating O-Ne-Mg white dwarfs can end up in the bar-mode instability, and the fraction of which is unknown. If a signal-to-noise ratio of 5 is required to detect the source, an event rate of at least 10^{-6}/galaxy/year is required for such a source to occur at a detectable distance per year. Hence these sources will not be promising for LIGO II if the event rate is much less than 10^{-6} per year per galaxy.

The event rate of the core collapse of massive stars is much higher than that of the AIC. The structure of a pre-supernova core is very similar to that of a pre-collapse white dwarf, so our results might be applicable to the neutron stars produced by the core collapse. If the core is rapidly rotating, the resulting neutron star might be able to develop a bar-mode instability. If a significant fraction of the pre-supernova cores are rapidly rotating, the chance of detecting the gravitational radiation from the bar-mode instability might be much higher than expected.

3.5 Magnetic field effects

As mentioned in Sec. 3.2.2, a new-born hot protoneutron star is dynamically stable because its β is too small. It takes about 20 s for the protoneutron star to cool down and evolve into a cold neutron star, which may have high enough β to trigger a dynamical instability. The protoneutron stars, as well as the cold neutron stars computed in Sec. 3.2.2, show strong differential rotation (see

Chapter 2). This differential rotation will cause a frozen-in magnetic field to wind up, creating strong toroidal fields. This process will result in a re-distribution of angular momentum and destroy the differential rotation. If the timescale of this magnetic braking is shorter than the cooling timescale, the star may not be able to develop the dynamical instability discussed in Secs. 3.3 and 3.4. In this section, we estimate the timescale of this magnetic braking.

In the ideal magnetohydrodynamics limit, the magnetic field lines are frozen into the moving fluid. The evolution of magnetic field B is governed by the induction equation

$$\frac{\partial B^a}{\partial t} + v^b \nabla_b B^a - B^b \nabla_b v^a = -B^a \nabla_b v^b \ . \tag{3.57}$$

In our equilibrium models, $v^b = \varpi\Omega(\varpi) e^b_{\hat{\varphi}}$. Hence $\nabla_b v^b = 0$ and Eq. (3.57) becomes

$$\frac{dB^a}{dt} = B^b \nabla_b v^a \ , \tag{3.58}$$

where $d/dt = \partial/\partial t + v^b \nabla_b$ is the time derivative in the fluid's co-moving frame. Equation (3.58) can be integrated analytically (see, e.g., Appendix B of [43]). The magnetic field $B^j(\boldsymbol{x}, t)$ at the position $\boldsymbol{x}$ of a fluid element at time t is related to the magnetic field $B^k(\boldsymbol{x_0}, t_0)$ at the position $\boldsymbol{x_0}$ of the same fluid at time t_0 by

$$B^j(\boldsymbol{x}, t) = B^k(\boldsymbol{x_0}, t_0) \frac{\partial x^j}{\partial x_0^k} \ , \tag{3.59}$$

where $\partial x^j / \partial x_0^k$ is the coordinate strain between t_0 and t. With $v^a = \varpi\Omega(\varpi) e^a_{\hat{\varphi}}$, it is easy to show that the induced magnetic field has components only in the $e^a_{\hat{\varphi}}$ direction. Its magnitude B_i, after a time t, is easy to compute from Eq. (3.59). The result is

$$B_i(t) = B_0 t \varpi |\partial_\varpi \Omega| \ , \tag{3.60}$$

where B_0 is the component of magnetic field in the $\boldsymbol{e}_\varpi$ direction. The induced magnetic field will significantly change the equilibrium velocity field when the energy density of magnetic field $\epsilon_B = B_i^2/(8\pi)$ is comparable to the rotational kinetic energy density $\epsilon_R = \rho\varpi^2\Omega^2/2$. This will occur in a timescale τ_B set by $\epsilon_B = \epsilon_R$. Using Eq. (3.60), we obtain

$$\tau_B = \frac{\Omega}{|\partial_\varpi \Omega|} \frac{\sqrt{4\pi\rho}}{B_0} = \frac{L}{v_A} \ , \tag{3.61}$$

where $L = \Omega/|\partial_\varpi \Omega|$ is the length scale of differential rotation, and $v_A = B_0/\sqrt{4\pi\rho}$ is the speed of

Alfvèn waves.

Observational data suggest that the magnetic fields of most white dwarfs are smaller than 10^5 G, although a small fraction of "magnetic white dwarfs" can have fields in the range 10^6–10^9 G. Assuming flux conservation, the magnetic fields of the hot protoneutron stars just after collapse would be $B_0 \sim 10^9$ G for those 10^5 G white dwarfs. Using the angular velocity distribution in Chapter 2 for the hot protoneutron star, we find that the magnetic timescale in the dynamically important region ($\varpi \lesssim 100$ km) is

$$\tau_B \approx 10^4 \text{ s} \left(\frac{10^9 \text{ G}}{B_0}\right) , \tag{3.62}$$

which is much longer than the neutrino cooling timescale (~ 20 s). Hence the angular momentum transport caused by the magnetic field is negligible during the cooling period. The magnetic timescale for the cold neutron stars can be calculated from the angular frequency distribution computed in Sec. 3.2.2. We find that τ_B for the cold models is about half of that given by Eq. (3.62), which is still much longer than the timescale of gravitational waves τ_{GW} calculated in the previous Section. The instability results presented in the previous two sections remain unchanged unless the neutron star's initial magnetic field B_0 is greater than 10^{12} G. In that case, a detailed magnetohydrodynamical simulation has to be carried out to compute the angular momentum transport.

The magnetic timescale for these nascent neutron stars is significantly different from that estimated by Baumgarte, Shapiro and Shibata [44] and Shapiro [45]. They consider differentially rotating "hypermassive" neutron stars, which could be the remnants of the coalescence of binary neutron stars. Those neutron stars are very massive ($M \sim 3M_\odot$) and have much higher densities than the new-born neutron stars studied in this chapter. They also use a seed magnetic field of strength $B_0 \sim 10^{12}$ G, which is much larger than our estimate. These two differences combined make our magnetic braking timescale two orders of magnitude larger than theirs. It should be noted that it is the magnetic field just after the collapse that is relevant to our analysis here. The strong differential rotation of the neutron star will eventually generate a very strong toroidal field ($B_i \sim 10^{16}$ G) and destroy the differential rotation. The final state of the neutron star will be in rigid rotation, and its magnetic field will be completely different from the initial field. For this reason, the field strength $B \sim 10^{12}$ G observed in a typical pulsar is probably not relevant here.

3.6 Summary and discussion

We have applied linear stability analysis to study the dynamical stability of new-born neutron stars formed by AIC. We find that a neutron star has a dynamically unstable bar mode if its β is greater than the critical value $\beta_d \approx 0.25$. In order for the neutron star to have $\beta > \beta_d$, the pre-collapse white dwarf must be composed of oxygen, neon, magnesium and have a rotational angular frequency $\Omega \gtrsim 3.4$ rad s^{-1}, corresponding to 93% of the maximum rotational frequency the white dwarf can have without mass shedding.

The eigenfunction of the most unstable bar mode is concentrated within a radius $\varpi \lesssim 60$ km. The oscillation frequency of the mode is $f \approx 450$ Hz. When the amplitude of the mode is small, it grows exponentially with an e-folding time $\tau \approx 8$ ms for the most rapidly rotating star ($\beta = 0.261$), which is about 5.5 rotation periods at the center of the star.

The signal-to-noise ratio of the gravitational waves emitted by this instability is estimated to be 15 for LIGO-II broad-band interferometers if the source is located in the Virgo cluster of galaxies ($D = 20$ Mpc). The detectability of these sources also depends on the event rate. The event rate of AIC is between 10^{-5} and 10^{-8}/galaxy/year. Only those AIC events corresponding to the collapse of rapidly rotating O-Ne-Mg white dwarfs can end up in the bar-mode instability. While it is likely that the white dwarfs would be spun up to rapidly rotation by the accretion gas prior to collapse [17], it is not clear how many of the AIC events are related to the O-Ne-Mg white dwarfs. If the event rate is less than 10^{-6}/galaxy/year, it is not likely that LIGO II will detect these sources. However, the event rate of the core collapse of massive stars is much higher than that of the AIC. A bar-mode instability could develop for neutron stars formed from the collapse of rapidly rotating pre-supernova cores. If a significant fraction of the cores are rapidly rotating, the chance of detecting the gravitational radiation from bar-mode instability would be much higher.

If the pre-collapse white dwarf is differentially rotating, the resulting neutron star can have a higher value of β. The bar-mode instability is then expected to last for a longer time. However, any differential rotation will be destroyed by magnetic fields in a timescale $\tau_B \sim R/v_A$, where R is the size of the white dwarf and $v_A = B/\sqrt{4\pi\bar{\rho}} \sim B\sqrt{R^3/(3M)}$. For a massive white dwarf with $M = 1.4M_\odot$,

$$\tau_B \sim 2 \text{ yrs } \left(\frac{10^5 \text{ G}}{\text{B}}\right)\left(\frac{\text{R}}{1500 \text{ km}}\right)^{-1/2}, \tag{3.63}$$

which is much shorter than the accretion timescale. Hence rigid rotation is a good approximation for pre-collapse white dwarfs.

The magnetic field of a neutron star is much stronger than that of a white dwarf. The timescale for a magnetic field to suppress differential rotation depends on the initial magnetic field B_0 of the protoneutron star. If the magnetic field of the pre-collapse white dwarf is of order 10^5 G, the initial field will be $B_0 \sim 10^9$ G according to conservation of magnetic flux. In this case, the magnetic timescale is $\tau_B \sim 10^4$ s. This timescale is much longer than the time required for a hot protoneutron star to cool down and turn into a cold neutron star, and go through the whole dynamical instability phase. If $B_0 \gtrsim 10^{12}$ G, a significant amount of angular momentum transport will take place during the cooling phase. A detailed magnetohydrodynamical simulation has to be carried out to study the transport process in this case. However, such a strong initial magnetic field is possible only if the pre-collapse white dwarf has a magnetic field $B \gtrsim 10^8$ G.

Finally, we want to point out that the collapse of white dwarfs will certainly produce asymmetric shocks and may eject a small portion of the mass. We expect that our neutron star models describe fairly well the inner cores of the stars but not the tenuous outer layers. Our stability results are sensitive to the region with $\varpi \lesssim 100$ km. The results could change considerably if the structure in this region is very different from that of our models. This issue will hopefully be resolved by the future full 3-D AIC simulations.

Acknowledgements

I thank Lee Lindblom for his guidance on all aspects of this work. I also thank Kip S. Thorne and Stuart L. Shapiro for useful discussions. This research was supported by NSF grants PHY-9796079 and PHY-0099568, and NASA grant NAG5-4093.

3.7 Appendix: Resonance at the co-rotation radius

We see from Figs. 3.10–3.12 that the bar-mode eigenfunction has peculiar structures at the co-rotation radius ($\varpi \approx 40$ km) at which $\omega + 2\Omega \approx 0$. The density perturbation has a small peak and the velocity perturbation is almost parallel to the φ direction. In this section, we shall show that these are caused by the resonance of the fluid driven by the mode.

For simplicity, we only consider the fluid's motion on the equatorial plane. Assume that the perturbations are dominated by a mode that goes as $\exp(i\omega t + im\varphi)$. We also assume that this mode is even under the reflection $z \to -z$. Hence we have $\xi^z = 0$ and $\delta v^z = 0$. In cylindrical

coordinates, the linearized Euler equation takes the form

$$i(\omega + m\Omega)\delta v^{\varpi} = 2\Omega\delta v^{\hat{\varphi}} - \frac{\partial_{\varpi}\delta P}{\rho} + \frac{\partial_{\varpi}P}{\rho^2}\delta\rho - \partial_{\varpi}\delta\Phi \ , \tag{3.64}$$

$$i(\omega + m\Omega)\delta v^{\hat{\varphi}} = -(\varpi\partial_{\varpi}\Omega + 2\Omega)\delta v^{\varpi} - \frac{im}{\varpi}\left(\frac{\delta P}{\rho} + \delta\Phi\right) \ . \tag{3.65}$$

The density perturbation $\delta\rho$ is related to the pressure perturbation δP by

$$\delta\rho = \frac{\rho}{\gamma_p P}\delta P - \left(1 - \frac{\gamma_{\rm eq}}{\gamma_p}\right)\xi^{\varpi}\partial_{\varpi}\rho \ . \tag{3.66}$$

The ϖ-component of the Lagrangian displacement is given by

$$\xi^{\varpi} = \frac{\delta v^{\varpi}}{i(\omega + m\Omega)} \ . \tag{3.67}$$

Our numerical simulations show that δP is well behaved and smooth near the co-rotation radius at which $\omega + m\Omega \approx 0$. The perturbed gravitational potential $\delta\Phi$ is expected (and is confirmed by our numerical simulations) to be smooth since it depends on the overall distribution of the density perturbation. We can then use Eqs. (3.64)–(3.67) to express all the other perturbed quantities in terms of δP and $\delta\Phi$. Near the co-rotation radius, the expressions are:

$$\delta\rho = \frac{\rho}{\gamma_p P}\delta P - \left(1 - \frac{\gamma_{\rm eq}}{\gamma_p}\right)\frac{\delta v^{\varpi}\partial_{\varpi}\rho}{i(\omega + m\Omega)} \ , \tag{3.68}$$

$$\delta v^{\varpi} \approx \frac{-2im\Omega}{\varpi(\kappa^2 + B)}\left(\frac{\delta P}{\rho} + \delta\Phi\right) \ , \tag{3.69}$$

$$\delta v^{\hat{\varphi}} = \frac{i}{\omega + m\Omega}\left[\frac{\kappa^2}{2\Omega}\delta v^{\varpi} + \frac{im}{\varpi}\left(\frac{\delta P}{\rho} + \delta\Phi\right)\right] \ , \tag{3.70}$$

$$\kappa^2 = \varpi\partial_{\varpi}\Omega^2 + 4\Omega^2 \ , \tag{3.71}$$

$$B = \frac{\partial_{\varpi}P\partial_{\varpi}\rho}{\rho^2}\left(1 - \frac{\gamma_{\rm eq}}{\gamma_p}\right) \ . \tag{3.72}$$

It follows from Eqs. (3.67) and (3.66) that if $|\delta v^{\varpi}|$ is not of order $(\omega + m\Omega)$ near the co-rotation radius, both $|\xi^{\varpi}|$ and $|\delta\rho|$ will be large. The large magnitude of the Lagrangian displacement is caused by the fluid being driven in resonance by the mode. The large displacement of the fluid causes $|\delta\rho|$ to be large due to the second term of Eq. (3.66). This term arises because of the different compressibilities of stationary and oscillating fluid (i.e., $\gamma_{\rm eq} \neq \gamma_p$). In the case of the bar mode ($m = 2$), the co-rotation radius is located at $\varpi_c \approx 40$ km. The equilibrium density on the equator $\rho(\varpi_c, 0) \approx 10^{12}$ g cm^{-3} and the stationary fluid is very compressible ($\gamma_{\rm eq} \approx 0.7$). The high

compressibility of the stationary fluid make the background equilibrium density ρ drop rapidly as ϖ increases, i.e., $|\partial_\varpi \rho|$ is large. The oscillating fluid is far less compressible ($\gamma_p = 1.35$). As a result, when the oscillating fluid moves to a new location, it does not expand or compress to an extent that can compensate for the difference between the background densities at the old and new locations. Since both $|\xi^\varpi|$ and $|\partial_\varpi \rho|$ are large, $\delta\rho$ is dominated by the second term of Eq. (3.66) near the co-rotation radius. This explains the narrow secondary peak of $\delta\rho$ seen in Fig. 3.10. We see from Eq. (3.70) that $|\delta v^{\hat{\varphi}}| \gg |\delta v^\varpi|$ and $\delta v^{\hat{\varphi}}$ changes rapidly near the co-rotation radius, which explains the flow pattern seen in Fig. 3.12.

Bibliography

[1] K. S. Thorne, in *Black Holes and Relativistic Stars*, ed. R. M. Wald (The University of Chicago Press, 1998).

[2] S. Chandrasekhar, *Ellipsoidal Figures of Equilibrium* (New Haven: Yale University Press, 1969).

[3] J. E. Tohline, R. H. Durisen and M. McCollough, Astrophys. J., **298**, 220, 1985.

[4] R. H. Durisen, R. A. Gingold, J. E. Tohline and A. P. Boss, Astrophys. J., **305**, 281, 1986.

[5] H. A. Williams and J. E. Tohline, Astrophys. J., **334**, 449, 1988.

[6] J. L. Houser, J. M. Centrella and S. C. Smith, Phys. Rev. Lett., **72**, 1314, 1994.

[7] S. Smith, J. L. Houser and J. M. Centrella, Astrophys. J., **458**, 236 (1996).

[8] J. L. Houser and J. M. Centrella, Phys. Rev. D., **54**, 7278 (1996).

[9] B. K. Pickett, R. H. Durisen and R. H. Davis, Astrophys. J., **458**, 714 (1996).

[10] J. L. Houser, Mon. Not. Roy. Astro. Soc., **299**, 1069 (1998).

[11] K. C. B. New, J. M. Centrella and J. E. Tohline, Phys. Rev. D, **62**, 064019 (2000).

[12] J. N. Imamura and J. Toman, Astrophys. J, **444**, 363 (1995).

[13] J. M. Centrella, K. C. B. New, L. L. Lowe and J. D. Brown, Astrophys. J. Lett., **550**, 193 (2001).

[14] N. Stergioulas and J. L. Friedman, Astrophys. J., **492**, 301 (1998).

[15] M. Shibata, T. W. Baumgarte and S. L. Shapiro, Astrophys. J., **542**, 453 (2000).

[16] M. Saijo, M. Shibata, T. W. Baumgarte and S. L. Shapiro, Astrophys. J., **548**, 919 (2001).

[17] C. L. Fryer, D. E. Holz and S. A. Hughes, to appear in Astrophys. J., astro-ph/0106113 (2001).

[18] See, e.g., R. Narayan and R. Popham, Astrophys. J. Lett., **346**, 25 (1989).

[19] K. Nomoto, in *Proc. 13th Texas Symp. on Relativistic Astrophysics*, edited by M. Ulmer, (World Scientific, Singapore, 1987).

[20] K. Nomoto and Y. Kondo, Astrophys. J. **367**, L19 (1991).

[21] E. Bravo and D. García-Senz, Mon. Not. Roy. Astro. Soc., **307**, 984 (1999).

[22] E. E. Salpeter, Astrophys. J., **134**, 669 (1961).

[23] I. Hachisu, Astrophys. J. Supp., **61**, 479 (1986).

[24] J.-L. Tassoul, *Theory of Rotating Stars*, Princeton Univ. Press (1978).

[25] H. A. Bethe and M. B. Johnson, Nucl. Phys. A, **230**, 1 (1974).

[26] G. Baym, H. A. Bethe and C. J. Pethick, Nucl. Phys. A, **175**, 225 (1971).

[27] S. Smith and J. M. Centrella, in *Approaches to Numerical Relativity*, edited by R. d'Inverno, Cambridge University Press, New York (1992).

[28] J. T. Toman, J. N. Imamura, B. K. Pickett and R. H. Durisen, Astrophys. J., **497**, 370 (1998).

[29] D. W. Meltzer and K. S. Thorne, Astrophys. J., **145**, 514 (1966).

[30] M. Colpi, S. L. Shapiro and S. A. Teukolsky, Astrophys. J., **339**, 318 (1989).

[31] L. S. Finn and C. R. Evans, Astrophys. J., **351**, 588 (1990).

[32] L. Lindblom and S. L. Detweiler, Astrophys. J. Supp., **53**, 73 (1983).

[33] J. N. Imamura, R. H. Durisen and B. K. Pickett, Astrophys. J., **528**, 946 (2000).

[34] J. D. Brown, Phys. Rev. D., **62**, 0004002 (2000).

[35] See, e.g., K. S. Thorne in *Three Hundred Years of Gravitation*, edited by S. W. Hawking and W. Israel (Cambridge University Press 1987).

[36] K. S. Thorne, Rev. Mod. Phys., **52**, 299 (1980).

[37] B. J. Owen, L. Lindblom, C. Cutler, B. F. Schutz, A. Vecchio and N. Andersson, Phys. Rev. D **58**, 084020 (1998).

[38] B. J. Owen and L. Lindblom, gr-qc/0111024 (2001).

[39] This formula was first derived by R. D. Blandford (unpublished).

[40] E. Gustafson, D. Shoemarker, K. Strain and R. Weiss, LIGO Document T990080-00-D.

[41] V. Kalogera, in *Gravitational Waves: Third Edoardo Amaldi Conference*, edited by S. Meshkov (American Institute of Physics, Melville, NY, 2000).

[42] C. L. Fryer, W. Benz, S. A. Colgate and M. Herant, Astrophys. J., **516**, 892 (1999).

[43] L. Rezzolla, F. K. Lamb, D. Marković and S. L. Shapiro, Phys. Rev. D, **64**, 104013 (2001).

[44] T. W. Baumgarte, S. L. Shapiro and M. Shibata, Astrophys. J. Lett., **528**, 29 (2000).

[45] S. L. Shapiro, Astrophys. J., **544**, 397 (2000).

Chapter 4

Post-Newtonian Structures of Differentially Rotating Neutron Stars

To be submitted to *Physical Review D.*

Abstract A self-consistent field method is developed, which can be used to construct models of differentially rotating stars to first post-Newtonian order. The rotation law is specified by the specific angular momentum distribution $j(m_\varpi)$, where m_ϖ is the baryonic mass fraction inside the surface of constant specific angular momentum. The method is then used to compute models of the nascent neutron stars resulting from the accretion induced collapse of white dwarfs. The ratios of kinetic energy to gravitational binding energy, β, of the relativistic models are found to be slightly smaller than the corresponding values of the Newtonian models.

4.1 Introduction

We have demonstrated in Chapter 3 that the accretion induced collapse (AIC) of a rapidly rotating white dwarf can result in a rapidly rotating neutron star that is dynamically unstable to the bar-mode instability. This instability could emit a substantial amount of gravitational radiation that could be detectable by gravitational wave interferometers, such as LIGO, VIRGO, GEO and TAMA.

However, for this instability to occur, the neutron star must have a $\beta = T/|W|$ greater than a critical value $\beta_d \approx 0.25$. Here T is the rotational kinetic energy and $|W|$ is the gravitational binding energy. Only the AIC of O-Ne-Mg white dwarfs with $\Omega > 0.93\Omega_m$ can produce neutron stars with such a high value of β. Here Ω is the angular velocity of the white dwarf and Ω_m is the angular

velocity at which mass shedding occurs on the equatorial surface. This type of source will not be promising for LIGO II because its event rate is not very high.

Neutron stars are compact objects and general relativistic effects have a significant influence on both the structure and dynamical stability of the stars. Recently, Shibata, Baumgarte, Saijo and Shapiro studied the dynamical stability of differentially rotating polytropes in full general relativity [1] and in the post-Newtonian approximation [2]. They performed numerical simulations on the differentially rotating polytropes with some specified rotation law. They found that as the star becomes more compact, the critical value β_d slightly decreases from the Newtonian value 0.26 to 0.24 for their chosen rotation law. It is not clear, however, whether their result implies that the relativistic effects would destabilize the stars we are studying, for the equilibrium structure of the star will also be changed by the relativistic effects. The value of β of a relativistic star will not be the same as that of a Newtonian star with the same baryon mass and total angular momentum. The objective of this chapter is first to develop a new numerical technique which can be used to construct the equilibrium structure of a rotating star with a specified specific angular momentum distribution to first post-Newtonian (1PN) order [i.e., including terms of order c^{-2} higher than the Newtonian terms in the equations of motion]. Then we construct models of neutron stars corresponding to the collapse of the white dwarfs we studied in Sections 2.2 and 3.2.1 and compare them with the Newtonian models.

Equilibrium models of neutron stars in full general relativity have been built by many authors [3, 4, 5, 6, 7, 8, 9]. The neutron stars studied in the literature are either rigidly rotating or rotating with an *ad hoc* rotation law. New-born neutron stars resulting from core collapse of massive stars or accretion induced collapse of massive white dwarfs are differentially rotating [10, 11, 12] (see also Sections 2.3 and 3.2.2). It seems plausible that the rotation laws of these neutron stars could be approximated by the specific angular momentum distribution $j(m_\varpi)$ of the pre-collapse stars (see Sections 2.3 and 4.2.1). Here m_ϖ is the baryonic mass fraction inside the surface of constant specific angular momentum. Equilibrium models of Newtonian stars with a specified $j(m_\varpi)$ have been constructed by many authors [13, 14, 15, 16]. However, none of these studies, to our knowledge, has been generalized to include the relativistic effects.

If a rotating axisymmetric star is described by a barotropic equation of state, i.e., the total energy density ϵ is a function of pressure only, then there is a constraint on the rotation law (see Section 4.2.1). This rotational constraint is usually written in the form $u^0 u_\varphi = F(\Omega)$ [17, 6], where F is an arbitrary function. Here Ω is the angular velocity of the fluid with respect to an inertial

observer at infinity; u^0 is the time component of the four-velocity and $u_\varphi = u_\mu \varphi^\mu$, where φ^α is the axial Killing vector field of the spacetime. In the Newtonian limit, this constraint reduces to the well-known result that Ω is constant in the direction parallel to the rotation axis. The major obstacle in the construction of differentially rotating relativistic stars is that it is not clear what function F should be used that will produce the desired specific angular momentum distribution $j(m_\varpi)$. In the next section, we will reformulate the rotational constraint in a way that can be used to impose the rotation law $j(m_\varpi)$, at least in the 1PN calculations.

The structure of this chapter is as follows. In Section 4.2, we give a brief review on the full relativistic treatment of rotating relativistic stars and then reformulate the rotational constraint imposed by the barotropic equation of state. Next, we use the standard 1PN metric and show that the rotational constraint can be solved analytically. We then derive the equations of motion determining the structure of a star to 1PN order. In Section 4.3, we generalize the self-consistent field method of Smith and Centrella [22], which can be used to compute the structure of a star to 1PN order. In Section 4.4, we apply the numerical method to construct neutron star models resulting from the collapse of the O-Ne-Mg white dwarfs we studied in Section 3.2.1 and compare them with the corresponding Newtonian models. Finally, we summarize our conclusions in Section 4.5.

4.2 Formalism

In this Section, we first give a brief review on the full relativistic treatment of rotating relativistic stars and then reformulate the rotational constraint imposed by the barotropic equation of state (EOS) in Section 4.2.1. Then we derive the equations of motion determining the equilibrium structure of a rotating star to 1PN order in Section 4.2.2. Throughout this chapter, we use the convention that Greek indices run from 0 to 4, 0 being the time component; whereas Latin indices run from 1 to 3 only. A sum over repeated indexes is assumed unless stated otherwise. The signature of the metric is $(-+++)$.

4.2.1 Full relativistic consideration

We want to construct the nascent neutron stars resulting from the AIC of rotating white dwarfs. As in Sec. 2.2, we make the following assumptions on the AIC and the collapsed stars.

First, we assume the collapse is axisymmetric. Hence the spacetime, albeit dynamical, has an axial Killing vector field φ^α. Second, we neglect viscosity and assume a perfect fluid stress-energy

tensor

$$T^{\mu\nu} = (\epsilon + P)u^\mu u^\nu + Pg^{\mu\nu} \ , \tag{4.1}$$

where ϵ is the energy density in the fluid's rest frame; P is pressure and u^μ is the fluid's four-velocity, normalized so that $u^\alpha u_\alpha = -1$. Third, we assume that the collapsed objects can be described by a barotropic EOS, i.e. $\epsilon = \epsilon(P)$. Fourth, we assume there is no meridional circulation in the equilibrium state of the collapsed objects. In other words, the fluid's four-velocity can be written as

$$u^\alpha = u^0 \left(t^\alpha + \frac{\Omega}{c} \varphi^\alpha \right) \ , \tag{4.2}$$

where t^α is the timelike Killing vector field of the spacetime of the collapsed star; c is the speed of light; Ω is the rotational angular velocity and u^0 is the time component of the four-velocity. Finally, we assume that no material is ejected from the star during and after the collapse. Hence the total baryon rest mass M_0 and the total angular momentum J are conserved.

Let n denote the baryon number density in the fluid's rest frame. It follows from the baryon number conservation law $\nabla_\nu (nu^\nu) = 0$ and conservation of energy-momentum $\nabla_\nu T^{\mu\nu} = 0$ that (see, e.g., [21])

$$\frac{d\epsilon}{dn} = \frac{\epsilon + P}{n} \ . \tag{4.3}$$

Given a barotropic EOS, the above equation can be integrated, giving

$$n(\epsilon) = n(\epsilon_0) \exp \left[\int_{\epsilon_0}^{\epsilon} \frac{d\epsilon'}{\epsilon' + P(\epsilon')} \right] \ . \tag{4.4}$$

We define the baryonic rest mass density $\rho = n\bar{m}_B$. Here $\bar{m}_B$ is the average baryon mass, defined so that

$$\lim_{\epsilon \to 0} \frac{\epsilon}{\rho c^2} = 1 \ . \tag{4.5}$$

It follows [17] from the conservation of baryon number $\nabla_\nu (nu^\nu) = 0$, conservation of energy-momentum $\nabla_\nu T^{\mu\nu} = 0$, and the existence of an axial Killing vector φ^α that

$$u^\beta \nabla_\beta j = \frac{dj}{d\tau} = 0 \ , \tag{4.6}$$

where τ is the proper time along the fluid particle's worldline and

$$j = \frac{\epsilon + P}{\rho c^2} u_\varphi \ . \tag{4.7}$$

Here $u_\varphi = u_\alpha \varphi^\alpha$. In the Newtonian limit, $j = \Omega \varpi^2$, which is the Newtonian expression of the specific angular momentum along the rotation axis. Here ϖ is the distance from the rotation axis. To generalize the Newtonian results in Section 2.3, we shall build neutron star models with the same baryon mass M_0, total angular momentum J, and specific angular momentum distribution $j(m_\varpi)$ as the pre-collapse white dwarfs. Here m_ϖ is the baryonic mass fraction inside the surface of constant j.

In the stationary and axisymmetric spacetime of a relativistic star, the Euler equation takes the form [17]

$$\frac{\nabla_\alpha P}{\epsilon + P} = -u^\beta \nabla_\beta u_\alpha = \nabla_\alpha (\ln u^0) - u^0 u_\varphi \frac{\nabla_\alpha \Omega}{c} \ . \tag{4.8}$$

Since the EOS is barotropic, the left side of Eq. (4.8) is a total differential. This imposes a constraint on the rotation law: the integrability condition for Eq. (4.8) is that the rotation law must have the form $u^0 u_\varphi = F(\Omega)$ [17, 6], where F is an arbitrary function. In the Newtonian limit, this rotational constraint means that Ω is constant in the direction parallel to the rotation axis. The constraint written in this form is not convenient for our purpose, as our rotation laws are specified by the function $j(m_\varpi)$. Hence, we formulate the constraint in another way: the integrability condition is that $u^0 u_\varphi \nabla_\alpha \Omega$ is an exact differential. In the language of differential forms, we require that $u^0 u_\varphi \tilde{d}\Omega$ be an exact form. This implies that its exterior derivative vanishes:

$$\tilde{d}(u^0 u_\varphi \tilde{d}\Omega) = 0 \ . \tag{4.9}$$

4.2.2 Post-Newtonian approximation

In this chapter, we calculate the structure of neutron stars to the first post-Newtonian order. We split the energy density into two terms [18]:

$$\epsilon = \rho c^2 \left(1 + \frac{\Pi}{c^2}\right) \ . \tag{4.10}$$

We adopt the 1PN metric (in Cartesian coordinates) developed by Chandrasekhar, and Blanchet, Damour and Schäfer [18, 19, 20]:

$$g_{00} = -\left(1 + \frac{2U}{c^2} + \frac{2U^2}{c^4}\right) + O(c^{-6}) \ , \tag{4.11}$$

$$g_{0i} = \frac{A_i}{c^3} + O(c^{-5}) \ , \tag{4.12}$$

$$g_{ij} = \left(1 - \frac{2U}{c^2}\right)\delta_{ij} + O(c^{-4}) \ . \tag{4.13}$$

The metric components satisfy the gauge condition

$$\sum_{i=1}^{3} \partial_i g_{i0} - \frac{1}{2c}\partial_t \left(\sum_{i=1}^{3} g_{ii}\right) = O(c^{-5}) \ , \tag{4.14}$$

$$\sum_{i=1}^{3} \partial_i g_{ij} + \frac{1}{2}\partial_j \left(g_{00} - \sum_{i=1}^{3} g_{ii}\right) = O(c^{-4}) \ . \tag{4.15}$$

In this metric, the components of the four-velocity are

$$u^0 = 1 + \frac{1}{c^2}\left(\frac{v^2}{2} - U\right) + \frac{1}{2c^4}\left(U^2 - 5Uv^2 + \frac{3}{4}v^4 + 2v^i A_i\right) + O(c^{-6}) \ , \tag{4.16}$$

$$u^i = \frac{v^i}{c}\left[1 + \frac{1}{c^2}\left(\frac{v^2}{2} - U\right)\right] + O(c^{-5}) \ , \tag{4.17}$$

where $v^i = cu^i/u^0$ and $v^2 = \delta_{ij}v^i v^j$. The potentials U and A_i satisfy the elliptic equations

$$D^j D_j U + \frac{8\pi G\rho}{c^2}U = 4\pi G\rho\left[1 + \frac{1}{c^2}\left(\Pi + 2v^2 + \frac{3P}{\rho}\right)\right] \ , \tag{4.18}$$

$$D^j D_j A_i = 16\pi G\rho\delta_{ik}v^k \ , \tag{4.19}$$

where D_j denotes the covariant derivative compatible with the three dimensional flat-space metric, and G is the gravitational constant.

We introduce cylindrical coordinates (ϖ, φ, z) with $\partial/\partial\varphi$ being the axial Killing vector, and $\varpi = \sqrt{x^2 + y^2}$. In this coordinate system, the velocity vector potential A_i has only one component: $A_\varphi = xA_y - yA_x$. Let $Q = A_\varphi/\varpi$. Then Q satisfies the equation

$$D^j D_j Q - \frac{Q}{\varpi^2} = 16\pi G\rho\Omega\varpi \ . \tag{4.20}$$

To 1PN order, we have

$$cu^0 u_\varphi = \varpi^2\Omega\left(1 + \frac{K}{c^2}\right) \ , \tag{4.21}$$

where

$$K = v^2 - 4U + \frac{Q}{v} \ . \tag{4.22}$$

Since $u^0 u_\varphi \nabla_\alpha \Omega$ is an exact differential, we can write

$$\nabla_\alpha f = \varpi^2 \Omega \left(1 + \frac{K}{c^2}\right) \nabla_\alpha \Omega \ , \tag{4.23}$$

where f is a scalar function. The rotational constraint (4.9) gives only one nontrivial equation for Ω because the spacetime is stationary and axisymmetric. To 1PN order, this equation can be solved analytically, giving

$$\Omega(\varpi, z) = \Omega_0(\varpi) + \frac{\varpi \partial_\varpi \Omega_0}{2c^2}[K(\varpi, z) - K_0(\varpi)] \ , \tag{4.24}$$

where $\Omega_0(\varpi) \equiv \Omega(\varpi, 0)$ and $K_0(\varpi) \equiv K(\varpi, 0)$. Eq. (4.23) can then be integrated and we obtain, up to an arbitrary additive constant,

$$\begin{aligned} f(\varpi, z) &= \frac{\varpi^2}{2}\Omega_0^2(\varpi) - \int_0^\varpi d\varpi' \, \varpi' \Omega_0^2(\varpi') \\ &\quad + \frac{1}{c^2}\left[\varpi^2 \Omega_0(\varpi)\, \Omega_1(\varpi, z) + \frac{\varpi^2}{2}\Omega_0^2(\varpi) K_0(\varpi) - I_1(\varpi)\right] \ , \end{aligned} \tag{4.25}$$

where

$$\Omega_1(\varpi, z) = \frac{\varpi \partial_\varpi \Omega_0}{2}[K(\varpi, z) - K_0(\varpi)] \ , \tag{4.26}$$

$$I_1(\varpi) = \int_0^\varpi d\varpi' \, \Omega_0^2(\varpi') \left[\varpi' K_0(\varpi') + \frac{\varpi'^2}{2}\partial_\varpi K_0(\varpi')\right] \ . \tag{4.27}$$

It is convenient to define an auxiliary function

$$h = c^2 \int_0^P \frac{dP'}{\epsilon(P') + P'} \ . \tag{4.28}$$

This quantity is defined only inside the star. The boundary of the star is given by the surface $h = 0$. In the Newtonian limit, h reduces to the specific enthalpy. The Euler equation (4.8), to 1PN order, can be written in integral form:

$$\begin{aligned} h(\varpi, z) &= \int_0^\varpi d\varpi' \, \varpi' \Omega_0^2(\varpi') - U + C \\ &\quad + \frac{1}{c^2}\left(\frac{\varpi^4}{4}\Omega_0^4 - 2\varpi^2 \Omega_0^2 U + Qv - \frac{\varpi^2 \Omega_0^2 K_0}{2} + I_1\right) \ , \end{aligned} \tag{4.29}$$

where C is a constant and all quantities outside the integral are evaluated at (ϖ, z).

The structure of the star is determined once a rotation law is given. The rotation law we want is specified by the specific angular momentum distribution function $j(m_\varpi)$, which is determined by the

pre-collapse white dwarf (see Section 2.2.3). Straightforward calculations using Eqs. (4.7), (4.10), (4.11), (4.12), (4.13), (4.16), (4.17), (4.24) and (4.26) give

$$j = \varpi^2 \Omega_0 \left[1 + \frac{1}{c^2} \left(\frac{v^2}{2} - 3U + \Pi + \frac{P}{\rho} + \frac{\Omega_1}{\Omega_0} + \frac{Q}{v} \right) \right] . \tag{4.30}$$

To compute m_ϖ, the baryonic mass fraction inside the surface of constant j, we first need to determine the surfaces on which j is constant. In the Newtonian case, the surfaces of constant j are cylinders. This is not true in general in the relativistic case (at least not in the coordinate system we are using). Let $(\varpi + \eta(\varpi, z)/c^2, z)$ denote the surface of constant j that intersects the equatorial plane at cylindrical coordinate radius ϖ. Hence we have

$$j(\varpi + \eta(\varpi, z)/c^2, z) = j(\varpi, 0) , \tag{4.31}$$

$$\eta(\varpi, 0) = 0 . \tag{4.32}$$

Expanding the left side of Eq. (4.31) to $O(c^{-2})$, we obtain

$$\eta(\varpi, z) = -c^2 \frac{j(\varpi, z) - j_0(\varpi)}{\partial_\varpi j_0(\varpi)} , \tag{4.33}$$

where $j_0(\varpi) \equiv j(\varpi, 0)$. Using Eq. (4.30), we obtain

$$\eta = -\frac{\varpi \Omega_0 \pounds(\Pi - 3U + P/\rho) + \varpi \Omega_1 + \pounds(Q)}{2\Omega_0 + \varpi \partial_\varpi \Omega_0} , \tag{4.34}$$

where $\pounds(q) \equiv q(\varpi, z) - q(\varpi, 0)$. The baryon mass M_ϖ inside the volume V_ϖ bounded by the surface of constant j is given by

$$M_\varpi = \int_{V_\varpi} \rho u^\mu n_\mu \, dV \tag{4.35}$$

$$= 2\pi \int_{-\infty}^{\infty} dz' \left[\varpi \rho^*(\varpi, z') \frac{\eta(\varpi, z')}{c^2} + \int_0^\varpi d\varpi' \, \varpi' \rho^*(\varpi', z') \right] , \tag{4.36}$$

where n^μ is the unit vector orthogonal to the surface of constant t; dV is the proper volume element in the constant t hypersurface, and

$$\rho^* = \rho \left[1 + \frac{1}{c^2} \left(\frac{v^2}{2} - 3U \right) \right] . \tag{4.37}$$

The baryonic mass fraction is then given by

$$m_\varpi = \frac{M_\varpi}{M_0} \ , \tag{4.38}$$

where M_0 is simply the value of M_ϖ at $\varpi = R_e$, the equatorial radius of the star. It is convenient to define the normalized specific angular momentum

$$j_n = \frac{M_0}{J} j \ . \tag{4.39}$$

Straightforward calculations from Eq. (4.30) give

$$\Omega_0^2 = \frac{\lambda^2 j_n^2}{\varpi^4} - \frac{1}{c^2}\left[\Omega_0^2\left(\varpi^2\Omega_0^2 - 6U_0 + 2\Pi_0 + \frac{2P_0}{\rho_0}\right) + \frac{2\Omega_0 Q_0}{\varpi}\right] \ , \tag{4.40}$$

where $\lambda = J/M_0$ and the subscript "0" in the above equation means that the quantity is evaluated at $(\varpi, 0)$. The integrated Euler Eq. (4.29) becomes

$$h = \lambda^2\psi - U + C + \frac{1}{c^2}\left(\frac{v^4}{4} - 2Uv^2 + Qv - \frac{1}{2}v^2 K_0 + I_2\right) \ . \tag{4.41}$$

Here

$$\psi(\varpi) = \int_0^\varpi \frac{j_n^2(m_{\varpi'})}{\varpi'^3}\, d\varpi' \ , \tag{4.42}$$

$$I_2(\varpi) = \int_0^\varpi d\varpi' \left[\frac{1}{2}v_0^2\partial_\varpi K_0 + 2\varpi'\Omega_0^2\left(U_0 - \Pi_0 - \frac{P_0}{\rho_0}\right) - Q_0\Omega_0\right] \ , \tag{4.43}$$

where all the quantities in the integrands are evaluated at $\varpi = \varpi'$.

The rotational kinetic energy T and gravitation potential energy W of a relativistic star are given by (see, e.g., [9])

$$T = \frac{1}{2}\int \Omega\, dJ = \frac{1}{2c}\int \Omega T_{\mu\nu} n^\mu \varphi^\nu\, dV \ , \tag{4.44}$$

$$W = -[(M_p - M)c^2 + T] \ , \tag{4.45}$$

where the proper mass M_p and gravitational mass M are

$$M_p = \frac{1}{c^2}\int \epsilon u^\mu n_\mu\, dV \tag{4.46}$$

$$M = -\frac{2}{c^2}\int\left(T_{\alpha\beta}-\frac{1}{2}T^{\sigma}_{\sigma}g_{\alpha\beta}\right)t^{\alpha}n^{\beta}\,dV\ . \tag{4.47}$$

The expressions for T and W to 1PN order are

$$T = \int\frac{1}{2}\rho v^2\left[1+\frac{1}{c^2}\left(v^2-6U+\Pi+\frac{P}{\rho}+\frac{Q}{v}\right)\right]d^3x\ , \tag{4.48}$$

$$W = \int(\rho v^2+\rho U+3P)\,d^3x-\frac{1}{c^2}\int\rho\left(\frac{5}{2}U^2+\frac{11}{2}Uv^2-\frac{9}{8}v^4 -\frac{Qv}{2}-\Pi v^2-\Pi U-\frac{3Pv^2}{2\rho}+\frac{6PU}{\rho}\right)d^3x\ , \tag{4.49}$$

where $d^3x \equiv \varpi\,d\varpi\,dz\,d\varphi$.

Given the total baryon mass M_0, total angular momentum J, normalized specific angular momentum distribution $j_n(m_\varpi)$, and the EOS, we have to solve Eqs. (4.18), (4.20), (4.41), (4.30), and (4.38) consistently to determine the structure of the differentially rotating star. We shall discuss how these equations can be solved numerically in the next Section.

4.3 Numerical method

In this section, we develop a self-consistent field technique to calculate the structure of a relativistic star with the rotation law specified by the normalized specific angular momentum distribution $j_n(m_\varpi)$. Our method is a generalization of the one used by Smith and Centrella [22], which is a modified version of Hachisu's self-consistent field method [23].

The self-consistent field method is an iteration procedure. Suppose in a certain iteration step, we have $h(\varpi,z)$ and $\Omega_0(\varpi)$ in a cylindrical grid, we first evaluate the quantities ρ, P and Π from the EOS. Then we compute the potentials U and Q by solving the elliptic equations (4.18) and (4.20). Since the velocity potential Q always appears in the 1PN terms of the equations of motion, we can replace Ω on the right side of Eq. (4.20) by Ω_0. The angular velocity Ω, as well as $v=\varpi\Omega$, outside the equatorial plane are determined by Eqs. (4.22) and (4.24). Next, we compute the baryonic mass fraction m_ϖ using Eqs. (4.34), (4.36), (4.37) and (4.38). The function ψ is then calculated by Eq. (4.42). During each iteration, we fix two parameters, which we choose to be the central energy density ϵ_c [or equivalently, $h_c = h(0,0)$] and the equatorial radius R_e. The constants C and λ^2 in Eq. (4.41) are then given by

$$C = h_c + U_c \tag{4.50}$$

$$\lambda^2 = \frac{1}{\psi}\left[U - C - \frac{1}{c^2}\left(\frac{v^4}{4} - 2v^2U + Qv - \frac{v^2K_0}{2} + I_2\right)\right] , \tag{4.51}$$

where $U_c = U(0,0)$ and all the quantities in the second equation are evaluated at the equatorial surface of the star. Finally, we update h by Eq. (4.41) and update Ω_0 by solving Eq. (4.40). We repeat the procedure until h and Ω_0 converge to the desired accuracy.

When the star becomes flattened, the iteration scheme described above does not converge. This is fixed by the modified scheme suggested in Ref. [15]: the variables h and Ω_0 in the $(i+1)$-th iteration, h_{i+1} and $(\Omega_0)_{i+1}$ are changed to

$$h_{i+1} = h_i\delta + h'(1-\delta) , \tag{4.52}$$

$$(\Omega_0)_{i+1} = (\Omega_0)_i\delta + \Omega_0'(1-\delta) , \tag{4.53}$$

where h' and Ω_0' are the quantities determined by Eqs. (4.41) and (4.40). The parameter δ ($0 \le \delta < 1$) is used to control the changes of h and Ω_0 in an iteration step. For a very flattened configuration, we need to use $\delta > 0.9$ to ensure convergence, and it takes more than 100 iterations for the models to converge to a fractional accuracy of 10^{-5}. In the standard self-consistent field method, one only needs to solve for the density distribution ρ (or equivalently, the enthalpy distribution h) self-consistently. In our self-consistent field method, we also need to solve for the equatorial angular velocity distribution Ω_0 self-consistently. This is the main difference between the standard scheme and our proposed scheme, apart from the fact that the equations of motion in the 1PN case are more complicated.

The self-consistent field method described above computes stars with a given central energy density ϵ_c and equatorial radius R_e. However, what we want is to construct a star with a given total baryon mass M_0 and total angular momentum J. To do this, we first compute a model of nonrotating spherical star by solving the 1PN TOV equations in isotropic coordinates. We use the density distribution as an initial guess to construct a model with slightly different ϵ_c and R_e. We then build models with different values of ϵ_c and R_e until we end up with the model having the desired baryon mass and angular momentum.

For a rapidly rotating configuration, the equatorial radius extends to $R_e > 1000$ km and the polar radius is approximately $R_p \approx 10$ km in our coordinate system. Hence we use a nonuniform cylindrical grid to perform most of the computations. The resolution near the center of the star is about 0.4 km, whereas the resolution is about 6.5 km near the equatorial surface of the star. We

double the resolution to check the convergence. For a given ϵ_c and R_e, the fractional differences of the baryon mass M_0 and angular momentum J between the two resolution grids are less than 10^{-5} even for the rapidly rotating cases.

We adopt the Bethe-Johnson EOS [24] for densities above 10^{14} g cm^{-3}, and BBP EOS [25] for densities in the range $10^{11} - 10^{14}$ g cm^{-3}. The EOS for densities below 10^{11} g cm^{-3} is joined by that of the pre-collapse white dwarfs, which is the EOS of a zero-temperature ideal degenerate electron gas with electrostatic corrections derived by Salpeter [26]. We are mainly interested in the structure of the most rapidly rotating neutron stars. The central densities of these stars are around 4×10^{14} g cm^{-3} (see the next section), and ideas about the EOS in this relatively low density region have not changed very much since 1970's.

The baryon masses of the neutron stars we compute in this chapter are around $1.4M_\odot$. For a non-rotating spherical star of this baryon mass, $c^2R/GM \approx 6$ for the EOS we adopt. Here $M \approx 1.3M_\odot$ is the gravitational mass and $R \approx 12$ km is the circumferential radius of the star. Hence we expect that the second and higher order post-Newtonian terms will give about 3% corrections to our models.

4.4 Results

We only construct neutron star models corresponding to the collapse of O-Ne-Mg white dwarfs (i.e., the Sequence III white dwarfs in Section 3.2.1), because these neutron stars are the most likely to undergo a dynamical instability and emit strong gravitational waves.

Figure 4.1 shows the central densities ϵ_c/c^2 of the resulting neutron stars as a function of Ω/Ω_m, where Ω is the angular frequency of the pre-collapse white dwarf, and Ω_m is the angular frequency of the maximally rotating white dwarf in the sequence. Both Newtonian and 1PN results are shown. We see that the central energy densities for the 1PN models are higher than the Newtonian models. This is expected because relativistic effects tend to make the stars more compact. The difference in ϵ_c decreases as the star becomes more rapidly rotating.

Figure 4.2 shows the value of $\beta = T/|W|$ of the neutron stars as a function of Ω/Ω_m. We see that the relativistic correction lowers the value of β for stars of given M_0 and J. The maximum β of these neutron stars is 0.24, which is 8% lower than the Newtonian case (0.26).

The structure of the neutron stars is not much different from the Newtonian models. Stars with $\beta \gtrsim 0.1$ all contain a high-density central core of size about 20 km, surrounded by a low-density torus-like envelope. The size of the envelope ranges from 100 km (for stars with $\beta \sim 0.1$) to over 500 km (for $\beta \gtrsim 0.2$). Figure 4.3 shows the density contour of a typical rapidly rotating neutron

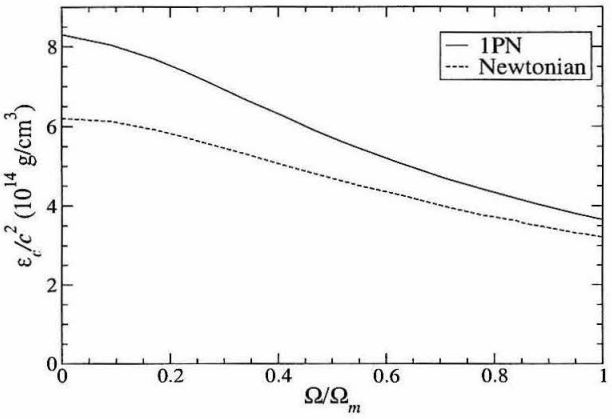

Figure 4.1: The central densities ϵ_c/c^2 of differentially rotating neutron stars as a function of Ω/Ω_m of the pre-collapse white dwarfs. Both Newtonian and 1PN results are shown for stars having the same M_0 and J.

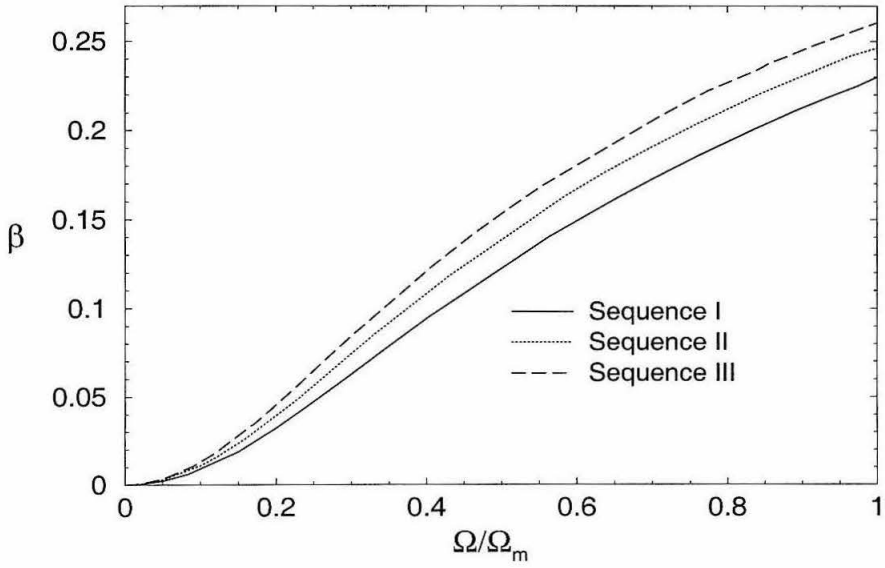

Figure 4.2: The value of β of the resulting neutron stars as a function of Ω/Ω_m of the pre-collapse white dwarfs.

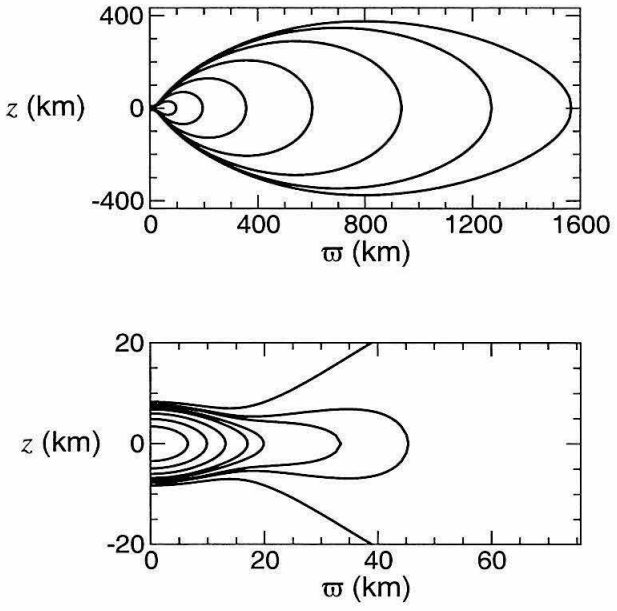

Figure 4.3: Meridional density contours of the neutron star resulting from the AIC of a rigidly rotating O-Ne-Mg white dwarf with $\Omega/\Omega_m = 0.964$. This neutron star has $\beta = 0.238$. The contours in the upper graph denote, from inward to outward, $\rho/\rho_c = 10^{-4}$, 10^{-5}, 10^{-6}, 10^{-7}, 10^{-8}, 10^{-9} and 0. The contours in the lower graph denote, from inward to outward, ρ/ρ_c= 0.8, 0.6, 0.4, 0.2, 0.1, 10^{-2}, 10^{-3} and 10^{-4}. The central density of the star is $\rho_c = 3.8 \times 10^{14}$ g cm^{-3}.

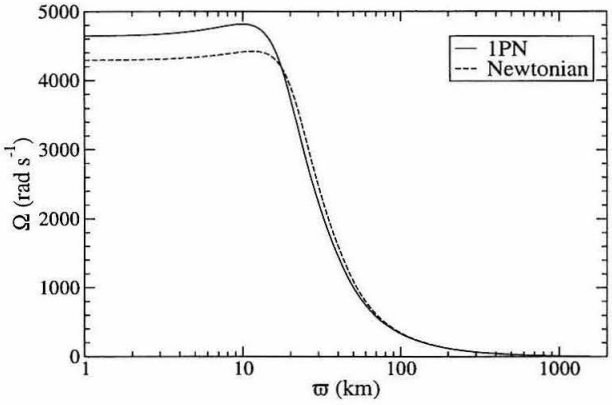

Figure 4.4: The equatorial angular velocity $\Omega_0(\varpi)$ of the neutron star in Fig. 4.3.

star. This figure looks basically the same as Fig. 3.3, which shows the density contours of the same star computed with Newtonian gravity. The β of this star is 0.238, which is somewhat smaller than the Newtonian value 0.255.

Figure 4.4 shows the equatorial angular velocity distribution $\Omega_0(\varpi)$ of the same star. We see that the angular velocity in the inner core of the star ($\varpi \lesssim 20$ km) in the 1PN model is slightly larger than that of the corresponding Newtonian model. This is expected because relativistic effects make the star more compact. The material is compressed more in the 1PN model, and should rotate faster due to the conservation of angular momentum. Figure 4.5 shows the distribution of rotational kinetic energy T and gravitational binding energy $|W|$ of the material contained within cylindrical radius ϖ. The two quantities approach their asymptotic values at $\varpi \approx 30$ km. This is due to the high central condensation of the star. Both T and $|W|$ in the 1PN model are larger than the corresponding Newtonian model. The kinetic energy T is larger because the star rotates faster. However, the difference between the two T-curves decreases as we move away from the rotation axis. This is because most of the kinetic energy of the star is from the region 10 km $\lesssim \varpi \lesssim 30$ km, in which relativistic effects are less important. On the other hand, the gravitational binding energy of the star is mainly contributed from the material in the inner region $\varpi \lesssim 20$ km, in which relativistic effects are important. As a result, the $T/|W|$ value of the relativistic model is somewhat less than in the corresponding Newtonian model.

Figure 4.6 shows the equatorial angular velocity Ω_0 for several selected models in the central region near the rotation axis. The shape of the curves are very similar to those of the Newtonian

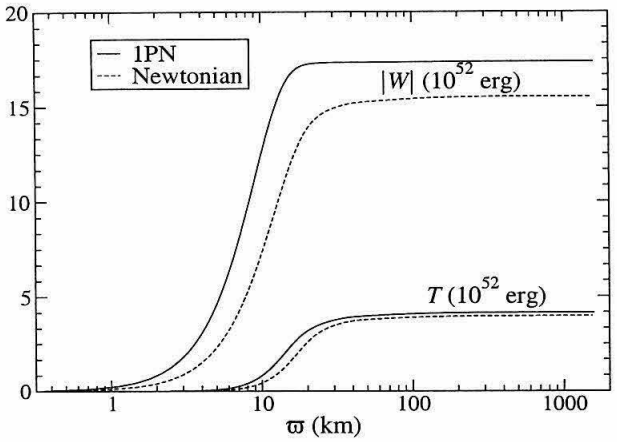

Figure 4.5: The distribution of the rotational kinetic energy T and gravitational binding energy $|W|$ of the material inside the radius ϖ, for the neutron star in Fig. 4.3.

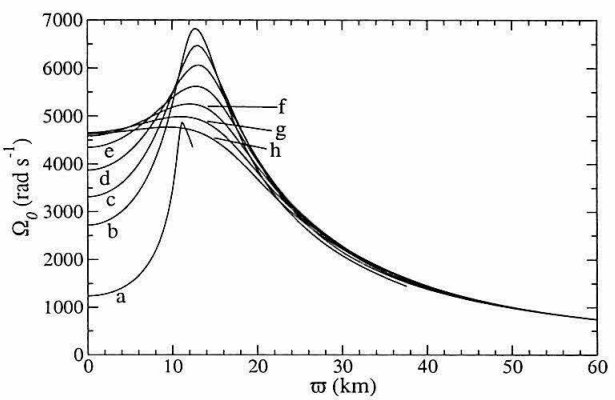

Figure 4.6: The equatorial rotational angular velocity Ω_0 as a function of ϖ for $\varpi < 60$ km. These neutron stars result from the AIC of the pre-collapse white dwarfs with Ω/Ω_m equal to (a) 0.090, (b) 0.23, (c) 0.30, (d) 0.41, (e) 0.55, (f) 0.71, (g) 0.86 and (h) 1.00.

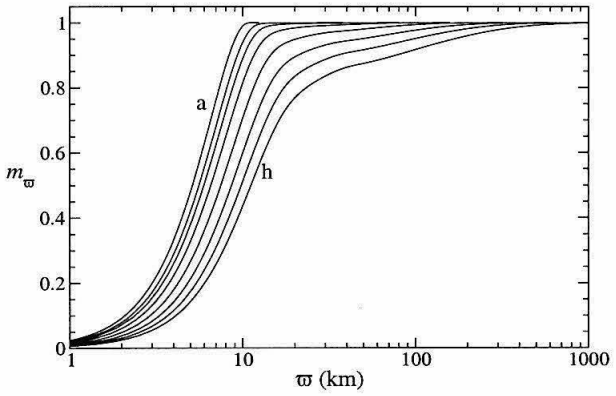

Figure 4.7: The cylindrical mass fraction m_ϖ as a function of ϖ for the neutron star models in Fig. 4.6. The curves and the corresponding models are identified by the degrees of central condensation: the higher the degree of central condensation, the lower the value of Ω/Ω_m.

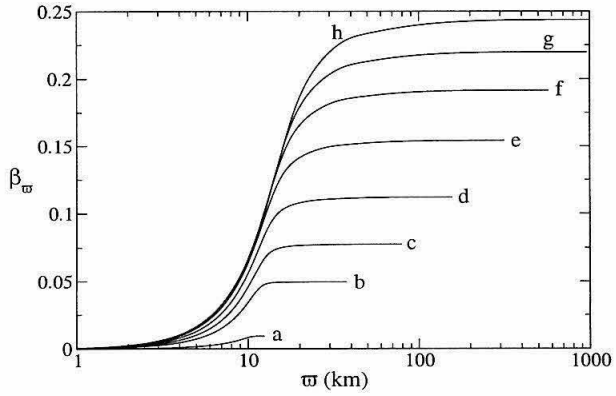

Figure 4.8: The value of β_ϖ as a function of ϖ for the neutron star models in Fig. 4.6.

models (see Fig. 3.4). However, the angular velocities in the 1PN models are all slightly larger than the Newtonian models in the inner core.

Figure 4.7 shows the baryonic mass fraction m_{ϖ} verses ϖ for the selected models in Fig. 4.6. As in the Newtonian case (see Fig. 3.5), the mass is highly concentrated in the inner core of the star. The degree of central condensation decreases as the star rotates faster. However, more than 80% of the mass is contained within a 30 km radius even for the most rapidly rotating star, where the outer envelope extends to over 1000 km. The collapsed object can be regarded as a neutron star of size about 20 km surrounded by an accretion torus.

Figure 4.8 shows β_{ϖ}, the $T/|W|$ of the material inside the surface of constant ϖ, for the selected models in Fig. 4.6. The shape of the curves are qualitatively the same as those in the Newtonian models (see Fig. 3.6), although the values of β_{ϖ} are slightly smaller. All the curves level off at $\varpi \approx 30 - 50$ km, suggesting that the material in the outer layers does not have much influence on the overall dynamical stability of the star.

4.5 Conclusions

We have generalized the self-consistent field method which can be used to compute models of differentially rotating stars to 1PN order with a specified angular momentum distribution $j(m_{\varpi})$. We also applied this new method to construct models of nascent neutron stars resulting from the collapse of massive O-Ne-Mg white dwarfs in Section 3.2.1 and compare them with the corresponding Newtonian models.

We found that the 1PN models are more compact, rotate faster, and have a smaller values of β's than the corresponding Newtonian models. The highest value of β these neutron stars can achieve is 0.24, which is 8% smaller than the Newtonian case. We estimate that the fractional error due to our neglecting higher order post-Newtonian terms is about 3%.

We have demonstrated that relativistic effects lower the value of β of a star with a given baryon mass M_0 and angular momentum J. Shibata, Baumgarte, Shapiro and Saijo demonstrated that the relativistic effects also lower the critical value β_d for the dynamical instability by a similar amount. It will be interesting to find out which of these two effects is more important. Careful numerical 1PN stability analyses must be carried out to determine whether or not relativistic effects destabilize the stars.

Bibliography

[1] M. Shibata, T. W. Baumgarte and S. L. Shapiro, Astrophys. J., **542**, 453 (2000).

[2] M. Saijo, M. Shibata, T. W. Baumgarte and S. L. Shapiro, Astrophys. J., **548**, 919 (2000).

[3] J. R. Wilson, Astrophys. J., **176**, 195 (1972).

[4] S. Bonazzola and J. Schneider, Astrophys. J., **191**, 273 (1974).

[5] I. M. Butterworth and J. R. Ipser, Astrophys. J. Lett., **200**, 103 (1976);

[6] I. M. Butterworth and J. R. Ipser, Astrophys. J., **204**, 200 (1976).

[7] I. M. Butterworth, Astrophys. J., **204**, 561 (1976); I. M. Butterworth, Astrophys. J., **231**, 219 (1979).

[8] J. F. Friedman, J. R. Ipser and L. Parker, Astrophys. J., **304**, 115 (1986).

[9] H. Komatsu, Y. Eriguchi and I. Hachisu, Mon. Not. R. Astro. Soc., **237**, 355 (1989); H. Komatsu, Y. Eriguchi and I. Hachisu, Mon. Not. R. Astro. Soc., **239**, 153 (1989).

[10] R. Mönchmeyer and E. Müller, in NATO ASI on *Timing Neutron Stars*, ed. Ögelman H., D. Reidel Publ. Comp., Dordrecht 1988.

[11] H.-Th. Janka, R. Mönchmeyer, Astro. & Astrophys., **209**, L5 (1989); H.-Th. Janka, R. Mönchmeyer, Astro. & Astrophys., **226**, 69 (1989).

[12] C. L. Fryer, D. E. Holz and S. A. Hughes, to appear in Astrophys. J., astro-ph/0106113 (2001).

[13] J. P. Ostriker and J. W-K. Mark, Astrophys. J., **151**, 1075 (1968); J. P. Ostriker and P. Bodeneimer, Astrophys. J., **151**, 1089 (1968).

[14] P. Bodeneimer and J. P. Ostriker, Astrophys. J., **180**, 159 (1973).

[15] B. K. Pickett, R. H. Durisen and R. H. Davis, Astrophys. J., **458**, 714 (1996).

[16] K. C. B. New and S. Shapiro, Astrophys. J., **548**, 439 (2001).

[17] J. M. Bardeen, Astrophys. J., **162**, 71 (1970).

[18] S. Chandrasekhar, Astrophys. J., **142**, 1488 (1965).

[19] L. Blanchet, T. Damour and G. Schaäfer, Mon. Not. Roy. Astro. Soc., **242**, 289 (1990).

[20] C. Cutler, Astrophys. J., **374**, 248 (1991).

[21] C. W. Misner, K. S. Thorne and J. A. Wheeler, *Gravitation* (Freeman and Company 1973).

[22] S. Smith, J. M. Centrella, in *Approaches to Numerical Relativity*, ed. R.d'Inverno. (Cambridge Univ. Press, New York 1992).

[23] I. Hachisu, Astrophys. J. Supp., **61**, 479 (1986).

[24] H. A. Bethe and M. B. Johnson, Nucl. Phys. A, **230**, 1 (1974).

[25] G. Baym, H. A. Bethe and C. J. Pethick, Nucl. Phys. A, **175**, 225 (1971).

[26] E. E. Salpeter, Astrophys. J., **134**, 669 (1961).